12-2021

Space Domain Awareness Assessment of Cislunar Periodic Orbits for Lagrange Point Surveillance

Adam P. Wilmer

SPACE DOMAIN AWARENESS ASSESSMENT OF CISLUNAR PERIODIC ORBITS FOR LAGRANGE POINT SURVEILLANCE

THESIS

Adam P. Wilmer, Second Lieutenant, USAF

AFIT-ENY-MS-21-D-079

DEPARTMENT OF THE AIR FORCE
AIR UNIVERSITY

AIR FORCE INSTITUTE OF TECHNOLOGY

Wright-Patterson Air Force Base, Ohio

AFIT-ENY-MS-21-D-079

SPACE DOMAIN AWARENESS ASSESSMENT OF CISLUNAR PERIODIC ORBITS FOR LAGRANGE POINT SURVEILLANCE

THESIS

Presented to the Faculty

Department of Aeronautics and Astronautics

Graduate School of Engineering and Management

Air Force Institute of Technology

Air University

Air Education and Training Command

in Partial Fulfillment of the Requirements for the

Degree of Master of Science in Aeronautical Engineering

Adam P. Wilmer, B.S.M.E.

Second Lieutenant, USAF

December 23, 2021

AFIT-ENY-MS-21-D-079

SPACE DOMAIN AWARENESS ASSESSMENT OF CISLUNAR PERIODIC ORBITS FOR LAGRANGE POINT SURVEILLANCE

Adam P. Wilmer, B.S.M.E.
Second Lieutenant, USAF

Approved:

Major Robert Bettinger, Ph.D Chair	Date
Lt Col Bryan Little, Ph.D Member	Date
Mr. David Meyer Member	Date
Dr. William Wiesel, Ph.D Member	Date

Abstract

The world is in the midst of the second Space Age. The continued development and support of NASA's Artemis program and similar international efforts has made frequent Earth-Moon travel more likely than ever in the coming decades. With this surge in traffic, it is paramount to have knowledge of the locations of all space objects in cislunar space to optimize mission readiness and prevent catastrophic collisions. Cislunar periodic orbits provide an elegant means to fill the observational capability gaps which are present in ground-based and/or near-Earth spaced-base sensors. This research involves the theoretical analysis of the effectiveness of cislunar periodic orbits for Space Domain Awareness (SDA) mission architectures. Specifically, cislunar periodic orbits are analyzed, both individually and in constellations with one another, for their effectiveness at monitoring target satellites in Lyapunov and halo orbits about the Earth-Moon L_1 and L_2 Lagrange points. In this work, over thirty cislunar periodic orbits are created and modeled in the Circular Restricted Three-Body Problem (CR3BP). Selected orbits are subject to perturbations in both the Elliptical Restricted Three-Body Problem (ER3BP) and the Bicircular Restricted Four-Body Problem (BCR4BP) to demonstrate how stabilizing controllers will be needed to maintain periodicity in these orbits. A new taxonomy for the classification of SDA regions is also presented which will enable a spatial division of the national SDA mission portfolio. Finally, selected cislunar periodic orbits are subjected to a catastrophic spacecraft explosion to understand the debris-related consequences of mishaps within this orbital regime.

Results of this research show cislunar periodic orbits to be highly effective in monitoring Lyapunov and halo orbits about the Earth-Moon L_1 and L_2 Lagrange

points, with many scenarios hosting a 100% visibility time of the targets. Further analysis into the propellant expenditure (ΔV) is required to adequately determine the feasibility of cislunar periodic orbits in a real-world, highly perturbative, environment. However, if the required ΔV is indeed low, cislunar periodic orbits are ideal candidates for SDA and surveillance of various points in cislunar space, to include the Moon and Lagrange points.

Acknowledgements

This work marks a milestone in my lifelong journey of learning. I am grateful to every one of my teachers, coaches, mentors, and relatives who helped me along the way. Conversely, it is also important to be grateful for the challenges, both academically and in life, that I faced reaching this point which inevitably strengthened my resolve. First, I would like to thank my advisor at the US Air Force Academy, Lt Col James Westfall, who mentored me throughout my senior year and assisted me in getting into AFIT. I am indebted to my AFIT faculty advisor, Maj Robert Bettinger, for his guidance, help, and support throughout the course of this research. He's the man! From responding to critical questions in the wee hours of the morning, to assisting me in participating in and traveling to conferences, to conversations about his 10,000 push-up routine every morning (I'm skeptical), Maj B has made my graduate school experience worthwhile and has led me to a greater understanding of the world around me. Next, I would like to thank Lt Col Bryan Little for his profound insight and knowledge shared on the dynamics of the universe. Finally, I would like to give a big shout-out to myself, you did it! Who would've thought?

Adam P. Wilmer

Table of Contents

Page

Page

List of Figures

List of Tables

Nomenclature

Acronyms

BCR4BP	Bi-Circular Rstricted Four-Body Problem
CR3BP	Circular Restricted Three-Boyd Problem
DOD	Department of Defense
DU	Distance Unit
ER3BP	Elliptical Restricted Three-Body Problem
FL-SDA	Fence Line Space Domain Awareness
GEO	Geostationary Earth Orbit
HG-SDA	High-Ground Space Domain Awareness
LEO	Low Earth Orbit
LG-SDA	Low-Ground Space Domain Awareness
MEO	Medium Earth Orbit
MG-SDA	Mid-Ground Space Domain Awareness
NBP	N-Body Problem
P-SDA	Parapet Space Domain Awareness
SDA	Space Domain Awareness
SME	Subject Matter Expert
SOI	Sphere of Influence
TU	Time Unit
USAF	United States Air Force

USSF	United States Space Force

Greek

ε	Error tolerance in single shooting method
θ	Angle
$\dot{\theta}$	Angular Velocity
μ	Non-dimensional mass parameter
Φ	State transition matrix
ϕ	System constraints or Phase angle
Ψ	Phase function
Ω	CR3BP psuedo-potential
$\tilde{\Omega}$	ER3BP psuedo-potential

Roman

A	Surface area of target satellite
C	Jacobi constant
e	Eccentricity or Position error
E	Earth
I	Identity matrix
$\hat{I}$	Inertial reference frame
L	Lagrangian
M	Moon
q	Generalized coordinate

$\dot{q}$	Generalized velocity
r	Position
$\dot{r}$	Velocity
$\hat{s}$	Synodic reference frame
sat	satellite
S	Sun
t	time
T	Kinetic energy
U	Potential energy
v	True anomaly
$\vec{v}$	Velocity vector
$\mathbf{X}$	State vector
x, y, z	Coordinates in the Earth-Moon rotating synodic reference frame
X, Y, Z	Coordinates in the inertial (non-rotating) reference frame

Subscript and Superscript Characters

A_1	Scalar distance from Sun to Sun-Earth-Moon baryenter
A_2	Scalar distance from Earth-Moon barycenter to Sun-Earth-Moon baryenter
C_d	Coefficient of diffuse reflection
$C^{\hat{I}\hat{s}}$	Direction cosine matrix transforming synodic reference frame to inertial reference frame
Δe_V	ΔV error induced transitioning from the CR3BP to the BCR4BP

L_1, L_2, L_3	Collinear (unstable) Lagrange Points
L_4, L_5	Triangular (marginally stable) Lagrange Points
m_e	Mass of Earth
m_m	Mass of Moon
m_S	Mass of Sun
M_v	Visual Magnitude
r_{sat}	Distance to satellite with respect to origin of reference frame
$r_{sat/e}$	Distance to satellite with respect to Earth
$r_{sat/m}$	Distance to satellite with respect to Moon
$r_{sat/S}$	Distance to satellite with respect to Sun
$r_{Tar/sat}$	Distance to Target with respect to satellite
x_S, y_S	Coordinates of the Sun in the Earth-Moon synodic reference frame
θ_e	Angle of the Earth-Moon synodic reference frame
$\dot{\theta}_e$	Angular velocity of the Earth-Moon synodic reference frame
θ_S	Angle of line connecting the Sun and synodic reference frame
$\dot{\theta}_S$	Angular velocity of the Sun about the S-E-M inertial reference frame
μ_e	Non-dimensional mass parameter of the Earth
μ_m (also μ)	Non-dimensional mass parameter of the Moon
μ_S	Non-dimensional mass parameter of the Sun

SPACE DOMAIN AWARENESS ASSESSMENT OF CISLUNAR PERIODIC ORBITS FOR LAGRANGE POINT SURVEILLANCE

I. Introduction

1.1 General Issue and Research Motivation

The opening decades of the twenty-first century witnessed a reemergence of international attention towards the realization of space missions into the cislunar[1] environment and beyond, with both nations and private companies investing into missions to the Moon and Mars. Cislunar space offers to serve as the new high-ground for national and foreign operations, allowing a positional, logistical, and visual advantage over other ground or space-based assets. The Air Force Research Laboratory (AFRL) has begun making policy with the expectation of cislunar space becoming the new high-ground. Such policy includes the creation of the Cislunar Highway Patrol Systems (CHPS) whose mission would be to search, detect, track, characterize, and catalog objects in the lunar exclusion zone (the area imperceptible due to the Sun's reflection off the Moon) [4]. This, along with national plans to develop a long-term human presence on the Moon and facilitate preparations for Human missions to Mars via NASA's Artemis program, has provided the U.S. with a vested interest in exploring trajectory design and space-based surveillance operations within the Earth-Moon system. One such class of trajectories, identified herein as cislunar periodic orbits[2], could provide support for various missions to include re-supply, personnel transport,

[1]The term "cislunar" refers to the spherical volume of space extending from geosynchronous Earth orbit to and including the Moon's orbit and the Earth-Moon Lagrange points.

[2]Cislunar periodic orbits are periodic orbits which traverse cislunar space. Periodic orbits, as a whole, are explained in Section 2.3, while cislunar periodic orbits are further explained in Section 2.3.3 with an example presented.

space-based infrastructure development, and surveillance operations. With increasing missions beyond near-Earth orbit, the use of a subset of these cislunar periodic orbits for space domain awareness (SDA)[3] mission architectures may also prove beneficial for the timely identification and tracking of resident space objects, such as satellites or space debris, to ensure safe space traffic management. Performing Space Domain Awareness (SDA) utilizing classical terrestrial and/or space-based sensors in near-Earth orbits becomes increasingly difficult when applied to the cislunar orbit regime. Cislunar periodic orbits provide an elegant means to fill this capability gap. When compared with alternative types of orbital trajectories, cislunar periodic orbits provide mission-related benefits in terms of their ability to traverse wide expanses of cislunar space capturing multiple different viewing angles of targets. Cislunar periodic orbits are also designed to repeatedly traverse a given region of cislunar space, potentially allowing for a lower propellant expenditure than typical non-periodic cislunar trajectories.

In the coming decades, it is expected that the largest U.S. Department of Defense mission with regards to SDA will be protecting the space lines of commerce. Both nations and private companies are exponentially building space-based infrastructure to ensure communication, surveillance, and transportation. In doing so, near-Earth space is becoming congested with thousands of active spacecraft and tens of thousands of debris fragments from historical mishaps and breakups. This congestion, combined with the growing connection of space access to national security and economic growth, has prompted many nations to realize the benefit of extending space operations into cislunar space. Cislunar space and the outer reaches of the Earth-Moon system are becoming the new "high ground" for space operations and the SDA mission and focus must expand accordingly to handle this growth of congestion and competition.

[3]SDA is the identification, characterization, tracking, and monitoring of resident space objects; this concept is explained further in Section 2.4.

1.1.1 Thesis Prospectus

This research involves theoretical analysis of various aspects involving cislunar periodic orbits. There is, however, much analysis which involves various other forms of periodic orbits. Simulations are conducted to assess the effectiveness of these orbits in SDA missions, namely in monitoring Lyapunov and halo orbits located at the L_1 and L_2 Lagrange points. Dynamical variations in cislunar periodic orbit trajectory are analyzed to determine how added perturbations affect trajectory, and ultimately how stabilizing controllers will be needed to maintain periodicity in these orbits. A novel SDA taxonomy is also proposed which will assist in enabling a spatial division of the national SDA mission portfolio. A catastrophic explosion is simulated onboard a spacecraft along cislunar periodic orbits to analyze the debris related risks to other satellites in the same orbit as well as risks to the Earth and Moon

Specifically, the research will analyze various satellite constellation designs utilizing cislunar periodic orbits to provide a baseline assessment of SDA functionality in cislunar space. The research will use the Circular Restricted Three-Body Problem (CR3BP) and Bicircular Restricted Four-Body Problem (BC4BP) as the primary dynamical models for cislunar trajectory generation, study, and analysis. In addition, the Elliptical Restricted Three-Body Problem (ER3BP) will be implemented to demonstrate how the inclusion of the Moon's eccentricity may change the orbital trajectory.

Research into this topic will advance ongoing research into SDA architectures within the cislunar domain. The analytical focus on exploring the use of cislunar periodic orbits for the SDA mission set is novel because these orbits have traditionally been studied with respect to the cislunar logistical transport of personnel and materiel. Research into cislunar periodic orbits is sought as a potential trajectory that can be leveraged to expand the SDA footprint into the cislunar domain, and provide an

alternative means for the search, track, and characterization of both natural and man-made objects in that environment.

1.2 Methodology

With the application of assumptions restricting the orbital shape and relative inclination of celestial bodies such as the Earth and Moon, numerical analysis of the motion of small bodies of comparatively negligible mass (e.g., a satellite) within a multi-body gravitational system is possible. The motion of objects in cislunar space is determined using various astrodynamical models such as the CR3BP, ER3BP, and BCR4BP. While cislunar periodic orbits for resident space objects are most easily found and accessed by means of the CR3BP, through stabilizing controllers (such a propellant expenditure) periodic orbits may remain stable even when transitioning into higher fidelity models. After the initial conditions (initial position and velocity) of cislunar periodic orbits are found in the CR3BP, select orbits are subject to various dynamical models, analyzed for their effectiveness in SDA mission scenarios, and used for debris propagation analysis.

1.2.1 Earth-Moon System and Lagrange Points

Understanding of the Earth-Moon system is of vital importance in astrodynamical trajectory design within cislunar space. From the gravitational tug-of-war between the Earth and Moon, points of stability emerge. These points of stability are referred to as Lagrange points (also called libration points). The Earth-Moon Lagrange points are shown with respect to the Earth and Moon in Fig. 1:

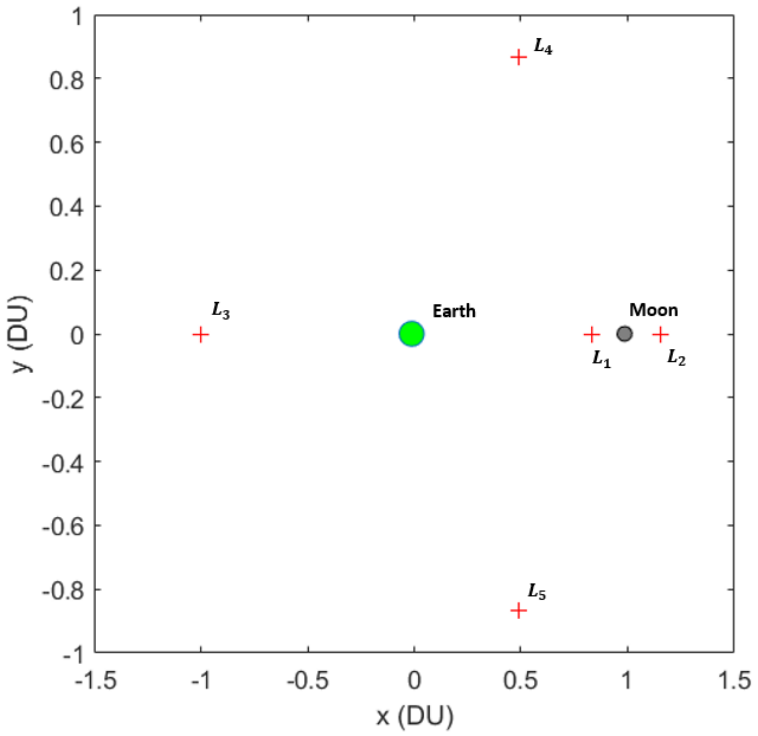

Figure 1: Earth-Moon System

As shown in Figure 1, there are five Lagrange points in the Earth-Moon system (L_1, L_2, L_3, L_4, L_5); these are stationary points which are always in the same position with respect to the Earth and Moon. Therefore, these points rotate about the Earth-Moon barycenter at the same rate that the Earth and Moon do, in an inertial (non-rotating) reference frame. If an object were precisely at one of these Lagrange points, they would remain there indefinitely. Lagrange points are discussed in detail in Section 3.3.2.

The L_1 and L_2 Lagrange points are anticipated to be some of the most utilized and important points in cislunar space. Specifically, many have proposed these points as inexpensive gateways for performing transfers between orbits. The L_1 manifold can enable transfers to the lunar region for less fuel than a conventional Hohmann transfer, and the L_1 point might be an appealing location for future spacecraft due

to its high vantage point over the Earth and Moon. In terms of application, NASA's Artemis program has a planned lunar gateway to be orbiting the L_2 Lagrange point in a near-rectilinear halo orbit. The Chang'e-4 mission was also accompanied by the Queqiao communications relay satellite orbiting the L_2 Lagrange point [5]. Due to the potential for use and anticipated increase in such use, L_1 and L_2 surveillance is the primary SDA focus of the cislunar periodic orbits analyzed in this research.

1.2.2 The Circular Restricted Three-Body Problem

The CR3BP is the most foundational cislunar trajectory model used to model the motion of a spacecraft under the gravitational forces of the Earth and Moon. Key assumptions to this model include that the spacecraft is of negligible mass when compared to the Earth and Moon, and that the Moon is in a circular orbit about the Earth. The CR3BP has no known closed form analytical solution and, as a result, numerical integration must be implemented to solve for an approximate solution. Luckily, today's computers have the capability and computing power to quickly solve for approximate solutions with high accuracy and precision. The CR3BP equations of motion consists of two (if working in the 2-D case) or three (if working in the 3-D case) second order differential equations which require an initial position and velocity to numerically integrate. Due to the chaotic nature of the CR3BP, trajectories are highly sensitive to changes in initial conditions, thus, small changes in initial conditions result in large changes to overall trajectory. The CR3BP provides insight to Lagrange points: points of stability in which an orbiting object, if precisely at a Lagrange point, will remain fixed in an Earth-Moon rotating reference frame, or appear to move in a circular orbit about the barycenter in an inertial (non-rotating) reference frame. The CR3BP equations of motion derivation, Lagrange Points, and stability are discussed in detail in Chapter 3.3.

1.2.3 Elliptical Restricted Three-Body Problem

In reality, the Moon's orbit about the Earth is not circular, but rather slightly elliptical. The ER3BP is an extension of the CR3BP in which the Earth and Moon are not assumed to be in a perfectly circular orbit about their shared barycenter. The elliptical motion of the Moon creates the perception that the Earth and Moon are oscillating along their shared axis in the synodic reference frame. The ER3BP equations of motion derivation, Lagrange Points, and stability are discussed in detail in Chapter 3.4.

1.2.4 Bicircular Restricted Four-Body Problem

The BCR4BP is an extension of the CR3BP in which the gravitational influence of the Sun is included. While Solar gravity is small compared to other perturbations in near Earth orbit, as a spacecraft nears the edge of the Earth's sphere of influence (SOI) the Sun begins to have a greater impact on trajectory. Past the Earth's SOI, solar gravity begins to supersede Earth's gravity. In the BCR4BP, the Earth and Moon revolve in a coplanar circular orbit about their shared barycenter. This Earth-Moon barycenter, along with the Sun, then revolve in a coplanar circular orbit about the Sun-Earth-Moon barycenter. This is best explained visually in Fig. 8. The BCR4BP equations of motion derivation, Lagrange Points, and stability are discussed in detail in Chapter 3.5.

1.2.5 Space Domain Awareness

As space begins to be increasingly viewed as a warfighting domain, SDA acts to assist in such operation. Sometimes used interchangeably with space situational awareness (SSA), SDA is, at it's core, a mission of space surveillance and intelligence. Specifically, SDA is the identification, characterization, tracking, and monitoring of

any factor associated with the space domain that could affect space operation, thereby impacting the security, safety, economy, or environment of the U.S. [6]. Within this analysis, SDA effectiveness is a function of how often the Target object is observable. The SDA simulation model used in this analysis takes into account exclusion angles from the Sun, Earth, and Moon to determine Target visibility. SDA is explained further in Section 2.4. The methodology behind the simulation analysis is described in detail in Chapter 3.9 with results presented in Chapter IV. A new SDA taxonomy is then proposed in Chapter V.

1.3 Thesis Overview

This research is organized as follows:

- Chapter II: Trajectory models, to include perturbation theory and n-body problems are described. Detailed reviews of existing literature related to the areas of this research including history of trajectory generation and the astrodynamical models used, periodic orbits, and space domain awareness.

- Chapter III: In this chapter the trajectory model equations of motion are derived and the features of each model are analyzed and discussed. Next, the method of generating or "discovering" periodic orbits is discussed with an example case presented. All periodic orbits discovered are either presented or their respective location within this thesis is mentioned. Differential correction in the form of the single and multiple shooting methods are then discussed. Afterwards, the simulation model, which was used to determine space domain awareness effectiveness, is discussed with its assumptions stated. Finally, a statistical debris model to determine spacecraft survivability is discussed.

- Chapter IV: The results of the space domain awareness simulations conducted

in Systems Tool Kit (STK) are presented. Simulations consist of 12 cislunar periodic orbits analyzed, both individually and in constellations with one another, for their effectiveness of monitoring four scenarios: 2 targets in a L_1 Lyapunov orbit, L_2 Lyapunov orbit, L_1 halo orbit, and L_2 halo orbit. Dynamical variations in trajectory when transitioning from the CR3BP to the ER3BP and BCR4BP are also presented. Finally, through means of differential correction, it is shown how much error, in terms of ΔV, the BCR4BP dynamics introduce on the CR3BP solutions for a given number of patchpoints.

- Chapter V: A proposed SDA taxonomy for describing regions in space is presented which will enable a spatial division of the national SDA mission portfolio. This taxonomy utilizes specific regions corresponding to compounding distances from the Earth and varying SDA mission subsets, to include space traffic management, space control, lunar/Lagrange point surveillance, space weather observation, and planetary defense. The history of SDA and its origins from space situational awareness (SSA) are also discussed.

- Chapter VI: Potential debris-related consequences of a catastrophic explosion on-board spacecraft traveling along select cislunar periodic orbits are analyzed. Specifically, this case study features cislunar periodic orbits with host notional spacecraft that are subjected to catastrophic breakup events at various location along their trajectories, which are simulated using the dynamics of the BCR4BP. The orbital states of debris fragments at the end of the simulation window are used to evaluate the potential risk to orbital regimes near Earth and the Moon due to a cislunar periodic orbit debris event.

- Chapter VII: Summarizes, provides conclusions to the overall research, and describes avenues for further research to be conducted.

II. Background and Literature Review

2.1 Chapter Overview

The purpose of this chapter is to highlight relevant research and models related to the problem of determining the motion of a satellite in cislunar space, various types of periodic orbits in cislunar space, space domain awareness, and debris risk to spacecraft. Section 2.2 discusses models for determining spacecraft motion and trajectory, including perturbation theory, the three-body problem, the four-body problem, and higher fidelity computational models. Section 2.3 reviews periodic orbits and literature that has been published on the subject. Periodic orbits which are described include cislunar periodic orbits, Lyapunov orbits, and halo orbits. A detailed discussion on the concept and history of space domain awareness is presented in section 2.4. Finally, a concise discussion on the debris environment in space and previous work conducted is presented in section 2.5

2.2 Spacecraft Trajectory Model: Perturbations and The Problem of N-bodies

The study of celestial mechanics is one heavily rooted in dynamical analysis and had a significant contribution to the development of classical mechanics [7]. Specifically, the problem of multi-body celestial motion and dynamics has long been studied, with analysis historically seeking to predict planetary position and motion as a function of time. Interest in multi-body dynamics gained an increase in momentum during the nineteenth century and culminated with the King of Sweden, Oscar II, putting forth a challenge: starting from an arbitrary initial configuration, solve the general three-body problem in the form of a series expansion describing the positions of the three bodies for all future moments of time [8]. Although Poincaré and his contempo-

raries developed an analytical method to approximate this motion, the realization of closed-form solutions remains unattainable due to the chaotic nature of multi-body dynamics.

The N-body problem (NBP) represents a generalized model of the motion of celestial bodies as mass particles. A main assumption to this problem is that the distribution of mass among each gravitational body in the system is spherically symmetric, or that the size of the bodies are small when compared to the distances which separate them [7]. The Solar System is, at its core, an NBP. There are various methods which are used to obtain the equations of motion for different forms of NBPs: Lagrange's equations of motion, Hamilton's canonical equations, the Hamilton-Jacobi equations, Hamilton's principle, Kane's method, D'Alembert's principle, and the Appellian method. The basic methodology for all of these methods remains consistent: project Newton's Second Law along the cardinal vectors.

All dynamical trajectory models require some form of assumption to reach an approximate solution. The complex and chaotic dynamics of trajectories within a multi-body domain, such as cislunar space, causes for varying solutions depending on the dynamical model used and location of the spacecraft with respect to the Earth and Moon. Many perturbations exist in this environment which influence the motion of the spacecraft: gravitational influences of the Earth, Moon, Sun and other gravitation bodies, Earth's oblateness, local deviations caused by mountain ranges and oceans, solar radiation pressure, atmospheric drag if the trajectory contains close proximity passes of a gravitational body's atmosphere. While it would be ideal to include all perturbations in any trajectory model, this becomes difficult both in developing the equations of motion as well as computing a solution once the equations are developed. Many variables also aren't deterministic, such as atmospheric drag, causing the need for assumptions to arise somewhere in the process of determining the trajectory.

Therefore, it is best to determine which perturbations are vital to the model, which ones may be ignored, and how high of fidelity a model needs to be to produce solutions that are adequate for the work that's being conducted.

2.2.1 Perturbation Theory

Perturbation theory is one of the most basic methods commonly used to model the motion of a spacecraft subject to multiple perturbing forces. In general perturbation theory, the largest terms in the equations of motion are those which arise from the Two-Body (Earth and spacecraft) problem. Therefore, the equations of motion are formed with the assumption of an orbit which is Two-Body-like, thus resembling the two-body problem equations of motion with other perturbations seen as additional terms added on. Perturbation theory was heavily used in the early days of orbit prediction before computers were available to ease the computational load. The benefit of this model is that it is able to generate accurate predictions without requiring very long computational burdens seen by other methods which require numerical integration. Numerical integration is avoided in general perturbation theory allowing for an approximate analytical solution to the trajectory to be obtained in the form of an infinite series expansion [9].

The fundamental assumption of perturbation theory is that all secondary (non-Two-Body) perturbations remain small in comparison to the Earth's gravity. Perturbation theory is extremely useful for high-altitude Earth orbits where the spacecraft is high enough that atmospheric drag is small but low enough to where the Sun and Moon's gravitational force also remain small. Past GEO perturbation theory begins to break down as the Moon's gravitational force no longer remains small, thus it is advised to use other models for trajectories contained within cislunar space and beyond.

2.2.2 The Three-Body Problem

The three-body problem is a classical astrodynamics problem which aims at predicting the motion of three celestial bodies under the gravitational force of one another. In terms of satellite trajectory, the three-body problem becomes the restricted three-body problem, simply meaning that the mass of the third body (i.e., the satellite) is negligible when compared to the Earth and Moon. The restricted three-body problem models the motion of a satellite under the gravitational influence of the Earth and Moon. There are two main types of restricted three-body problems: the circular restricted three-body problem (CR3BP) and the elliptical restricted three-body problem (ER3BP). The first assumes the Moon to have a circular orbit about the Earth while the latter takes into account the Moon's eccentricity. As discussed in sections 1.2.2 and 1.2.3, the problem of three bodies is a useful tool in early trajectory analysis and provides useful insights into the dynamical properties of the Earth-Moon system. These properties and characteristics are explored in detail in Sections 3.3 and 3.4.

In the late 19th century, Poincaré [10] made considerable contributions in the qualitative theory of the restricted three-body problem and dynamical systems alike. His work was the first to hint at the chaotic behavior of a dynamical system and inevitably proved that the CR3BP solution is infinitely discontinuous. Later in 1967, Szebehely [11] synthesized his knowledge of dynamics and the three body problem to culminate one of the first books on the subject: *Theory of Orbits*. This work provided a standard knowledge base and created a fundamental structure for how academicians may study the restricted problem of three bodies. A recent 2013 study by Parker and Anderson [12] surveyed thousands of trajectories used to transfer a spacecraft between the Earth and various locations near the Moon. This detailed work provides critical insight into three-body dynamics while also providing high-level information to mission managers and designers regarding low-energy Earth-Moon transfers.

While near-Earth space remains a focus for many missions, renewed attention is being given to pursuing missions in cislunar space and beyond the Earth-Moon system. Recent missions have incorporated three-body dynamic techniques to successfully operate in the cislunar domain. In terms of these cislunar space operations, there are reinvigorated U.S. civil initiatives to return to the Moon with NASA's Artemis program and other planned commercial space projects. Additionally, an increase in international projects has pushed space domain awareness (SDA) and space mission considerations beyond near-Earth space. Examples of recent international missions include China's Chang'e-5 successful lunar landing in December 2020 [13], India's Chandrayaan-2 (failed) lunar landing in September 2019 [14], Israel's Beresheet (failed) lunar landing in February 2019 [14, 15], and the injection of China's Queqiao relay satellite into orbit around the unstable L_2 Earth-Moon Lagrange point in January 2019 [5].

The three-body problem begins to break down in accuracy during close proximity passes of gravitational bodies where atmospheric drag or non-spherical gravity models become a significant perturbation. Solar gravitational forces can also significantly influence and alter the trajectory, even in cislunar space and especially over long time periods. However, even with these inconsistencies, the CR3BP provides incredible insight on properties of the Earth-Moon system such as Lagrange points, while also providing a useful starting point for periodic orbit generation and analysis.

2.2.3 The Four-Body Problem

The four-body problem is an extension of the three-body problem in which the solar gravity is included as a perturbation. The four-body problem aim at describing the motion of four celestial bodies under the gravitational attraction of one another. As with the three-body problem, for satellite trajectory computation, the fourth

body's (i.e., the satellite's) mass is negligible when compared to the other bodies, thus the restricted four-body problem is formed.

Koon et al. [1] describes two methods of modeling the restricted four-body problem: the concentric circular model and the bicircular model which are shown below in Figs. 2(a) and 2(b) respectively:

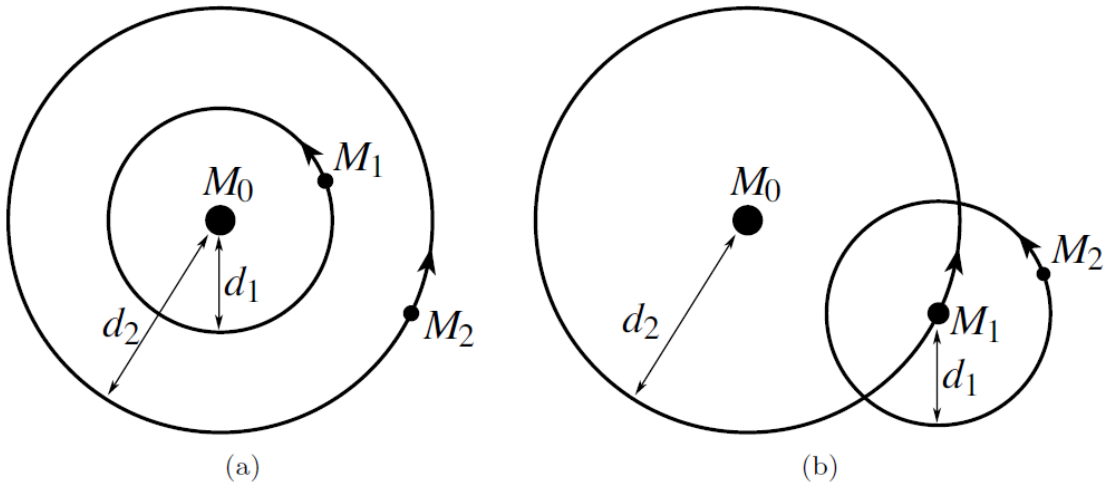

Figure 2: Models of Motion for the Restricted Four-Body Problem [1]

In the concentric circular restricted four body problem model (shown in Fig. 2(a)) M_0 is the central body about which M_1 and M_2 rotate in circular orbits. It is generally presumed that the masses of M_1 and M_2 are significantly less than M_0. An example of this type of system is the Jupiter-Ganymede-Callisto system (modeled as M_0, M_1, and M_2 respectively) [1].

In the bicircular restricted four-body problem (BCR4BP) model (shown in Fig. 2(b)) M_1 and M_2 are in a circular orbit about their shared barycenter which is in a circular orbit about M_0. It is generally presumed that the mass of $M_2 \ll M_1 \ll M_0$. The first use of the BCR4BP appears to be by Huang [16] in 1960. This is a common model for the Sun-Earth-Moon system (modeled as M_0, M_1, and M_2 respectively). However, the BCR4BP does not take into account some critical information about the

system which may lead to inaccurate solutions. Such information which is omitted includes the inclination differences between the Moon's orbit about the Earth and the Earth's orbit about the Sun (assumed to be zero), the eccentricity of the Moon about the Earth (assumed to be zero), and the eccentricity of the Earth about the Sun (assumed to be zero). While it can be argued that all of these are small changes, the author contends that many small changes and assumptions lead to large changes in overall solution. Therefore, this was not the primary model used in analysis. However, it does provide some insights into trajectory such as approximate ΔV required to maintain an orbit.

2.2.4 Higher Fidelity Models

High-fidelity orbit propagators operate with minimal assumptions, attempting to take into account as many real-life perturbations as possible. Due to this, they are often used to validate the results from analytical models. AGI's systems tool kit (STK) high-fidelity orbital propagators include astrogator and HPOP. Astrogator provides for trajectory and maneuver planning while also including targeting capabilities. HPOP, which stands for high-precision orbit propagator, is able to handle circular, elliptical, parabolic, and hyperbolic orbits at distances as close as the surface of the Earth to beyond the orbit of the Moon [17].

While these higher fidelity models lead to more precise solutions, they require an increase in required computation time, which becomes especially apparent when simulating many scenarios over long time periods. Pertaining to this research, this accuracy would only be useful for precise ΔV measurements and precise debris propagation following a mishap along a periodic orbit, neither of which were a primary focus of this research. Therefore, these models were not used in the present research.

2.3 Periodic Orbits

2.3.1 Definition

Periodic orbits are defined as orbits with trajectories which periodically return to their initial conditions (position and velocity). Due to this, periodic orbits feature repeating patterns which tend to appear artistic in the synodic reference frame.

2.3.2 Background

In 1897, Darwin [18] built on the work of Poincaré and Hill [19], and was seemingly the first to present numerical integration results for a specific mass parameter and a symmetric form of the potential function. It was later pointed out by Poincaré and Hough, that the kind of continuity used was not possible, leading Hough to write a paper addressing these deficiencies [20] and Darwin to release a publication [21] confirming Hough's conclusion. Decades later, while director of the Copenhagen Observatory, Strömgrén led his team to numerically determine and categorize families of periodic orbits; the tabulated results were published in 1934 [22]. In 1958, Egorov [23], unsatisfied with the solutions which literature of the time provided, noted many questions were either left unanswered or not fully answered with respect to Moon flight theory. These questions pertained to possible trajectories for circumnavigating the Moon and returning to Earth, the possibility of periodic circumnavigation of the Moon and Earth (i.e., periodic orbits), the shape and classification of trajectories in the passive phase, the problem of minimum initial velocities required for reaching the moon, and the effect produced by a spread in the initial conditions on the characteristics of various lunar flight trajectories. An evolution in computing technology around this time was pivotal in accelerating progress in the field of trajectory design with numerical integration significantly more feasible, thus leading to more discoveries of periodic solutions [11]. Robert Newton [24] appeared to be the first to specifically

study periodic orbits which involve close passages of both the Earth and Moon from which he generated using a particular methodology: starting with a point lying on the x-axis, vary only the velocity in the y-direction, creating a dependence that the initial y-velocity is a function of the initial x-position.

In the early 1960's, Arenstorf [25, 26] presented methods for solving families of synodically-closed periodic solutions in the CR3BP which, he noted, can be altered to have close proximity passes to both gravitational primaries. These periodic orbits are presented in terms of resonance, order, and period. Of practical use, Arenstorf discovered an Earth-Moon "figure-8" orbit in 1963 which was later used in the Apollo program [27].

Overall, the majority of research since the mid-twentieth century pertaining to periodic orbits within a multi-body gravitational system has focused on the determination of trajectory solutions for symmetric periodic orbits. A segment of researchers embarked on describing and determining families of asymmetric solutions, with such analysis requiring two initial values to be simultaneously adjusted in order to obtain a periodic solution as opposed to one with symmetric orbits [28].

2.3.3 Cislunar Periodic Orbits

Cislunar periodic orbits are a subset of periodic orbits in which the trajectory path will traverse cislunar space, or the spherical volume of space which extends from Earth's geosynchronous orbit to and including lunar orbit and the Earth-Moon Lagrange points. A stipulation to these orbits traversing cislunar space is that they *do not* soley orbit a Lagrange point (those are Lyapunov, Halo, and Lissajous orbits). An example of a cislunar periodic orbit generated by Arenstrof [25, 26] is shown in Fig. 3:

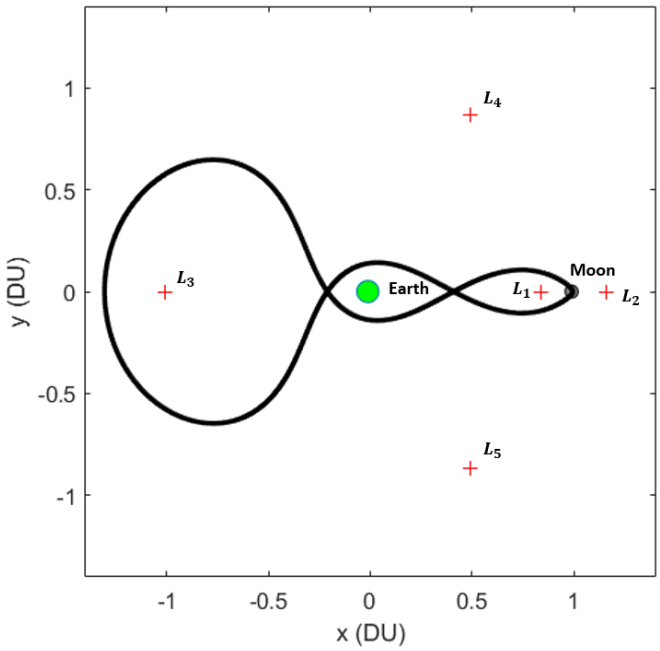

Figure 3: Example Cislunar Periodic Orbit

2.3.4 Lyapunov Orbits

Lyapunov orbits are periodic orbits about any of the three collinear (L_1, L_2, and L_3) Lagrange points whose trajectories lie completely in the plane of the Earth and Moon (i.e., there is no z-component to their position or velocity). These orbits were named after the Russian mathematician Aleksandr Lyapunov for his work on stability theory, ordered differential equations, and non-linear analysis [2]. An example of a family of Lyapunov orbits about the L_1 Lagrange point is shown below:

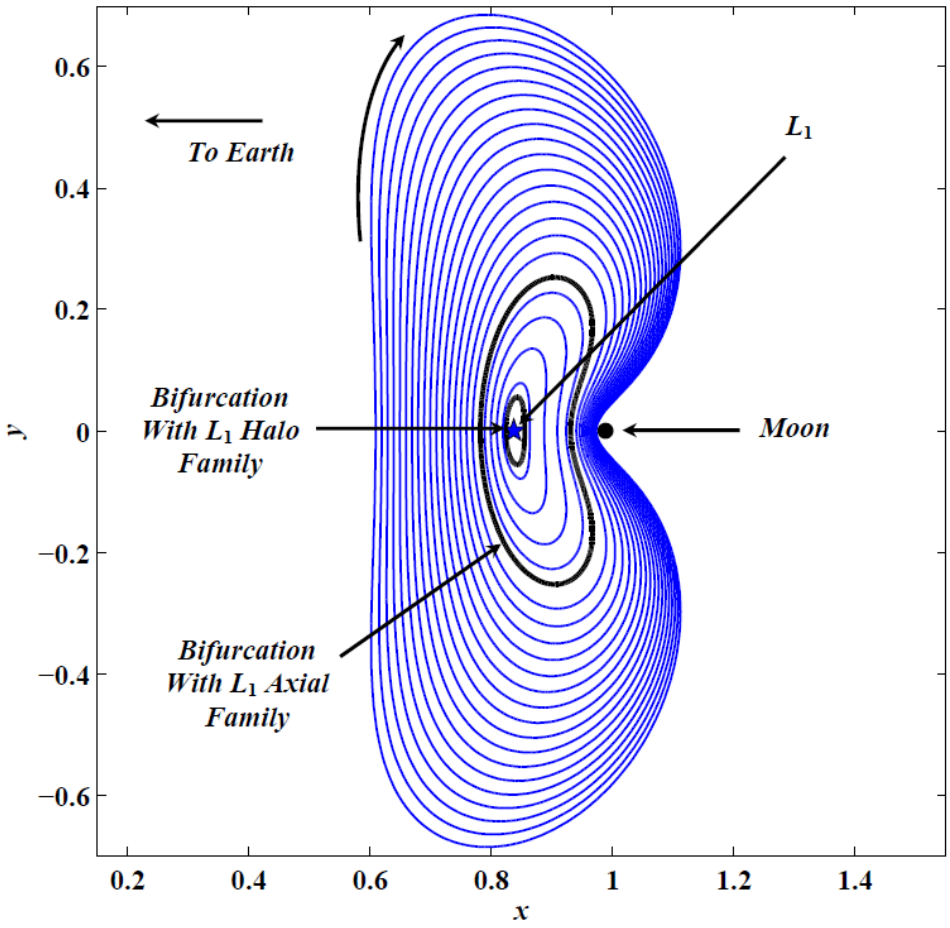

Figure 4: Family of Lyapunov Orbits about the L_1 Lagrange Point [2]

Due to the dynamics about the Lagrange points, these orbits generally develop more of a kidney-bean-like geometry as the radius from the Lagrange point increases.

2.3.5 Halo Orbits

Similar to a Lyapunov orbit, halo orbits are also periodic orbits about any of the three collinear (L_1, L_2, and L_3) Lagrange points. However, the difference lies in that these are three-dimensional orbits whose trajectory crosses the z-axis. Robert Farquhar first used the term "halo orbit" in his 1968 dissertation [29] in which he researched satellite station-keeping in the vicinity of the L_1 and L_2. The term "halo"

originates from these orbits appearing as a halo around the Moon when viewed from the Earth. The halo orbits used in this work were obtained through a methodology presented in Section 3.8

2.4 Space Domain Awareness

As defined by the 2020 *Spacepower: Doctrine for Space Forces*, Space Domain Awareness (SDA) "encompasses the effective identification, characterization, and understanding of any factor associated with the space domain that could affect space operations and thereby impact the security, safety, economy, or environment of our Nation" [6]. With the space domain becoming increasingly congested, contested, and competitive as peer, near-peer, and emerging space powers expand their presence in space, SDA will remain a critical mission for securing and advancing the space operations of the U.S. and its allied and partner nations in the coming decades [30].

2.4.1 Evolution from Space Situational Awareness

For nearly 50 years following the start of the first Space Age in the mid-twentieth century, space represented a supporting function to wider terrestrial conflict – either on land, at sea, or in the air. Space became the "ultimate high ground," as first described by then-USAF chief of staff General Charles Gabriel in 1982, which enabled the introduction of game-changing technologies in the form of persistent overhead surveillance, communication beyond the line-of-sight, and precision navigation and timing that would spur a revolution in U.S. military strategy and operational art in the latter twentieth and early twenty-first centuries [31]. Against this backdrop of space access and utilization, a new mission emerged in the 1960s: early warning and space object tracking and characterization. The proto-form of what would become known as "space situational awareness" (SSA) arose due to the need to differentiate between

non-hostile resident space objects (e.g., friendly satellites and debris) and ballistic missile nuclear payloads [32]. The SSA mission grew to encompass four functions: search, detect, track, and characterization. Once a space object is characterized and its position and velocity is known for predictive tracking, then the object is catalogued. At its heart, the SSA mission became one of space traffic management, with ground- and space-based sensors constantly updating and refining the space object catalog in order to de-conflict orbits and generate collision avoidance warnings [33].

Just as the U.S. Air Force (USAF) was created out of the need for service dedicated to attaining and projecting air power in the wake of World War II based on the growing role of the air domain in military and national security operations, the U.S. Space Force (USSF) has emerged as an independent service due to the need to attain and maintain national power and superiority in space – a domain which is now irrevocably linked to U.S. sovereignty and economic power. Until the start of the 2010s, there was general hesitancy to refer to space as a "warfighting domain"; however, the patent realization of space as a domain that is congested, contested, and competitive has prompted an evolution in how space is viewed and framed from a national security perspective [34]. While SSA remains a consistent term used in civilian space flight, the general SSA mission has become a subset of a wider mission set for the Department of Defense – SDA. In a memorandum released to the then-Air Force Space Command in 2019, Major General John Shaw discussed the formal shift from SSA to SDA within the Department of the Air Force, and stated that "the implication of space as a warfighting domain demands we shift our focus beyond the Space Situational Awareness mindset of a benign environment to achieve a more effective and comprehensive SDA" [34]. The document *Spacepower: Doctrine for Space Forces* outlines that SDA "leverages the unique subset of intelligence, surveillance, reconnaissance, environmental monitoring, and data sharing arrangements that pro-

vide operators and decision makers with a timely depiction of all factors and actors - including friendly, adversary, and third party - impacting domain operations" [6].

2.4.2 The New High-Ground: Cislunar Space

Until the 2010s, SDA missions were nominally restricted to the "near-Earth" orbital regime bounded by geosynchronous and super-synchronous orbit due to the volume of space traffic within this region. However, the late 2010s and early 2020s have marked a shift in the space operations paradigm, with a renewal in international interest of pursuing missions extending into the cislunar environment, to the Moon, and beyond the gravitational influence of the Earth-Moon system. Domestically, this shift is represented by reinvigorated initiatives to return to the Moon via NASA's Artemis program and planned commercial space projects. Recent international activity includes plans to develop a joint Chinese-Russian base at the lunar south pole in the 2036-2045 time frame [35], China's Chang'e-5 lunar sample-return mission in 2020 [36], Israel's attempted lunar surface mission in 2019 [15], and China's Chang'e-4 far-side lunar mission in 2018. Of note, the Chang'e-4 mission was accompanied by the Queqiao communications relay satellite orbiting the L_2 Earth-Moon Lagrange point [5]. International missions in cislunar space will likely increase throughout the 2020s, with a likewise increase in the number of spacecraft operating in this region as scientific exploration expands, space system technology evolves, and the lunar economy emerges and develops.

Attaining space situational and wider space domain awareness in the highly dynamic space domain of the future will require a field of view not limited to the traditional bounds of geosynchronous orbit, with the SDA mission embracing the entirety of the Earth-Moon system. Undoubtedly, *the largest U.S. Department of Defense mission with regards to SDA will be protecting the space lines of commerce*

[37, 38]. Nations and private companies alike are exponentially building space-based infrastructure to ensure communication, surveillance, and transportation. In doing so, near-Earth space is becoming congested with thousands of active spacecraft and tens of thousands of debris fragments from historical mishaps and breakups. This congestion, combined with the growing connection of space access to the national security and economic growth, has prompted many nations to realize the benefit and prestige of extending space operations into cislunar space. Cislunar space and the outer reaches of the Earth-Moon system are becoming the new "high ground" for space operations and the SDA mission and focus must expand accordingly to handle this growth of congestion and competition. Chapter V outlines a proposed taxonomy to better describe SDA missions performed in this expanding environment.

2.4.3 Challenges and Limitations to SDA in Cislunar Space

As peer and near-peer competitor nations edge towards pursuing space superiority, the sensors and ground stations which formed the cornerstone of U.S. SDA in previous decades are becoming restrictive in their range and resolution. Previous views of space operations being nominally limited to geosynchronous orbit and below are being superseded by a growing necessity to attain situational awareness of resident space objects deep within the cislunar environment. The limitations with which U.S. space sensing assets face will undoubtedly need to be relieved to ensure U.S. global superiority. The International Academy of Astronautics assesses that "the capacity and accuracy of current space monitoring systems is not sufficient to cover small objects or to provide for orbital avoidance service for all space assets" [39]. Ground-based radar and optical systems are the primary method for characterizing objects in space; however, weather, solar blind spots, and their terrestrial moorings all cause limitations [33]. Furthermore, many ground-based systems have significant optical

capability gaps, such as the Ground-Based Electro-Optical Deep Space Surveillance (GEODSS) system which is only capable of tracking basketball-sized objects at a distance of 32,187 km (20,000 miles) [33].

In terms of tracking and orbit determination via optical sensors, one primary challenge is solar exclusion angle: the cone region with respect to the Sun within which an optical sensor cannot view a given object. In other words, the Sun is too close to the sensor's line-of-sight for the object to be resolved and distinguished against the celestial background. Cislunar-based sensors offer a solution to these issues by hosting a wider range of angles from which to view objects when compared to ground-based or near-Earth orbital optical sensors. Of note, AFRL's Space Vehicles Directorate has begun the transition of pushing the bounds of SDA into cislunar space with the creation of the Cislunar Highway Patrol System (CHPS) program. Once developed and fielded, this satellite system intends to perform the search, detect, track, and characterize missions within both cislunar space and the lunar exclusion zone, or a spatial region imperceptible to Earth-based sensors due to lunar albedo [38].

2.5 Debris Risk to Spacecraft

A primary risk to orbiting SDA spacecraft will be collisions with natural and manmade space debris. Risks from natural debris have been studied since the 1960s. Davidson and Sandorff [40] analyzed methods for shielding spacecraft against cislunar meteoroids in a 1963 NASA report, and Burbank, Cour-Palais, and McAllum [41] presented equations for the flux of meteoroids in cislunar space in their 1965 study. More recently, accumulations of natural cislunar debris at the Earth-Moon L_4 and L_5 Lagrange points called the Kordylewski clouds were studied by Slíz-Balogh, Barta, and Horváth [42]. The risks posed by these debris accumulations to spacecraft operating at L_4 and L_5 were analyzed by Boone and Bettinger [43].

The risks posed by artificial space debris have also been studied for many years, notably in Kessler's 1978 paper on the creation of a debris belt around Earth [44]. Some studies have investigated the potential risks from artificial debris beyond the near-Earth environment. Boone and Bettinger [45] analyzed the propagation of cislunar debris and risks to spacecraft for a variety of cislunar debris case studies. Spacecraft explosions at the collinear Earth-Moon Lagrange points have also been studied by Boone and Bettinger [46], as well as by Bandyopadhyay, Sharma, and Tewari [47]. Past studies of cislunar debris have found slight risks to spacecraft orbiting near Earth and to spacecraft operating elsewhere in the Earth-Moon system.

2.6 Summary

This chapter reviewed background information related to cislunar trajectory models, periodic orbits, debris risks, and space domain awareness. Based on the research conducted, the most applicable trajectory model is the CR3BP due to the simplicity, ability to easily generate periodic orbits, and ability to simulate periodic orbits with minimal to no ΔV required to model during the SDA simulations. However, it is still useful to observe how the Moon's eccentricity and Sun's gravity change the motion of the satellite, therefore cislunar periodic orbits are subject to these models to observe dynamical variations in trajectory and ultimately show how stabilizing controllers will be needed to maintain periodicity. Solar radiation would have an impact on ΔV required to maintain a trajectory, however, that is beyond the scope of this research. A review of past literature has also indicated that certain perturbations may be neglected due to their small impact on trajectory. For instance, Earth's oblateness effects and atmospheric drag are neglected since these perturbations significantly decrease at large distances from the Earth (what is seen by the majority of the orbits analyzed).

III. Methodology

3.1 Chapter Overview

The purpose of this chapter is to detail the methods used for analyzing cislunar periodic orbits. Specifically, this chapter will derive the dynamical models for trajectory propagation in cislunar space, present critical equations used for differential correction, and present the SDA model used in this work. The equations of motion for the CR3BP, ER3BP, and BCR4BP are developed and used to analyze dynamical properties of the Earth-Moon system in Sections 3.3, 3.4, and 3.5 respectively. Next, the equations used for differential correction in adjusting initial conditions and/or determining ΔV required in higher fidelity models are presented in Section 3.6. The methodology behind the construction of periodic orbits and case scenarios are presented in Section 3.7. The SDA model and equations used for simulations are presented in Section 3.9. The debris survivability model used in this research is presented in Section 3.10. The derivations and stability analysis in this chapter were presented at the 2021 AAS/AIAA Astrodynamics Specialist Conference [48].

3.2 Non-Dimensional "Canonical" Units

For all trajectory models, a form of non-dimensional units referred to as "canonical units" are used as to simplify the problem in terms of dimensional magnitude and allow trajectory solutions to be applied to any similar system with different gravitational parameters. Canonical units are such that the universal gravitational constant is defined as unity. In this canonical system, all distances are divided by a specified distance unit (DU) as shown in Eq. (1):

$$x_{nd} = \frac{x_d}{DU} \tag{1}$$

where x_{nd} is the non-dimensional position and x_d is the dimensional position. In the Earth-Moon system, the DU is the distance between the Earth and Moon.

A non-dimensional mass unit (MU) is created, defined as the sum of the Earth and Moon masses. All masses are thus divided by this sum as shown in Eq. (2)

$$\mu_i = \frac{m_i}{MU} = \frac{m_i}{m_e + m_m} \tag{2}$$

where μ_i and m_i are the non-dimensional mass parameter and dimensional mass of the i^{th} body respectively.

The result of non-dimensionalizing the problem is that the synodic period of the system is 2π. A non-dimensional time unit (TU) is created which is equal to the period of the system divided by the non-dimensional period equal to 2π as shown in Eq. (3):

$$TU = \frac{P_d}{2\pi} \tag{3}$$

where P_d is the dimensional period of the Moon about the Earth. This TU is then used to non-dimensionalize all times. For instance, the non-dimensional velocity is shown in Eq. (4):

$$\dot{r}_{nd} = \dot{r}_d \left(\frac{TU}{DU} \right) \tag{4}$$

The DU, TU, and MU used in this work are provided in the table below:

Table 1: Earth-Moon Canonical Characteristic Quantities

Parameter	Value
Distance Unit (DU)	390,877.4158212686 km
Time Unit (TU)	4.4527 days
Mass Unit (MU)	6.0459×10^{24} kg

3.3 The Circular Restricted Three-Body Problem

3.3.1 CR3BP Derivation and Equations of Motion

An Eulerian collinear configuration is used to derive the CR3BP equations of motion; however, another equally valid option is the Lagrangian triangular configuration. Koon et al. [1] presented a method for deriving the CR3BP equations of motion using Lagrangian mechanics. A modified version of this method which includes intermediate steps is presented in this work.

To begin, the system will consist of three bodies modeled as point masses: the Earth (E), Moon (M), and satellite (sat). The assumptions made during this derivation are as follows:

- m_e and m_m are considerably larger than m_{sat}, such that m_{sat} is negligible and does not affect the motion of the primary bodies
- E and M are in a circular, coplanar orbit about their barycenter

A non-dimensionalized mass parameter is defined as $\mu = m_m/(m_e + m_m)$ which will also act as the non-dimensionalized mass of M, while the non-dimensional mass of E is equal to $1 - \mu$. A coordinate system is created, herein defined as the synodic reference frame which is represented by $\hat{s}$ with coordinates (x, y, z). The synodic reference frame is depicted with respect to the inertial reference frame in Fig. 5. The inertial reference frame is represented by $\hat{I}$ with coordinates (X,Y,Z).

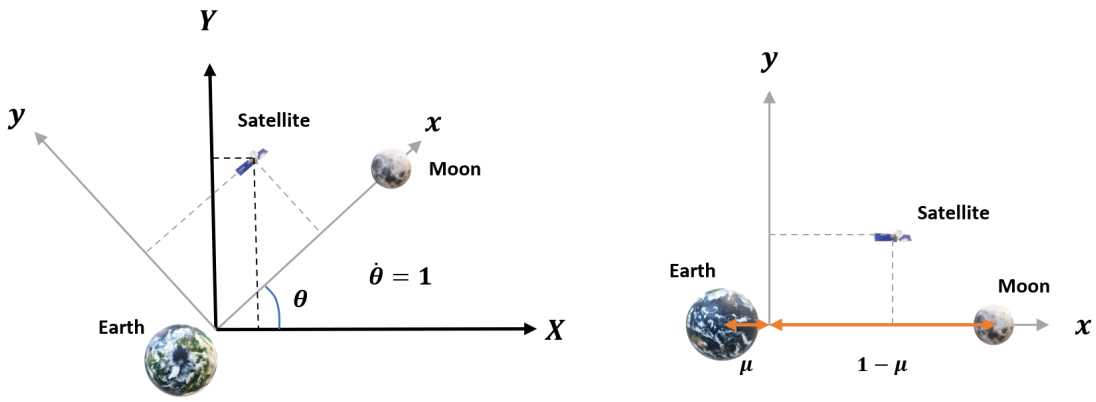

Figure 5: CR3BP Inertial (X,Y) and Synodic (x,y) Reference Frame

As shown in Fig 5, the synodic and inertial reference frames share the same origin: the E-M barycenter. In this coordinate system, the position of the satellite is ${}^{\hat{I}}\vec{r}_{sat} = (X, Y, Z)$ in the inertial reference frame and ${}^{\hat{s}}\vec{r}_{sat} = (x, y, z)$ in the synodic reference frame. The synodic frame is a rotating reference frame, which is rotated about the shared third axis (pointed out of the page) by an angle, θ, and has an x-axis passing through E and M. The angular velocity of the synodic reference frame with respect to the inertial reference frame is unity in non-dimensional coordinates. The fixed positions of E and M with respect to the origin in the synodic reference frame are ${}^{\hat{s}}\vec{r}_e = (-\mu, 0, 0)$ and ${}^{\hat{s}}\vec{r}_m = (1-\mu, 0, 0)$ respectively. For the purpose of simplification, the E and M non-dimensional mass parameters are set to $\mu_m = \mu$ and $\mu_e = 1 - \mu$. The scalar distance of *sat* with respect to E and M in the synodic reference frame is written as Eqs. (5) and (6), respectively:

$$r_{sat/e}^2 = (x + \mu_m)^2 + y^2 + z^2 \tag{5}$$

$$r_{sat/m}^2 = (x - \mu_e)^2 + y^2 + z^2 \tag{6}$$

With a coordinate transformation, the position of the satellite with respect to the

origin is expressed in the inertial reference frame using synodic frame coordinates as shown in Eq. (7):

$$ {}^{\hat{I}}\vec{r}_{sat} = \begin{bmatrix} X \\ Y \\ Z \end{bmatrix} = C^{\hat{I}\hat{s}} \begin{bmatrix} x \\ y \\ z \end{bmatrix} = \begin{bmatrix} x\cos\theta - y\sin\theta \\ x\sin\theta + y\cos\theta \\ z \end{bmatrix} \tag{7} $$

where

$$ C^{\hat{I}\hat{s}} = \begin{bmatrix} \cos\theta & -\sin\theta & 0 \\ \sin\theta & \cos\theta & 0 \\ 0 & 0 & 1 \end{bmatrix} \tag{8} $$

$C^{\hat{I}\hat{s}}$ is a 3-axis rotation direction cosine matrix transforming the synodic reference frame coordinates to be with respect to the inertial frame. Taking the derivative with respect to time (denoted by a dot above the coordinate), the velocity terms are obtained, shown in Eq. (9):

$$ {}^{\hat{I}}\dot{\vec{r}}_{sat} = \begin{bmatrix} \dot{X} \\ \dot{Y} \\ \dot{Z} \end{bmatrix} = \begin{bmatrix} (\dot{x} - y)\cos\theta - (x + \dot{y})\sin\theta \\ (x + \dot{y})\cos\theta + (\dot{x} - y)\sin\theta \\ \dot{z} \end{bmatrix} \tag{9} $$

Note that this operation could have occurred in the synodic reference frame; however, utilization of the transport theorem would then be required. Also, the time derivative of angle, θ, does not appear because the synodic period is 2π, making the synodic rate $\dot{\theta} = 1\frac{rad}{TU}$. Eq. (9) is often presented in literature with the absence of the trignometric functions since they will be canceled out during the utilization of Lagrange's equation of motion. The masses are modeled as point masses, thus providing only translational kinetic energy. Therefore, the specific kinetic energy of the satellite is calculated as

$$ T = \frac{1}{2}(\dot{X}^2 + \dot{Y}^2 + \dot{Z}^2) \tag{10} $$

substituting Eq. (9) into Eq. (10),

$$T = \frac{1}{2}\left(\Big[(\dot{x} - y)\cos\theta - (x + \dot{y})\sin\theta\Big]^2 + \Big[(x + \dot{y})\cos\theta + (\dot{x} - y)\sin\theta\Big]^2 + \dot{z}^2\right) \quad (11)$$

The specific potential energy for the satellite is expressed as

$$U = -\frac{\mu_e}{r_{sat/e}} - \frac{\mu_m}{r_{sat/m}} \quad (12)$$

where the datum is the satellite.

A system is holonomic if it is either unconstrained or its constraints (ϕ) may be described as a function of only the generalized coordinates and time (i.e. $\phi = \phi(q_1, ..., q_n, t)$). The CR3BP contains no constraints, therefore, it is a holonomic system with the full form of Lagrange's equation shown in Eq. (13) below:

$$\frac{d}{dt}\left(\frac{\partial L}{\partial \dot{q_k}}\right) - \frac{\partial L}{\partial q_k} = Q_{k(np)} \quad (13)$$

where q_k is the generalized coordinate, $Q_{k(np)}$ contains the non-potential generalized forces and L is the Lagrangian, defined as the kinetic energy minus the potential energy as shown in Eq. (14) below:

$$L = T - U \quad (14)$$

Substituting Eqs. (11) and (12) into Eq. (14) results in Eq. (15):

$$L = \frac{1}{2}\left[\Big[(\dot{x} - y)\cos\theta - (x + \dot{y})\sin\theta\Big]^2 + \Big[(x + \dot{y})\cos\theta + (\dot{x} - y)\sin\theta\Big]^2 + \dot{z}^2)\right] - \left(-\frac{\mu_e}{r_{sat/e}} - \frac{\mu_m}{r_{sat/m}}\right) \quad (15)$$

The CR3BP is without the presence of non-potential forces and, as a result, the non-potential generalized force term in Eq. (13) is equal to zero resulting in the following form of Lagrange's equation of motion:

$$\frac{d}{dt}\left(\frac{\partial L}{\partial \dot{q_k}}\right) - \frac{\partial L}{\partial q_k} = 0 \tag{16}$$

In the CR3BP, there are three generalized coordinates: x, y, and z, which form three equations of motion when using Lagrange's equation. Substituting Eq. (15) into Eq. (16) yields the following:

$$\frac{d}{dt}(\dot{x} - y) = x + \dot{y} - \frac{\mu_e\mu_m + \mu_e x}{((x+\mu_m)^2 + y^2 + z^2)^{3/2}} + \frac{\mu_e\mu_m - \mu_m x}{((x-\mu_e)^2 + y^2 + z^2)^{3/2}}$$

$$\frac{d}{dt}(\dot{y} + x) = y - \dot{x} - \frac{\mu_e y}{((x+\mu_m)^2 + y^2 + z^2)^{3/2}} - \frac{\mu_m y}{((x-\mu_e)^2 + y^2 + z^2)^{3/2}} \tag{17}$$

$$\frac{d}{dt}\dot{z} = -\frac{\mu_e z}{((x+\mu_m)^2 + y^2 + z^2)^{3/2}} - \frac{\mu_m z}{((x-\mu_e)^2 + y^2 + z^2)^{3/2}}$$

After further simplification of Eq. (17) and substituting in Eqs. (5) and (6), the CR3BP equations of motion are derived, shown in Eq. (18):

$$\ddot{x} = x + 2\dot{y} - \frac{(1-\mu)(x+\mu)}{r_{sat/e}^3} - \frac{\mu(x-1+\mu)}{r_{sat/m}^3}$$

$$\ddot{y} = y - 2\dot{x} - \frac{(1-\mu)y}{r_{sat/e}^3} - \frac{\mu y}{r_{sat/m}^3} \tag{18}$$

$$\ddot{z} = -\frac{(1-\mu)z}{r_{sat/e}^3} - \frac{\mu z}{r_{sat/m}^3}$$

Note that the use of transport theorem is not required due to the Lagrangian originating from energy terms which are inertial and scalar. It is common practice for the CR3BP equations of motion to be expressed in terms of a psuedo-potential function, Ω, as shown in Eq. (19):

$$\ddot{x} - 2\dot{y} = \Omega_x$$

$$\ddot{y} + 2\dot{x} = \Omega_y \tag{19}$$

$$\ddot{z} = \Omega_z$$

where Ω_x, Ω_y, and Ω_z are the partial derivatives with respect to x, y, and z of the potential function, respectively. The psuedo-potential function is Eq. (20):

$$\Omega = T_0 - U = \frac{1}{2}(x^2 + y^2) + \frac{1-\mu}{r_{sat/e}} + \frac{\mu}{r_{sat/m}} \tag{20}$$

where T_0 contains those terms in the kinetic energy which are solely a function of the generalized coordinates (x, y, z) and time (i.e. $T_0 = T(q_i, t)$). Constants used in the

CR3BP analysis are shown in Table 2:

Table 2: CR3BP Constants

Parameter	Value
G	$6.674 \times 10^{-20} \frac{Nkm^3}{kg^2}$
m_e	5.9724×10^{24} kg
m_m	7.346×10^{22} kg

Trajectories are determined by numerically integrating the equations of motions with a given set of initial conditions. Initial conditions consist of a starting position and velocity given in the form $\mathbf{X} = \begin{bmatrix} x_0 & y_0 & z_0 & \dot{x}_0 & \dot{y}_0 & \dot{z}_0 \end{bmatrix}$. In this research, MATLAB's ODE45 numerical integrator was used with absolute and relative tolerances ranging from 2.5×10^{-10} to 2.5×10^{-8} DU.

3.3.2 Analytical Mechanics and Stability of the CR3BP

Greenwood [49] defines a conservative system to be a system which meets the following criteria: The standard form of Lagrange's equation (holonomic or nonholonomic) applies, the Lagrangian function, L, is not an explicit function of time, and any constraint equations can be expressed in the differential form $\sum_{i=1}^{n} a_{ji} dq_i = 0$. With all of these conditions applying, the CR3BP is a conservative system where the Hamiltonian, $H = \sum_k \frac{\partial L}{\partial \dot{q}_k} \dot{q}_k - L$, is conserved (applicable for any conservative system). In the case of the CR3BP, the Jacobi integral (also called the Jacobi Constant) is conserved. Since the CR3BP does not contain any ignorable coordinates, the Jacobi Constant is the only constant of motion. The equation for the Jacobi Constant is shown in Eq. (21):

$$C = 2\Omega - \sqrt{\dot{x}^2 + \dot{y}^2 + \dot{z}^2} \tag{21}$$

The Jacobi Constant provides a relative negative measure of energy, meaning that a larger Jacobi Constant corresponds to less relative energy. The Jacobi Constant provides a means of depicting relative zero velocity surfaces and curves. For instance, by setting the velocity terms in Eq. (21) to zero, the zero velocity curves for all Jacobi Constant values may be plotted as shown in Fig. 6:

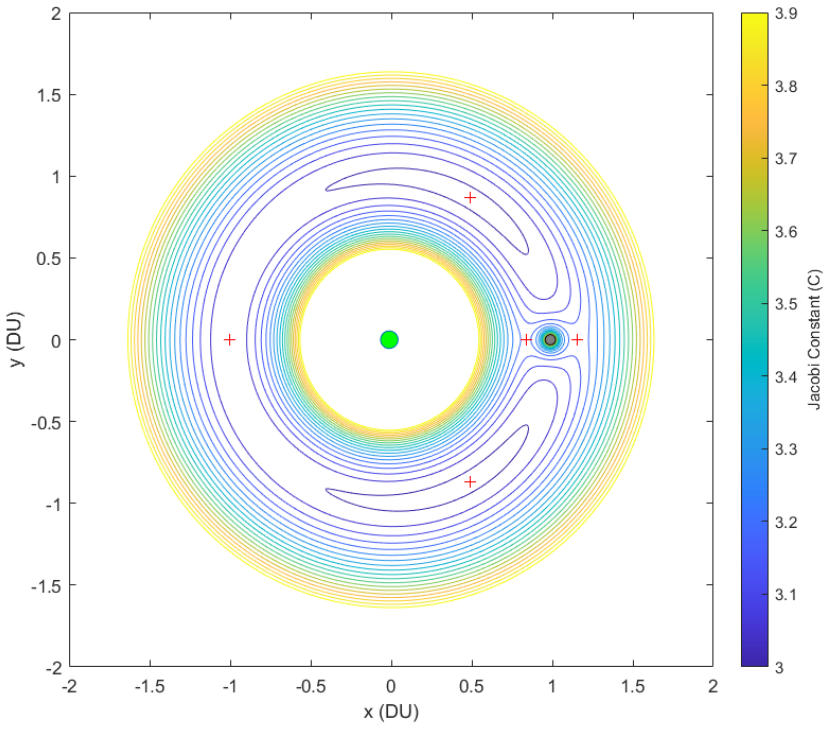

Figure 6: Earth-Moon CR3BP Zero Velocity Curves

A system of any order has an analytical solution if the constants of integration are greater than or equal to two times the degrees of freedom. In the CR3BP, there are a total of three degrees of freedom (three translational from the third body, *sat*). Since the number of constants of integration (one) are less than the degrees of freedom (three), there exists no closed form analytical solution to the CR3BP, and, as a result, numerical integration is required to produce approximate solutions.

There exist well known equilibrium solutions to the CR3BP in which the position of *sat* would appear to be unchanged with respect to time in the synodic reference frame. However, in the inertial reference frame, these points would appear to move in a perfectly circular orbit about the system barycenter. Often refereed to in literature as Lagrange points or Libration points, these points of stability are found by setting the velocity and acceleration terms in the equations of motion equal to zero. A simplification to this process is the realization that z is decoupled from x and y. Curtis [50] proves that for equilibrium conditions to hold true, the z-component of position must equal zero. In the CR3BP, there are 5 non-oscillatory equilibrium points, L_1, L_2, L_3, L_4, and L_5. The existence of these points was thought to be purely academic until 1906 with the discovery of the Trojan asteroids in the Sun-Jupiter L_4 and L_5 points [51]. As an example, the locations of the Lagrange points for the E-M system ($\mu = 0.012150586550569$) are shown in Table 3 and are drawn on the E-M synodic reference frame in Fig. 7 below:

Table 3: Non-Oscillatory Lagrange point locations in the Earth-Moon CR3BP Synodic Reference Frame

Lagrange point	x-position (DU)	y-position (DU)
L_1	0.8369	0
L_2	1.1557	0
L_3	-1.0050	0
L_4	0.4878	0.8660
L_5	0.4878	-0.8660

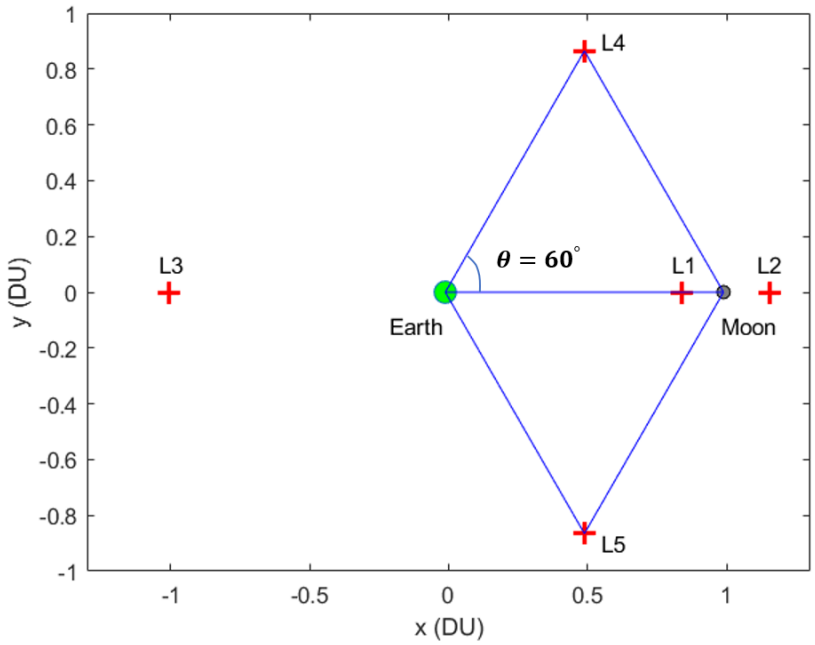

Figure 7: Lagrange Points for the Earth-Moon System in the Synodic Reference Frame

As shown in Fig. 7, equilateral triangles are formed between the E-M-$L4$ and E-M-$L5$ points, while the L_1,L_2, and L_3 Lagrange points are collinear with respect to the two primary masses. Through linear stability analysis, the stable and unstable nature of the Lagrange points may be proven [52]. The resulting conclusion is that the L_1,L_2 and L_3 Lagrange points are unstable; meanwhile, the L_4 and L_5 Lagrange points are infinitesimally stable as long as the following condition is met: $m_m < 0.0385(m_e+m_m)$ [7]. Essentially, there must be a significant mass difference between the two primary masses. According to Bialynicki-Birula, "the stability of motion near L_4 and L_5 is due to an intricate interplay between the potential forces and the Coriolis force" [53].

In this system, small differences in initial conditions lead to large differences in state, causing the CR3BP to be extremely chaotic. A commonly used stabilizing controller to mitigate this chaos is the use of propellant to adjust trajectory, more specifically referred to as change in velocity, ΔV. ΔV expenditure is generally the

limiting variable in space flight duration and longevity. The ΔV required for trajectory adjustments can be significantly reduced if scheduled early enough in the trajectory. For instance, Uphoff [54] showed that for his "BackFlip" orbit sequence, a ΔV of 10 m/s can contribute to a change the trajectory by more than 10,000 km when planned 10 to 15 hours in advance. In application to cycler orbits, Genova and Aldrin [55] showed how ΔV's as low as 19 m/s per 26.3 days would ensure close proximity Earth-Moon passes in their shamrock design. The result of this preparation provides a low cost means for shuttling humans and supplies to and from the Moon, a necessity when taking into consideration inevitably more frequent Earth-Moon travel due to future developments of a lunar base.

3.4 The Elliptical Restricted Three-Body Problem

The ER3BP is a deviation of the CR3BP, with the Moon now in an elliptical orbit about the Earth. This does two things: create a variable distance, r, between the primaries and create a variable angular velocity of the Earth and Moon about their barycenter, $\dot{v}$. The assumptions for the ER3BP are as follows:

- m_e and m_m are considerably larger than m_{sat}, such that m_{sat} is negligible and does not affect the motion of the primary bodies
- At initial time, $t = 0$, the primary bodies are at their minimum distance between one another

3.4.1 ER3BP Derivation and Equations of Motion

The ER3BP derivation appears in significantly fewer publications than the CR3BP, however, notable authors who have included this in their works include Szebehely [11, 56], Arenstorf [57], and Brouke [58]. The differences between the CR3BP and the ER3BP are highlighted in this derivation and additional equations presented. To start, the primary difference is that in the ER3BP, the non-dimensional distance between the primaries is now variable as represented in Eq. (22):

$$r = \frac{1 - e^2}{1 + e\cos v} = \frac{p}{1 + e\cos v} \tag{22}$$

where e is the eccentricity and v is the true anomaly of the Earth and Moon about their barycenter with respect to the synodic reference frame. Likewise, the non-dimensional angular velocity of the primaries about their common barycenter is now variable as represented in Eq. (23):

$$\dot{v} = \frac{\sqrt{1 - e^2}}{r^2} = \frac{\sqrt{p}}{r^2} \tag{23}$$

It is common practice to use a variant of the synodic reference frame which is now pulsating. To do this, all distances in the x-y plane are divided by the variable non-dimesnional distance between the primaries, r [58], as shown in Eq. (24) and (25)

$$x = \frac{x_{CR3BP}}{r} \tag{24}$$

$$y = \frac{y_{CR3BP}}{r} \tag{25}$$

where x_{CR3BP} and y_{CR3BP} are the non-dimensional coordinates in the CR3BP synodic

reference frame. Through this relationship, the distances of the primaries are now stationary in the new pulsating synodic reference frame with coordinates $(x_e, y_e) = (-\mu, 0)$ and $(x_m, y_m) = (1-\mu, 0)$.

The compilation of these changes transforms the ER3BP potential function ($\tilde{\Omega}$) into Eq (26):

$$\tilde{\Omega} = \frac{r}{p}\left[\frac{1}{2}(x^2+y^2) + \frac{\mu_e}{r_{sat/e}} + \frac{\mu_m}{r_{sat/m}} + \frac{1}{2}\mu_e\mu_m\right] \tag{26}$$

In order to simplify the equations of motion, it is common practice to make a change of independent variables from time, t, to true anomaly, v [56, 58]. This transformation is shown in Eq. (27):

$$dt = \frac{r^2}{\sqrt{p}}dv \tag{27}$$

The ER3BP equations of motion are shown in Eq. (28):

$$x'' - 2y' = \tilde{\Omega}_x$$

.

$$y'' + 2x' = \tilde{\Omega}_y \tag{28}$$

$$z'' = \tilde{\Omega}_z$$

where the superscripts ($'$) and ($''$) denote the first and second derivatives with respect to true anomaly. Expanding out the partial derivatives of the potential function in Eq. (28) yields the full form of the ER3BP equations of motion as shown in Eq. (29)

$$x'' = 2y' + \frac{r}{p}\left[x - \frac{(1-\mu)(x+\mu)}{r_{sat/e}^3} - \frac{\mu(x-1+\mu)}{r_{sat/m}^3}\right]$$

.

$$y'' = -2x' + \frac{r}{p}\left[y - \frac{(1-\mu)y}{r_{sat/e}^3} - \frac{\mu y}{r_{sat/m}^3}\right] \tag{29}$$

$$z'' = \frac{r}{p}\left[- \frac{(1-\mu)z}{r_{sat/e}^3} - \frac{\mu z}{r_{sat/m}^3}\right]$$

3.4.2 Analytical Mechanics and Stability of the ER3BP

In the previous section, it was explained that the CR3BP is a conservative system with the Jacobi integral being conserved, thus an integral of the motion and constant of integration. However, when elliptical motion is applied to the Moon, the system becomes non-conservative and the Jacobi integral is no longer an integral of the motion [57, 58].

Brouke notes another differing characteristic: the ER3BP does not include any natural families of periodic orbits in the sense of the circular problem [58]. Instead, any period of a periodic orbit must be a multiple of 2π [58]. Similar to the CR3BP, the ER3BP has a total of three degrees of freedom (three translational from the satellite). Since the number of constants of integration (zero) are less than the degrees of freedom (three), there exists no closed form analytical solution to the ER3BP, and, as a result, numerical integration is required to produce solutions.

The oscillatory motion of the primaries about the synodic frame x-axis causes stable points in the CR3BP to become unstable when applied to the ER3BP. Due to this, the ER3BP contains no points of stability.

3.5 The Bicircular Restricted Four-Body Problem

The BCR4BP is an extension of the CR3BP and consists of one body of negligible mass under the gravitational influence of three other bodies which are in a perfectly circular orbit around one another. This derivation specifically derives the equations of motion for the Moon in a circular orbit about the Earth, and the Earth-Moon barycenter in a circular orbit about the Sun, S.

3.5.1 BCR4BP Derivation and Equations of Motion

The BCR4BP is derived by making the following assumptions:

- The mass of *sat* is negligible compared to the masses of the other three bodies. Therefore, it's mass does not influence the motion of the three other bodies.
- E is in a circular orbit about S. M is in a circular orbit about E. Therefore angular velocities are constant.
- At the initial time, θ_e and θ_S are equal to zero.

Similar to the CR3BP, the equations of motion will be with respect to the E-M synodic reference frame. The diagram of the system is shown in Fig. 8 below:

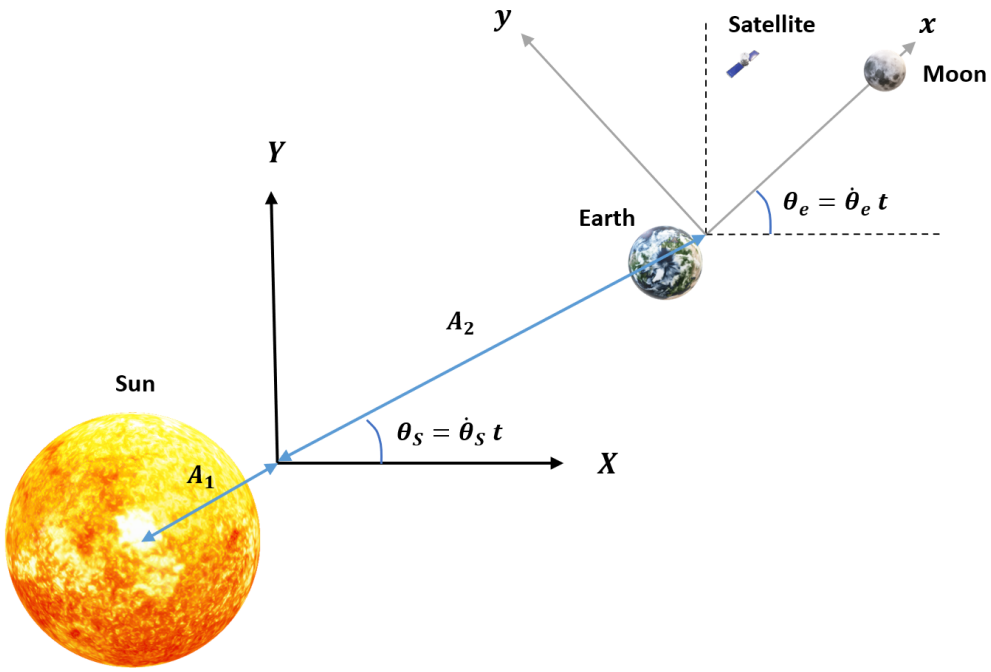

Figure 8: BCR4BP Inertial Reference frame (X,Y) and Synodic Reference Frame (x,y)

The angle between the E-M synodic reference frame and the inertial frame is $\theta_e = \dot{\theta}_e t$ while the angle the line connecting S and the synodic frame is $\theta_S = \dot{\theta}_S t$ where $\dot{\theta}_S$ and $\dot{\theta}_e$ are the angular rates of the S about the inertial reference frame and E about a shifted imaginary inertial reference frame (denoted by dotted lines in Fig. 8), respectively. A new non-dimensional mass parameter is created for S, $\mu_S = \frac{m_S}{m_e+m_m}$. A_1 represents the scalar non-dimensional distance between S and the inertial reference frame while A_2 represents the scalar non-dimensional distance between the inertial and synodic reference frames. Note that in this non-dimensional coordinate system $\dot{\theta}_e$ is unity, while $\dot{\theta}_S$ is less than one. The angles θ_S and θ_e are calculated from Eq. (30) and (31), respectively:

$$\theta_S = \dot{\theta}_S t = \sqrt{\frac{\mu_S + 1}{(A_1 + A_2)^3}}\, t \tag{30}$$

$$\theta_e = \dot{\theta}_e t = (1)t \tag{31}$$

The scalar distance of the satellite with respect to E, M, and S in the synodic reference frame (x,y) is written as Eqs. (32), (33), and (34) respectively:

$$r_{sat/e}^2 = (x+\mu)^2 + y^2 + z^2 \tag{32}$$

$$r_{sat/m}^2 = \big(x-(1-\mu)\big)^2 + y^2 + z^2 \tag{33}$$

$$r_{sat/S}^2 = (x-x_S)^2 + (y-y_S)^2 + z^2 \tag{34}$$

and x_S and y_S are the scalar distances of S in x and y coordinates with respect to the barycenter of the E-M synodic reference frame and are shown in Eqs. (35) and (36) respectively:

$$x_S = -(A_1 + A_2)\cos(\theta_S - \theta_e) \tag{35}$$

$$y_S = -(A_1 + A_2)\sin(\theta_S - \theta_e) \tag{36}$$

As with the CR3BP, a coordinate transformation is needed to avoid having to use the transport theorem when differentiating (either method is equally valid). This coordinate transformation is used to represent the satellite in the inertial reference frame whilst using synodic frame coordinates. An important distinction between the CR3BP and the BCR4BP is that differentiation in the BCR4BP must be made with the Inertial reference frame as the origin, which is now displaced from the synodic reference frame. This transformation is shown in Eq. (37):

$$ {}^{\hat{I}}\vec{r}_{sat} = \begin{bmatrix} X \\ Y \\ Z \end{bmatrix} = C^{\hat{I}\hat{s}} \begin{bmatrix} x \\ y \\ z \end{bmatrix} + {}^{\hat{I}}\vec{r}_{\hat{s}/\hat{I}} = \begin{bmatrix} x\cos\theta_e - y\sin\theta_e \\ x\sin\theta_e + y\cos\theta_e \\ z \end{bmatrix} + \begin{bmatrix} A_2\cos\theta_S \\ A_2\sin\theta_S \\ 0 \end{bmatrix} \tag{37} $$

where $C^{\hat{I}\hat{s}}$ is a 3-axis rotation direction cosine matrix transforming the system from the synodic reference frame to the inertial frame (see Eq. (8)) and ${}^{\hat{I}}\vec{r}_{\hat{s}/\hat{I}}$ is the vector distance of the synodic reference frame with respect to the inertial reference frame when viewed from the inertial reference frame. Taking the derivative with respect to time, the velocity terms are obtained, shown in Eq. (9):

$$ {}^{\hat{I}}\dot{\vec{r}}_{sat} = \begin{bmatrix} \dot{X} \\ \dot{Y} \\ \dot{Z} \end{bmatrix} = \begin{bmatrix} (\dot{x} - y)\cos\theta_e - (x + \dot{y})\sin\theta_e - A_2\dot{\theta}_S\sin\theta_S \\ (x + \dot{y})\cos\theta_e + (\dot{x} - y)\sin\theta_e + A_2\dot{\theta}_S\cos\theta_S \\ \dot{z} \end{bmatrix} \tag{38} $$

Just as with all dynamical models studied in this paper, the gravitational bodies are modeled as point masses, thus providing only translational kinetic energy. The specific kinetic energy of the BCR4BP is shown in Eq. (39):

$$ \begin{aligned} T = \frac{1}{2}\Bigg[&\Big[(\dot{x} - y)\cos\theta_e - (x + \dot{y})\sin\theta_e - A_2\dot{\theta}_S\sin\theta_S\Big]^2 \\ &+\Big[(x + \dot{y})\cos\theta_e + (\dot{x} - y)\sin\theta_e + A_2\dot{\theta}_S\cos\theta_S\Big]^2 + \dot{z}^2\Bigg] \end{aligned} \tag{39} $$

The potential energy of the BCR4BP differs from that of the CR3BP due to the addition of term due to the Sun's gravitational attraction. The potential energy of the BCR4BP is shown in Eq (40):

$$U = -\frac{1-\mu}{r_{sat/e}} - \frac{\mu}{r_{sat/m}} - \frac{\mu_S}{r_{sat/S}} \tag{40}$$

As with the CR3BP, the BCR4BP is holonomic with no non-potential forces for the same reason. Therefore, the following form of Lagrange's equation of motion is used:

$$\frac{d}{dt}\left(\frac{\partial L}{\partial \dot{q_k}}\right) - \frac{\partial L}{\partial q_k} = 0 \tag{41}$$

where the Lagrangian is the kinetic energy minus the potential energy as shown in Eq. (42):

$$L = T - U \tag{42}$$

Substituting Eqs. (39) and (40) into Eq. (42) and substituting the result into Eq. (41) and after simplification, the equations of motion for the BCR4BP are obtained as shown in Eq. (43):

$$\begin{aligned}
\ddot{x} &= x + 2\dot{y} - \frac{(1-\mu)(x+\mu)}{r_{sat/e}^3} - \frac{\mu(x-1+\mu)}{r_{sat/m}^3} - \frac{\mu_S(x-x_S)}{r_{sat/S}^3} + A_2\dot{\theta}_S^2\cos\left(\theta_S - \theta_e\right) \\
\ddot{y} &= y - 2\dot{x} - \frac{(1-\mu)y}{r_{sat/e}^3} - \frac{\mu y}{r_{sat/m}^3} - \frac{\mu_S(y-y_S)}{r_{sat/S}^3} + A_2\dot{\theta}_S^2\sin\left(\theta_S - \theta_e\right) \\
\ddot{z} &= -\frac{(1-\mu)z}{r_{sat/e}^3} - \frac{\mu z}{r_{sat/m}^3} - \frac{\mu_S z}{r_{sat/S}^3}
\end{aligned} \tag{43}$$

An important assumption to note in these equations is that at the beginning of propagation, $\theta_S = 0$; however, the Sun may be placed at any desired angle by adding the desired starting angle inside the trignometric functions of Eqs. (43), (35), and

(36). The BCR4BP uses the same values listed in Tables 1 and 2 with additional quantities listed in the table below:

Table 4: BCR4BP Non-dimensional Constants

Parameter	Value
A_1	0.00118
A_2	389.1725
μ_S	328900
$\dot{\theta}_S$	0.0747

The values in Table 4 are obtained by dividing the scalar distances, times, and masses by the values in Table 1.

3.5.2 Analytical Mechanics and Stability of the BCR4BP

In determining points of stability, the BCR4BP is closely approximated to a CR3BP where the first primary is the Sun and the second primary is the E-M barycenter. This is a conservative system where the Hamiltonian, $H=\sum_k \frac{\partial L}{\partial \dot{q}_k}\dot{q}_k - L$ is conserved. However, the Jacobi integral for this problem is slightly different in that it is taken with respect to a new BCR4BP rotating reference frame where the x-axis is aligned with the Sun and E-M barycenter and whose origin lies at the BCR4BP inertial reference frame. This would alter the equations of motion from those presented in Eq. (43). Just as with the cases of the CR3BP and ER3BP, there exists no closed form analytical solution to the BCR4BP, and, as a result, numerical integration is required to produce solutions.

The BCR4BP has 5 Lagrange points when approximated into a CR3BP. In this system, $\mu \approx 3.0394 \times 10^{-6}$. The L_4 ad L_5 points will still form an equilateral triangle as with the E-M CR3BP, however, the change in μ value causes a shift in the collinear L_1, L_2, and L_3 points. Due to the significant size difference of the Sun when com-

pared to the Earth and Moon, the L_1 and L_2 points are extremely close to the E-M barycenter. In this example, the BCR4BP Lagrange points were first calculated in a non-dimensional system where the sum of m_S, m_e, and m_m is one and then converted to the canonical units previously discussed by scaling up a factor of $A_1 + A_2$. These Lagrange points are taken with respect to the new BCR4BP rotating frame. The BCR4BP Lagrange points are shown in Table 5 and plotted on Fig. 9:

Table 5: Non-Oscillatory Lagrange point locations in the Sun-Earth-Moon BCR4BP Rotating Reference Frame

Lagrange point	x-position (DU)	y-position (DU)
L_1	$0.989987(A_1 + A_2)$	0
L_2	$1.010074(A_1 + A_2)$	0
L_3	$-1.000001(A_1 + A_2)$	0
L_4	$0.4878(A_1 + A_2)$	$0.8660(A_1 + A_2)$
L_5	$0.4878(A_1 + A_2)$	$-0.8660(A_1 + A_2)$

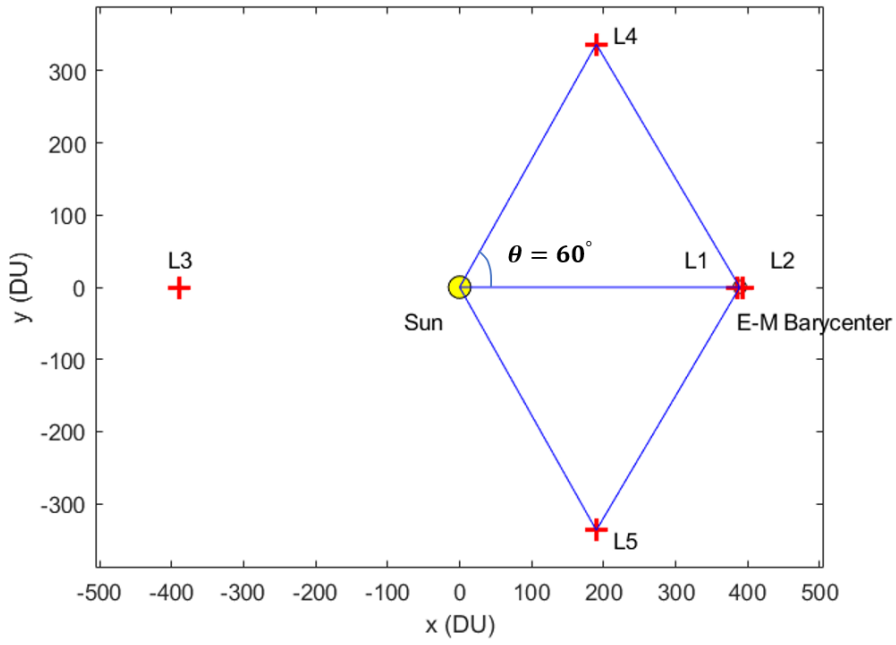

Figure 9: Lagrange Points for the Sun-Earth-Moon System in the BCR4BP Rotating Reference Frame

It is difficult to distinguish the L_1, L_2, and E-M barycenter in Fig. 9. Therefore, a close up image is presented in Fig. 10:

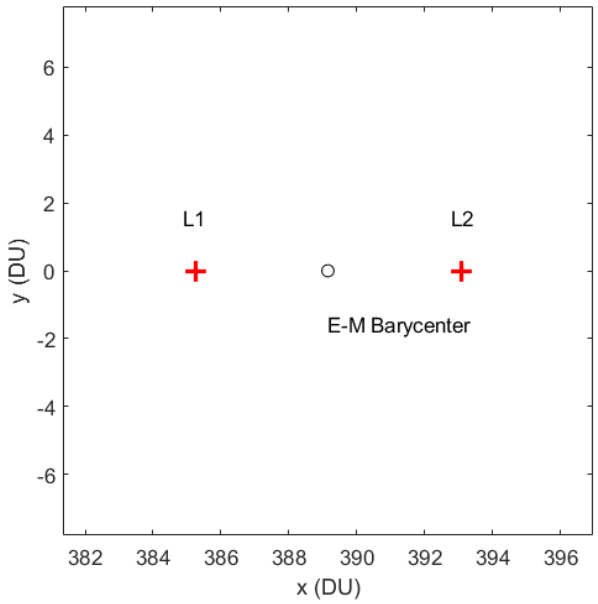

Figure 10: L_1 and L_2 Points for the Sun-Earth-Moon System in the BCR4BP Rotating Reference Frame

3.6 Differential Correction

Differential correction is used to correct a set of initial conditions to satisfy certain criteria. For instance, differential correction is used in targeting problems if a desired final position is specified. Differential correction, in terms of what was used in this work, is also used for transitioning a trajectory between different dynamical model (such as going from the CR3BP to the BCR4BP), or altering initial conditions to account for variations in the attributes of the system (such as a different μ value). The differential correction routines used in this work are outlined by Parker and Anderson [12], and described in detail below. The differential correction relies on the use of the state transition matrix (STM). The STM, Φ, provides mapping from the errors in the initial conditions to the errors in the final state at a particular time. To

begin describing the STM, a state vector $\mathbf{X}$ is defined as Eq. (44)

$$\mathbf{X} = \begin{bmatrix} x & y & z & \dot{x} & \dot{y} & \dot{z} \end{bmatrix} \tag{44}$$

The STM is then,

$$\Phi(t, t_0) = \frac{\partial \mathbf{X}(t)}{\partial \mathbf{X}(t_0)} = \begin{bmatrix} \Phi_{rr} & \Phi_{rv} \\ \Phi_{vr} & \Phi_{vv} \end{bmatrix} \tag{45}$$

and relates the final conditions $\left(\vec{r}(t) \text{ and } \vec{v}(t)\right)$ to the initial conditions $\left(\vec{r}_0 \text{ and } \vec{v}_0)\right)$ conditions by:

$$\begin{bmatrix} \delta\vec{r}(t) \\ \delta\vec{v}(t) \end{bmatrix} = \begin{bmatrix} \Phi_{rr} & \Phi_{rv} \\ \Phi_{vr} & \Phi_{vv} \end{bmatrix} \begin{bmatrix} \delta\vec{r}_0 \\ \delta\vec{v}_0 \end{bmatrix} \tag{46}$$

in which Φ_{rr}, Φ_{rv}, Φ_{vr}, and Φ_{vv} are $3x3$ sub-matrices which comprise the 6×6 STM. Note that the STM directly maps the deviations or errors in the state. In order to solve for the STM which maps $\mathbf{X}(t)$ to $\mathbf{X}(t_0)$, the STM is propagated for time t via the relationship in Eq. (47):

$$\dot{\Phi}(t, t_0) = A(t)\Phi(t, t_0) \tag{47}$$

where the initial condition for Φ is the identity martix as shown in Eq. 48:

$$\Phi(t_0, t_0) = \boldsymbol{I} = \begin{bmatrix} 1 & 0 & 0 & 0 & 0 & 0 \\ 0 & 1 & 0 & 0 & 0 & 0 \\ 0 & 0 & 1 & 0 & 0 & 0 \\ 0 & 0 & 0 & 1 & 0 & 0 \\ 0 & 0 & 0 & 0 & 1 & 0 \\ 0 & 0 & 0 & 0 & 0 & 1 \end{bmatrix} \tag{48}$$

The A Matrix in Eq. (47) is solved by evaluating Eq. (49):

$$A(t) = \frac{\partial \dot{\mathbf{X}}(t)}{\partial \mathbf{X}(t)} = \begin{bmatrix} a_{11} & a_{12} \\ a_{21} & a_{22} \end{bmatrix} \tag{49}$$

where

$$a_{11} = \begin{bmatrix} \frac{\partial \dot{x}}{\partial x} & \frac{\partial \dot{x}}{\partial y} & \frac{\partial \dot{x}}{\partial z} \\ \frac{\partial \dot{y}}{\partial x} & \frac{\partial \dot{y}}{\partial y} & \frac{\partial \dot{y}}{\partial z} \\ \frac{\partial \dot{z}}{\partial x} & \frac{\partial \dot{z}}{\partial y} & \frac{\partial \dot{z}}{\partial z} \end{bmatrix} \qquad a_{12} = \begin{bmatrix} \frac{\partial \dot{x}}{\partial \dot{x}} & \frac{\partial \dot{x}}{\partial \dot{y}} & \frac{\partial \dot{x}}{\partial \dot{z}} \\ \frac{\partial \dot{y}}{\partial \dot{x}} & \frac{\partial \dot{y}}{\partial \dot{y}} & \frac{\partial \dot{y}}{\partial \dot{z}} \\ \frac{\partial \dot{z}}{\partial \dot{x}} & \frac{\partial \dot{z}}{\partial \dot{y}} & \frac{\partial \dot{z}}{\partial \dot{z}} \end{bmatrix}$$

$$a_{21} = \begin{bmatrix} \frac{\partial \ddot{x}}{\partial x} & \frac{\partial \ddot{x}}{\partial y} & \frac{\partial \ddot{x}}{\partial z} \\ \frac{\partial \ddot{y}}{\partial x} & \frac{\partial \ddot{y}}{\partial y} & \frac{\partial \ddot{y}}{\partial z} \\ \frac{\partial \ddot{z}}{\partial x} & \frac{\partial \ddot{z}}{\partial y} & \frac{\partial \ddot{z}}{\partial z} \end{bmatrix} \qquad a_{22} = \begin{bmatrix} \frac{\partial \ddot{x}}{\partial \dot{x}} & \frac{\partial \ddot{x}}{\partial \dot{y}} & \frac{\partial \ddot{x}}{\partial \dot{z}} \\ \frac{\partial \ddot{y}}{\partial \dot{x}} & \frac{\partial \ddot{y}}{\partial \dot{y}} & \frac{\partial \ddot{y}}{\partial \dot{z}} \\ \frac{\partial \ddot{z}}{\partial \dot{x}} & \frac{\partial \ddot{z}}{\partial \dot{y}} & \frac{\partial \ddot{z}}{\partial \dot{z}} \end{bmatrix}$$

There are certain properties which the Φ matrix possesses such as:

$$\Phi(t_2, t_0) = \Phi(t_2, t_1)\Phi(t_1, t_0) \tag{50}$$

$$\Phi^{-1}(t, t_0) = \Phi(t_0, t) \tag{51}$$

With knowledge of the STM, differential correction may be performed via the single and multiple shooting methods. For both methods, a set number of patchpoints are chosen which allows for convergence of the algorithm outlined in Fig. 11.

3.6.1 Single Shooting Method

The first step in differential correction is the single shooting method. In the Single Shooting method the patchpoint positions and times to travel between patchpoints are held constant whilst the velocity is varied to a converged solution as to reach a desired position in a desired amount of time. It is crucial that the initial velocity guess is close to the solution or else the velocity will not converge. Likewise, orbital

dynamics in cislunar periodic orbits are extremely chaotic, thus it is important to impose enough patchpoints as to allow for a converged solution (especially around sharp "turns" in the trajectory). The algorithm for utilizing this single shooting method is shown in Fig. 11:

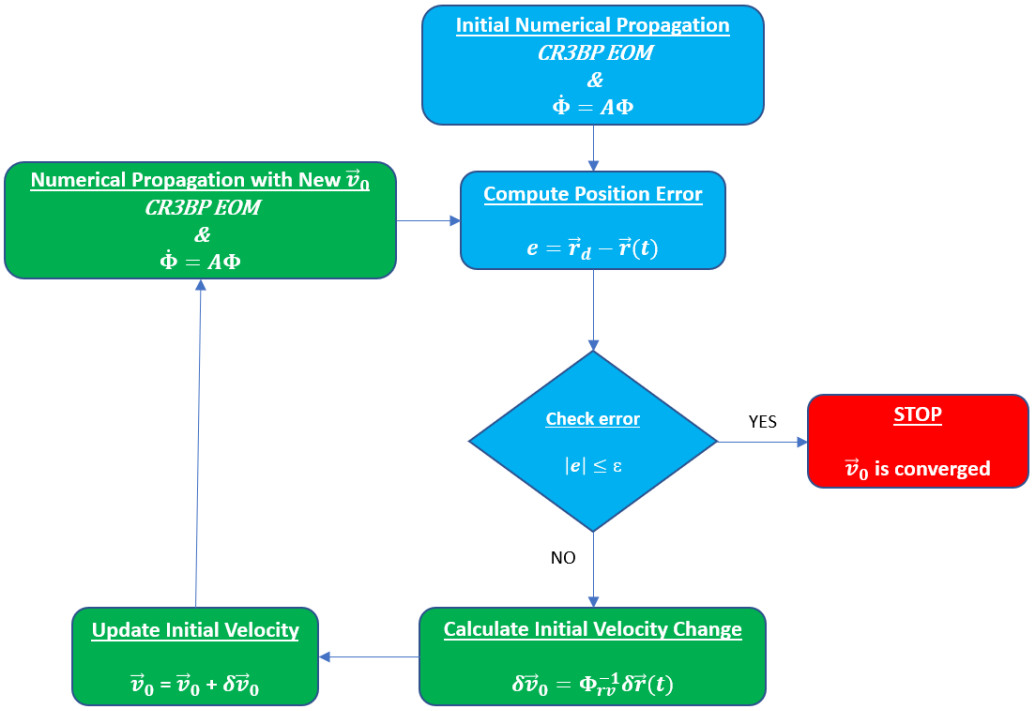

Figure 11: Single Shooting Method Algorithm

In the preceding algorithm, ε is the error tolerance, $\vec{r}_d$ is the desired position, and the equation for the initial velocity change is calculated from Eq. (46) and shown in Eq. (52):

$$\delta\vec{v}_0 = \Phi_{rv}^{-1}\delta\vec{r}(t) \tag{52}$$

If using the single shooting method for multiple points in a trajectory, then it is critical to remember to propagate each respective point at the start time in the

overall trajectory, as opposed to starting each point at t = 0.

3.6.2 Multiple Shooting Method

The multiple shooting method is used after the single shooting method to adjust position and times. The change in patchpoint position and times for a three-pathchpoint segment is calculated from Eq. (53):

$$\begin{bmatrix} \delta R_1 \\ \delta t_1 \\ \delta R_2 \\ \delta t_2 \\ \delta R_3 \\ \delta t_3 \end{bmatrix} = M^T (M M^T)^{-1} \left[\delta \Delta V_2 \right] \tag{53}$$

The goal with Eq. (53) is to reduce ΔV_2 to zero. Note that $\Delta V_2 = V_2^+ - V_2^-$ where the the solo superscripts "-" and "+" represent the incoming and outgoing parameters at a particular patchpoint. The M matrix is calculated by Eq. (54):

$$M = \begin{bmatrix} \frac{\partial \Delta V_2}{\partial R_1} & \frac{\partial \Delta V_2}{\partial t_1} & \frac{\partial \Delta V_2}{\partial R_2} & \frac{\delta \partial V_2}{\partial t_2} & \frac{\partial \Delta V_2}{\partial R_3} & \frac{\partial \Delta V_2}{\partial t_3} \end{bmatrix} \tag{54}$$

where

$$\frac{\partial \Delta V_2}{\partial R_1} = -\frac{\partial V_2^-}{\partial R_1^+} = -B_{12}^{-1} \qquad \frac{\partial \Delta V_2}{\partial t_1} = -\frac{\partial V_2^-}{\partial t_1^+} = B_{12}^{-1} V_1^+$$

$$\frac{\partial \Delta V_2}{\partial R_2} = -\frac{\partial V_2^+}{\partial R_2^-} - \frac{\partial V_2^-}{\partial R_2^+} = -B_{32}^{-1} A_{32} + B_{12}^{-1} A_{12}$$

$$\frac{\partial \Delta V_2}{\partial t_2} = \frac{\partial V_2^+}{\partial t_2^-} - \frac{\partial V_2^-}{\partial t_2^+} = B_{32}^{-1} A_{32} V_2^+ - B_{12}^{-1} A_{12} V_2^-$$

$$\frac{\partial \Delta V_2}{\partial R_3} = \frac{\partial V_2^+}{\partial R_3^-} = B_{32}^{-1} \qquad \frac{\partial \Delta V_2}{\partial t_3} = \frac{\partial V_2^+}{\partial t_3^-} = -B_{32}^{-1} V_3^-$$

which utilizes the notation in Eq. (55):

$$\begin{bmatrix} \delta R_2^- \\ \delta V_2^- \end{bmatrix} = \begin{bmatrix} A_{21} & B_{21} \\ C_{21} & D_{21} \end{bmatrix} \begin{bmatrix} \Delta R_1^+ \\ \Delta V_1^+ \end{bmatrix} \tag{55}$$

where the A_{21}, B_{21}, C_{21} and D_{21} sub-matrices form the STM mapping from patchpoint 1 to 2. Finally, to determine the new positions add the variation in position obtained to the initial position as shown in Eqs. (56) and (57):

$$\vec{r}_{1new} = \vec{r}_{1old}^{+} + \delta \vec{r}_1 \tag{56}$$

$$\vec{r}_{2new} = \vec{r}_{2old}^{-} + \delta \vec{r}_2 \tag{57}$$

This process describes the multiple shooting method for 3 points; for more than 3 points, then a matrix form shown in Eq. (58) may be used:

$$\begin{bmatrix} \delta R_1 \\ \delta t_1 \\ \delta R_2 \\ \delta t_2 \\ \delta R_3 \\ \delta t_3 \\ \delta R_4 \\ \delta t_4 \\ \vdots \\ \delta R_n \\ \delta t_n \end{bmatrix} = M^T (M M^T)^{-1} \begin{bmatrix} \delta \Delta V_2 \\ \delta \Delta V_3 \\ \vdots \\ \delta \Delta V_{n-1} \end{bmatrix} \tag{58}$$

From Eq. (58), the matrix M is equal to

$$M = \begin{bmatrix} \frac{\partial \Delta V_2}{\partial R_1} & \frac{\partial \Delta V_2}{\partial t_1} & \frac{\partial \Delta V_2}{\partial R_2} & \frac{\partial \Delta V_2}{\partial t_2} & \frac{\partial \Delta V_2}{\partial R_3} & \frac{\partial \Delta V_2}{\partial t_3} & 0_{3x3} & 0_{3x1} & ... & 0_{3x3} & 0_{3x1} \\ 0_{3x3} & 0_{3x1} & \frac{\partial \Delta V_3}{\partial R_2} & \frac{\partial \Delta V_3}{\partial t_2} & \frac{\partial \Delta V_3}{\partial R_3} & \frac{\partial \Delta V_3}{\partial t_3} & \frac{\partial \Delta V_3}{\partial R_4} & \frac{\partial \Delta V_3}{\partial t_4} & ... & 0_{3x3} & 0_{3x1} \\ \vdots & \vdots & \vdots & \vdots & \vdots & \vdots & \vdots & \vdots & \vdots & \vdots & \vdots \\ 0_{3x3} & 0_{3x1} & 0_{3x3} & 0_{3x1} & ... & \frac{\partial \Delta V_{n-1}}{\partial R_{n-2}} & \frac{\partial \Delta V_{n-1}}{\partial t_{n-2}} & \frac{\partial \Delta V_{n-1}}{\partial R_{n-1}} & \frac{\partial \Delta V_{n-1}}{\partial t_{n-1}} & \frac{\partial \Delta V_{n-1}}{\partial R_n} & \frac{\partial \Delta V_{n-1}}{\partial t_n} \end{bmatrix} \tag{59}$$

where 0_{3x3} is a 3x3 matrix of zeros and 0_{3x1} is a 3x1 matrix of zeros. For correcting the position, the following is used:

$$\vec{r}_{n-new} = \vec{r}^{+}_{n-old} + \delta\vec{r}_n \tag{60}$$

3.7 Periodic Orbit Construction

Due to the complexities in dynamics and chaos in higher fidelity trajectory models, periodic orbits are mainly found in the CR3BP or lower fidelity models such as the 2BP. In the CR3BP, the simplest way of creating or "discovering" these periodic orbits is to start with an arbitrary initial position along the x-axis of the synodic reference frame. The y-velocity is then adjusted until the trajectory closes in a periodic manner. Thus, the initial conditions will take the form of $\mathbf{X} = (x_0, 0, 0, 0, \dot{y}_0, 0)$. Without use of code which finds a converged near-by solution, this process becomes an artful task which takes some skill, knowledge, and, above all, patience. It is possible to have multiple periodic orbits lie in the same initial position, with varying velocities. To demonstrate this as an example, the initial position of $x = 1.15$ will be taken. By adjusting the y-velocities, three periodic orbits in the CR3BP ($\mu = 0.012150584673414$) are created, shown in Fig. 12 with initial conditions shown in Table 6:

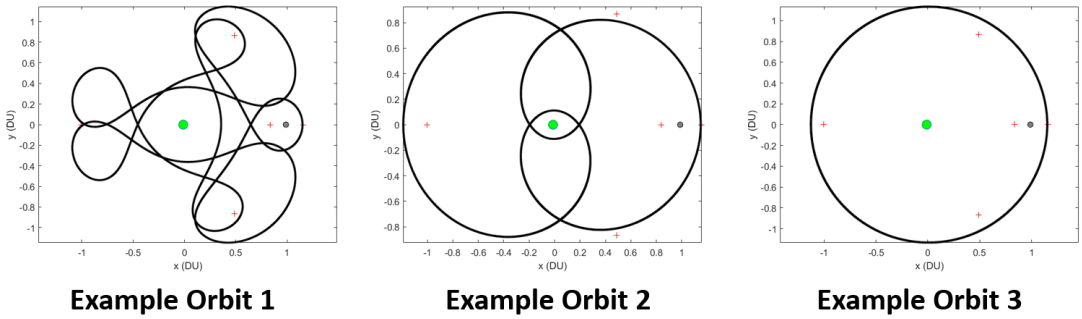

Figure 12: Periodic Orbit Construction Example (x=1.15)

Table 6: Periodic Orbit Construction Example (Fig. 12) Initial Conditions

Periodic Orbit Ex.	x_0	$\dot{y}_0$	T_0
1	1.15	-0.5724	30.8
2	1.15	-1.585	6.4
3	1.15	-2.112	3.5

Throughout the construction of cislunar periodic orbits it was observed that significantly more chaos was present when either of the following conditions were met:

- negative x_0-position and negative y_0-velocity
- positive x_0-position and positive y_0-velocity

When either of the above conditions were met, it was common for the trajectory to spiral out of the Earth-Moon system. Therefore, for nearly all of the orbits analyzed in this work, the initial conditions consisted of initial position and velocities which were opposite in sign. Figs. 12, 18, 19 (Orbits 7-9), and 36 all consist of periodic orbits that were discovered during this research. Other miscellaneous periodic orbits discovered are shown in Fig. 13 with the corresponding initial conditions shown in Table 7.

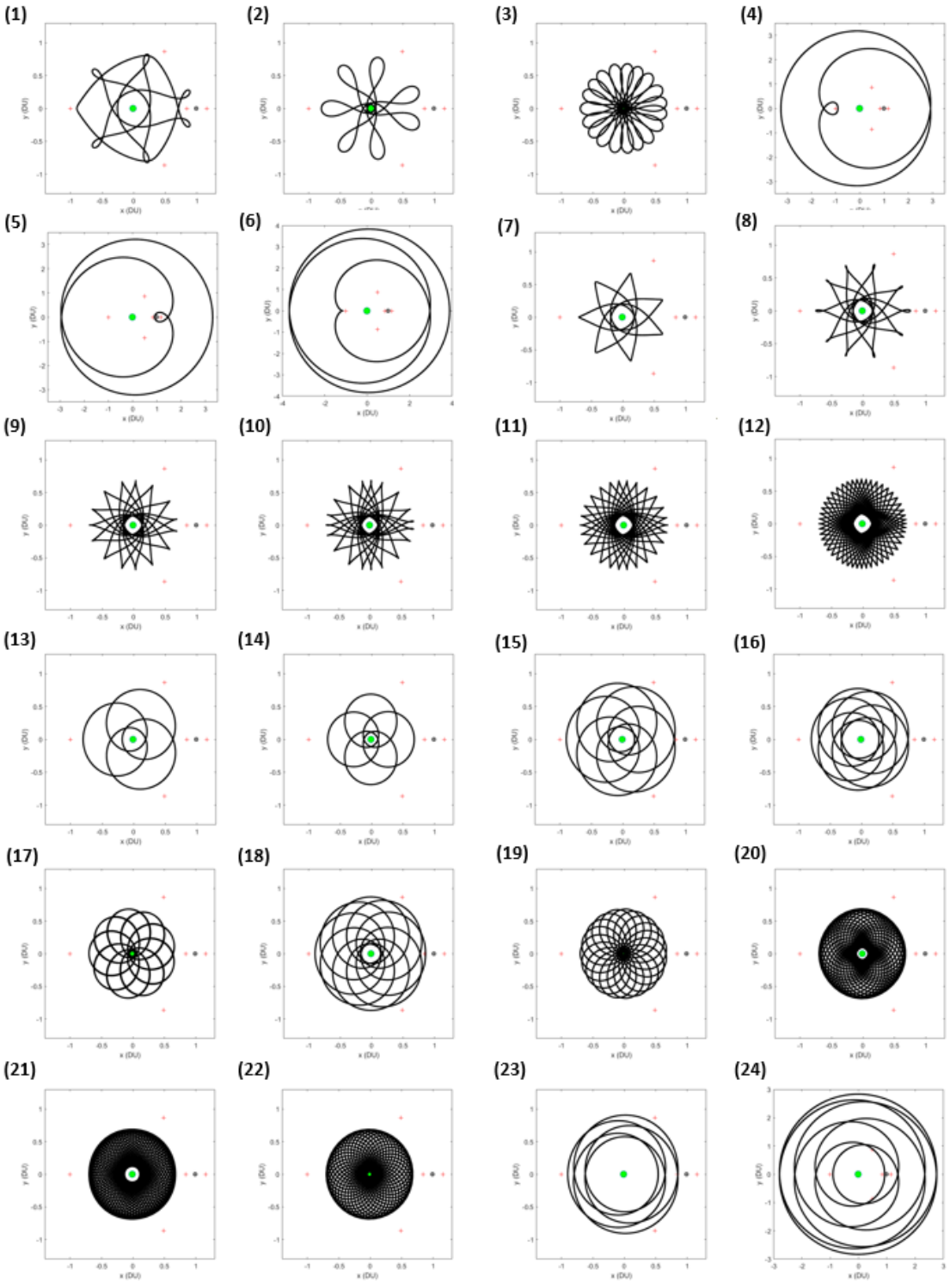

Figure 13: Miscellaneous Discovered Periodic Orbits

Table 7: Miscellaneous Discovered Periodic Orbits Initial Conditions

Misc Orbit	x_0	$\dot{y}_0$	T_0
1	-0.9	-0.099452	29.5
2	-0.8	0.38	12.6
3	-0.7	0.3865	25.2
4	-0.902627797776441	-0.42142	18.9
5	0.902627797776441	0.691	17.6
6	-1.15	-0.010244	25.2
7	-0.7	-0.065	12.5
8	-0.75	0.0794	18.9
9	-0.7	0.0212	25.1
10	-0.7	0.04115	31.4
11	-0.7	0.0085	44
12	-0.7	0.00074	81.9
13	-0.8	1.45	6.3
14	-0.7	1.2903	6.3
15	-0.9	1.51	12.45
16	-0.8	1.605	12.47
17	-0.7	1.099	50
18	-0.9	1.446	18.8
19	-0.7	0.959	40.0
20	-0.7	1.26	57.0
21	-0.7	1.35	69.0
22	-0.7	1.07	56.5
23	-0.9	1.82	12.2
24	-0.9	2.20583	31.85

Note that the initial conditions in Table 7 take the form of $\mathbf{X} = [x_0, 0, 0, 0, \dot{y}_0, 0]^T$. The orbits in Figs. 12, 13, 18, 19, and 36 may be used for a wide swath of missions,

not limited to SDA. Such missions include re-supply, personnel transport, and space-based infrastructure development. In particular, orbits which feature close proximity passes of both gravitational bodies, identified herein as cycler orbits, may be extremely useful for such mission sets. It may also be effective to transfer between these orbits by utilizing the Lagrange points.

3.8 Families of Halo Orbits

In preparation for this work, families of halo orbits about the L_1 and L_2 Lagrange points were created ($\mu = 0.012150584673414$). By taking advantage of the symmetry of the CR3BP about the x-z plane, initial conditions can be formed for periodic orbits about the collinear Lagrange points; for the halo orbits, the initial conditions take the form of $\mathbf{X} = [x_0, 0, z_0, 0, \dot{y}_0, 0]^T$. Following the method laid out by Grebow (2006), the bifurcation with the planar Lyapunov orbits is used as the starting point for forming halo orbits (orbit 1 in Tables 8 and 9) [2]. Using a continuation method, ever increasing z_0 values are found for the halo orbit initial conditions according to:

$$\mathbf{X}^{k+1} = \mathbf{X}^k + d\,\Delta\mathbf{X} \tag{61}$$

where $\Delta\mathbf{X} = [0,\ 0,\ 1,\ 0,\ 0,\ 0]^T$ represents a shift in the z direction at each step [2, 12]. After each shift, the new initial condition is corrected to form the periodic Halo Orbit about L_1 or L_2 for the given z_0 value. The initial conditions for some members of the L_1 and L_2 Northern Halo Orbit families are given in Tables 8 and 9.

Table 8: Family of L_1 Northern Halo Orbits

Halo Orbit	x_0	z_0	$\dot{y}_0$	T_0
1	0.823400	0	0.126232	2.742912
2	0.823391	0.024	0.135374	2.746862
3	0.823776	0.048	0.157540	2.757428
4	0.825081	0.072	0.184597	2.771716
5	0.827480	0.096	0.211253	2.784409
6	0.830970	0.120	0.234856	2.785808

Table 9: Family of L_2 Northern Halo Orbits

Halo Orbit	x_0	z_0	$\dot{y}_0$	T_0
1	1.180899	0	-0.155856	3.415531
2	1.180801	0.01	-0.156434	3.414713
3	1.180503	0.02	-0.158134	3.412257
4	1.179992	0.03	-0.160864	3.408149
5	1.179246	0.04	-0.164483	3.402362
6	1.178242	0.05	-0.168829	3.394850

Southern Halo Orbits can be formed in the same manner by using $\Delta\mathbf{X} = [0,\ 0,\ -1,\ 0,\ 0,\ 0]^T$. For the analysis performed in this paper, halo orbit 6 from Table 8 and halo orbit 6 from Table 9 will be used as Target orbits.

3.9 Space Domain Awareness Simulation Model

To determine if the Target satellites are visible, visual magnitude (M_v) of the vehicles is calculated. The first step in calculating visual magnitude is to determine the phase (or Sun) angle at every point in time. The phase angle is calculated from Eq. (62):

$$\phi = \arccos\left(\frac{\vec{r}_{Tar/sat} \cdot \vec{r}_{Tar/S}}{r_{Tar/sat} r_{Tar/S}}\right) \tag{62}$$

where $\vec{r}_{Tar/sat}$ is the vector position of the target with respect to the sensor bearing satellite, and $\vec{r}_{Tar/S}$ is the vector position of the target with respect to the Sun. In this analysis, the target is modeled as a sphere; therefore, the phase function, Ψ, becomes:

$$\Psi = \frac{2}{3}\frac{C_d}{\pi}(\sin\phi + (\pi - \phi)\cos\phi) \tag{63}$$

where C_d is the coefficient of diffuse reflection which is a function of the mean wavelength. The visual magnitude, M_v, is then calculated by:

$$M_v = -26.8 - 2.5\log_{10}\left(\frac{A}{r^2_{Tar/sat}}\Psi\right) \tag{64}$$

where A is the surface area of the Target. The visual magnitude is, counterintuitively, measured on a logarithmic scale in which lower numbers indicate brighter objects. For comparison, Table 10 lists common visual magnitudes [59].

Table 10: Common Visual Magnitudes

Object	M_v
Sun from Earth	-26.8
Full Moon from Earth	-12.5
Jupiter at brightest from Earth	-2.7
Polaris from Earth	1.99
Naked Eye Limit Ability	6.0
Pluto from Earth	15.1
Hubble Space Telescope Ability	31

For this analysis, a Target is considered visible when it has a visual magnitude

of $M_v \leq 18.5$. Constants used in the SDA analysis were area of the Target, A, and coefficient of diffuse reflection, C_d which were 2.25 m^2 and 0.86, respectively. It is critical to note that A is converted to kilometers before calculating M_v to match units of r^2.

Exclusion angles are also considered in this analysis, which are the angles between the satellite-Target and satellite-gravitational body. When the angle between the satellite-Target and satellite-gravitational body vectors are less than these exclusion angles, the target is assumed to be imperceptible due to the Sun's reflection onto the respective gravitational body. Table 11 shows the exclusion angles used:

Table 11: Exclusion Angles

Object	Value	M_v
Sun	30°	35
Earth	15°	35
Moon	6°	35

For graphical purposes, high M_v values are assigned to angles which are less than the exclusion angle as shown in Table 11. For instance, a M_v value of 35 would correspond to a scenario in which the Target is imperceptible due to either the Sun, Earth, or Moon's exclusion angle.

3.10 Artificial Debris Propagation Analysis

The methodology used for determining risk to spacecraft with respect to debris impact as discussed by Boone [3] was used for the debris propagation described in this section. The simulation results for this analysis are showcased in Chapter VI.

3.10.1 Debris Model

Debris will be assumed to be generated by a catastrophic battery explosion, and the statistical catastrophic spacecraft mishap model developed by Boone and Bettinger [45] based on the NOAA 16 satellite battery explosion will be used to determine the particle masses (m) and velocities (v) resulting from the explosion. All particle masses will be generated by selecting random numbers from a lognormal distribution with mean of -1.7285 and standard deviation of 1.4511. Given a constant value for particle kinetic energy (KE), the particle speed can be calculated from particle mass as Eq (65):

$$v = \sqrt{\frac{2}{m} KE} \tag{65}$$

A particle kinetic energy of about 580 J will be used based on the median kinetic energies of particles released from the NOAA 16 battery explosion. All particles will be assigned a random direction for their velocity vector to represent an omnidirectional explosion. Typically, this model results in 2,500 to 3,000 debris particles that are given an average ΔV of approximately 100 m/s.

3.10.2 Survivability Model

The survivability model used by Boone and Bettinger [45] for analyzing survivability of cislunar spacecraft is applied to evaluate the risks due to debris for this research. This model is a variation on the Poisson aircraft survivability developed by Ball [60]. In this model, the debris number density ρ within a spherical "danger zone" with volume V_{DZ} surrounding a notional spacecraft threatened by debris is used to calculate the probability of hazard to the notional spacecraft. A smaller spherical region called the "hazard zone" with volume V_{HZ} bounds this notional spacecraft. The radii of the danger zone and hazard zone are $10,000$ km and 500 m respectively.

The expected number of hits, E, to this hazard zone is given by Eq. (66):

$$E = \rho V_{HZ} \tag{66}$$

Any particle that enters the hazard zone sphere that would cause critical damage to the spacecraft if it struck the spacecraft is considered to significantly threaten the spacecraft and represents a "hazard." A diagram illustrating the hazard zone and danger zone is shown in Fig. 14:

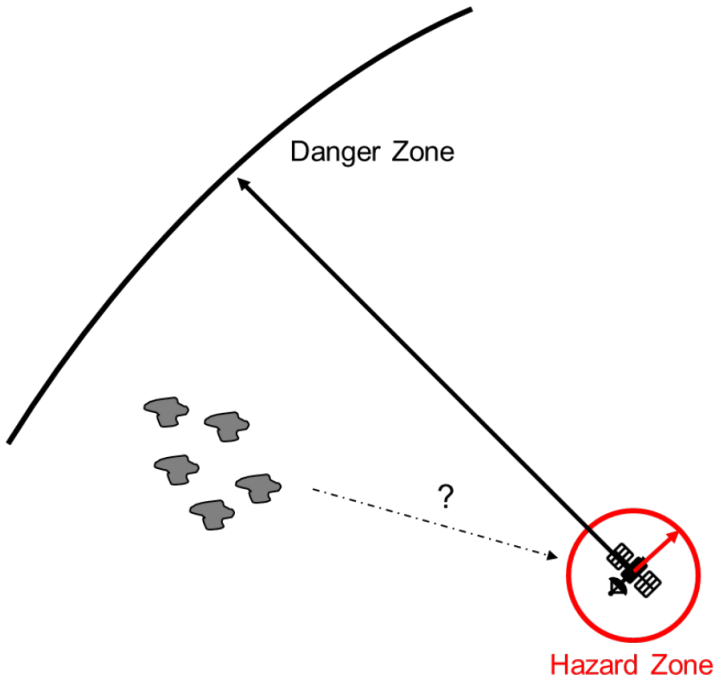

Figure 14: Diagram Showing Hazard Zone and Danger Zone for Survivability Model

The probability of causing critical damage given that an impact occurs is the probability of kill with a hit, $P_{K|H}$. $P_{K|H}$ is determined using a vulnerability model that depends on the properties of the debris in the vicinity of the spacecraft, which is discussed in greater detail in the next section. Given a value for $P_{K|H}$, the instantaneous

probability of spacecraft hazard is expressed by Eq. (67):

$$P_{HZ} = 1 - e^{-EP_{K|H}} \tag{67}$$

The total probability of hazard during a simulation with a start time of t_0 and an end time of t_f is given by Eq. (68):

$$(P_{HZ})_t = \int_{t_0}^{t_f} P_{HZ}(t)\, dt \tag{68}$$

3.10.3 Vulnerability Models

Two differing methods were used to determine $P_{K|H}$ throughout this research. The first consists of a logistic model that depends on the properties of the debris in the vicinity of the spacecraft, particularly debris mass. The initial rationale for excluding particle velocity in the model was that particle mass was assumed to have a stronger relationship with collision damage [3]. The equation for the mass-dependent $P_{K|H}$ is shown in Eq. 69:

$$P_{K|H} = A + \frac{K - A}{(C + Qe^{-B*m})^{1/v}} \tag{69}$$

where $A = 0$, $B = 3$, $C = 1$, $K = 1$, $Q = 0.1$, and $v = 0.05$. Plotting this equation vs. mass obtains Fig. 15:

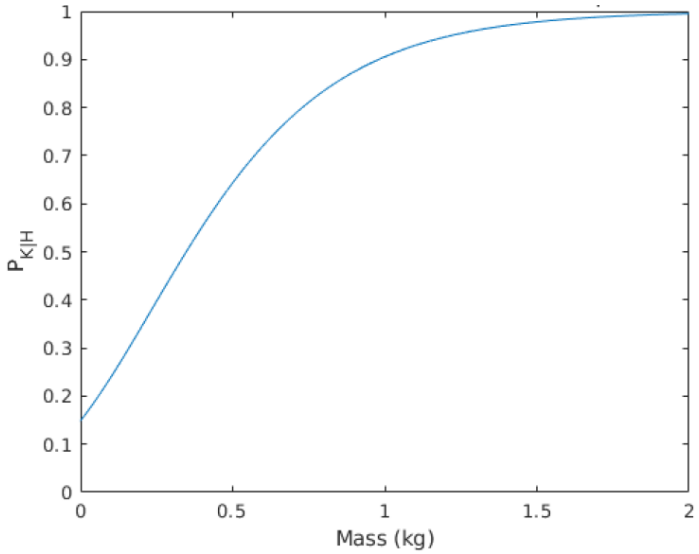

Figure 15: Mass-Dependent Logistic Curve Model [3]

As shown in Fig. 15, $P_{K|H}$ was assumed to trend towards 100% as a particles mass approached 2 kg, the upper limit of particle masses in this model.

The second method to solve for $P_{K|H}$ improves on the first model by using a more realistic $P_{K|H}$ model that incorporates both particle mass and velocity. This $P_{K|H}$ model utilizes ballistic limit equations, which define the impact conditions that will consistently cause failure of a spacecraft shield [61]. To generate a model for $P_{K|H}$, the following Whipple shield performance equation from Christiansen [62] is used:

$$d_c = k_l\left[t_w\left(\frac{\sigma}{40}\right)^{0.5} + C_L t_b \rho_b\right]\left[\cos(\theta)\right]^{-11/16}\rho_p^{-0.5}V^{-2/3} \tag{70}$$

The parameters in this equation and their assumed values are given in Table 12. The assumed shield parameters represent an aluminum Whipple shield consisting of a front bumper at a standoff distance from a rear wall, as described by Christiansen [61]. The projectiles are assumed to represent aluminum debris particles, so the diameter of the debris particles d_p can be calculated from the mass.

Table 12: Parameters in Ballistic Limit Equation

Parameter Symbol	**Meaning**	**Assumed Value**
d_c	Critical projectile diameter causing shield failure (cm)	Calculated through Eq. 70
d_p	Actual projectile diameter (cm)	Calculated from average mass of particles in danger zone
θ	Impact angle measured relative to surface normal	Random variable, limited to $0 \leq \theta \leq 65°$
V	Projectile speed (km/s)	Average speed of particles in danger zone relative to spacecraft
ρ_p	Density of projectile (g/cm^3)	2.70
t_w	Shield rear wall thickness (cm)	0.32
t_b	Shield bumper thickness (cm)	0.127
ρ_b	Shield bumper density (g/cm^3)	2.70
σ	Shield rear wall yield stress (ksi)	57
k_l	Empirical constant	1.9
C_L	Empirical constant (cm^3/g)	0.37

Failure of the shield occurs when the diameter of the projectile that strikes the shield exceeds the critical diameter for the impact, i.e., $d_p > d_c$. The critical diameter depends on the projectile velocity and the impact angle, and the projectile diameter depends on the projectile's mass. The average velocity and mass of particles within the danger zone is used to calculate d_c and d_p, and the impact angle is represented using a random variable.

For a cubic spacecraft, the distribution of observed impact angles is likely to be non-uniform. Normal impacts are more likely than glancing impacts due to the larger area available to hit for normal impacts. The probability of striking a given face (and thus having a certain impact angle) may be calculated using the ratio of the presented size of that face when compared to all other faces available to hit. Calculating impact angle probabilities for a two-dimensional case where particles approach a square spacecraft at all angles uniformly between 0 and 360° and then conducting a Monte Carlo simulation leads to the distribution of impact angles shown in Fig. 16. This distribution of impact angles is used as the distribution for the impact angle random variable θ in the ballistic limit equation. Note that impact angles above 65° are set equal to 65° in the ballistic limit equation due to an increase in shield damage for highly oblique impacts, as recommended by Christiansen [61, 62].

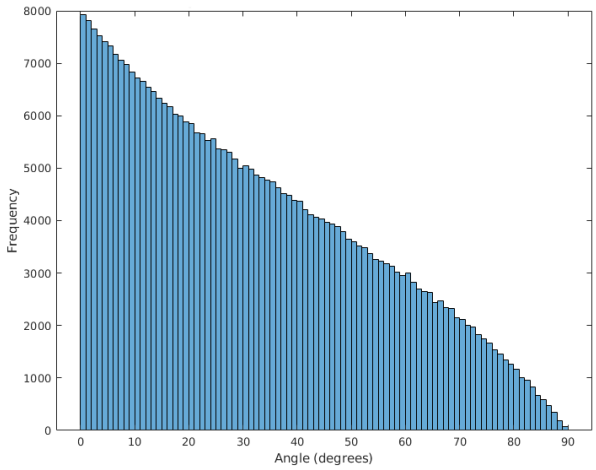

Figure 16: Histogram Showing Distribution of Impact Angles in Monte Carlo Simulation

The probability of shield failure is calculated using the fraction of impact angles that caused failure of the shield for a given projectile mass and velocity according to the ballistic limit equation in Eq. 70. The average masses and velocities of particles in the danger zone are used as the projectile mass and velocity, respectively. A failure of the shield does not necessarily mean the spacecraft will suffer critical damage, so $P_{K|H}$ is calculated by multiplying the probability of shield failure by 50%.

The variation in the resulting $P_{K|H}$ model with particle mass and velocity is shown in Fig. 17. Note that $P_{K|H}$ does not exceed 50%. The jumps in the $P_{K|H}$ curves are a result of the impact angle restriction used by Christiansen [61, 62]. When oblique impacts at angles greater than 65° become capable of penetrating the spacecraft shield, all remaining impact angles between 65° and 90° will also penetrate the shield, so the $P_{K|H}$ curve jumps up to its maximum value of 50%. The shapes of the curves are quite similar to the mass-dependent logistic curve model from Fig. 15.

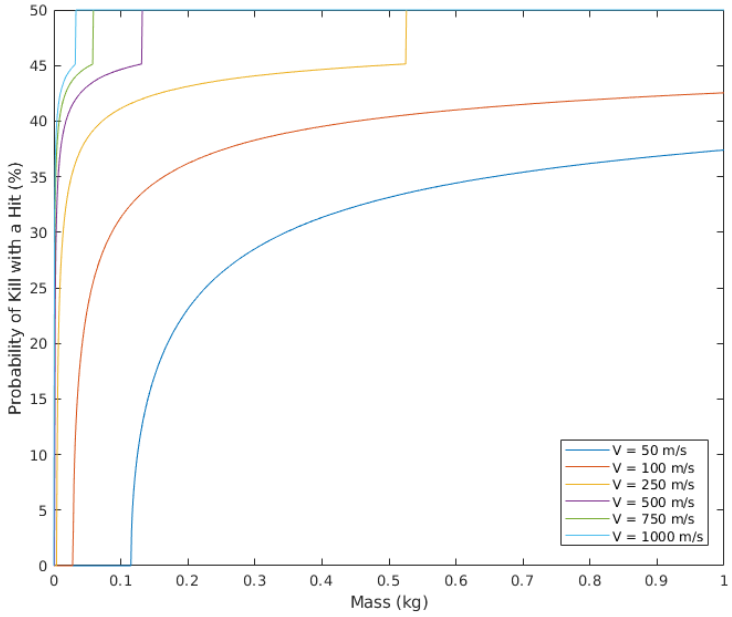

Figure 17: Variation in Ballistic Limit Vulnerability Model with Debris Particle Mass and Velocity

3.11 Summary

This chapter derived the dynamical models used to describe the motion of a spacecraft in the Earth-Moon system. Specifically, Eqs. (18), (29), and (43) were used to model the CR3BP, ER3BP, and BCR4BP, respectively. Differential correction techniques were presented in the form of the single and multiple shooting methods. These techniques are used in adjusting periodic orbits for a standardized μ value as well as approximating error when transitioning between dynamical models. The methodology behind periodic orbit construction and how the halo orbits in this study were derived was explained. Analytical techniques for determining if an object in cislunar space is visible was explained. Finally, the models used in the debris analysis were detailed.

IV. Mission Simulations and Dynamical Variations

4.1 Chapter Overview

Earth-Moon periodic orbits are analyzed, both individually and in constellations with one another, for timely identification and tracking of notional satellites in Lyapunov and halo orbits about the L_1 and L_2 Lagrange points. The orbits analyzed are created and modeled in the Circular Restricted Three-Body Problem (CR3BP). In performing the SDA simulations, Systems Tool Kit (STK) was utilized to model the sensors and dynamics [63]. Data was extracted from the simulation and plotted for analysis. SDA effectiveness is determined as a function of SDA coverage, orbital period (i.e., revisit time), and propellant costs for all cislunar periodic orbits. Notional space-to-space sensors are used to determine limitations of periodic orbit geometry for the SDA missions as a function of capability, range, and Sun/Earth/Moon exclusion angles. Visual magnitude (see Section 3.9) is used in determining if a target satellite is visible.

Once SDA simulations are complete, the cislunar periodic orbits are subject to the ER3BP and BCR4BP dynamics as to ascertain the changes in trajectory under different dynamical assumptions. The implementation of multiple dynamical models is sought in order to compare orbit maintenance costs when transitioning to higher fidelity models. Through means of differential correction, it is shown how much error, in terms of ΔV, the BCR4BP dynamics introduce on the CR3BP solutions for a given number of patchpoints.

The methodology of this research under different conditions was presented at the 2021 Advanced Maui Optical and Space Surveillance Technologies Conference (AMOS), as well as the 2021 AIAA ASCEND conference [64, 65].

4.2 Cislunar Periodic Orbits Analyzed

This research consisted of analyzing 12 cislunar periodic orbits for their effectiveness of Lyapunov and halo orbit monitoring. These orbits are shown in the Earth-Moon system in Figs. 18 and 19 below:

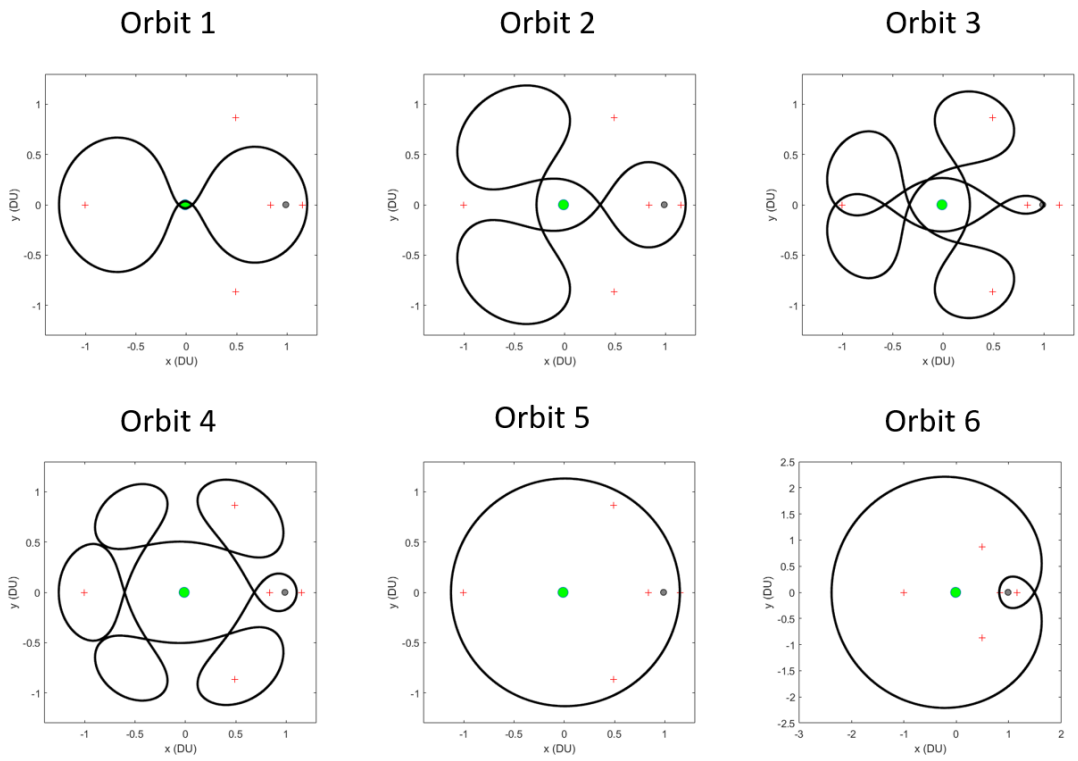

Figure 18: Cislunar Periodic Orbits 1-6

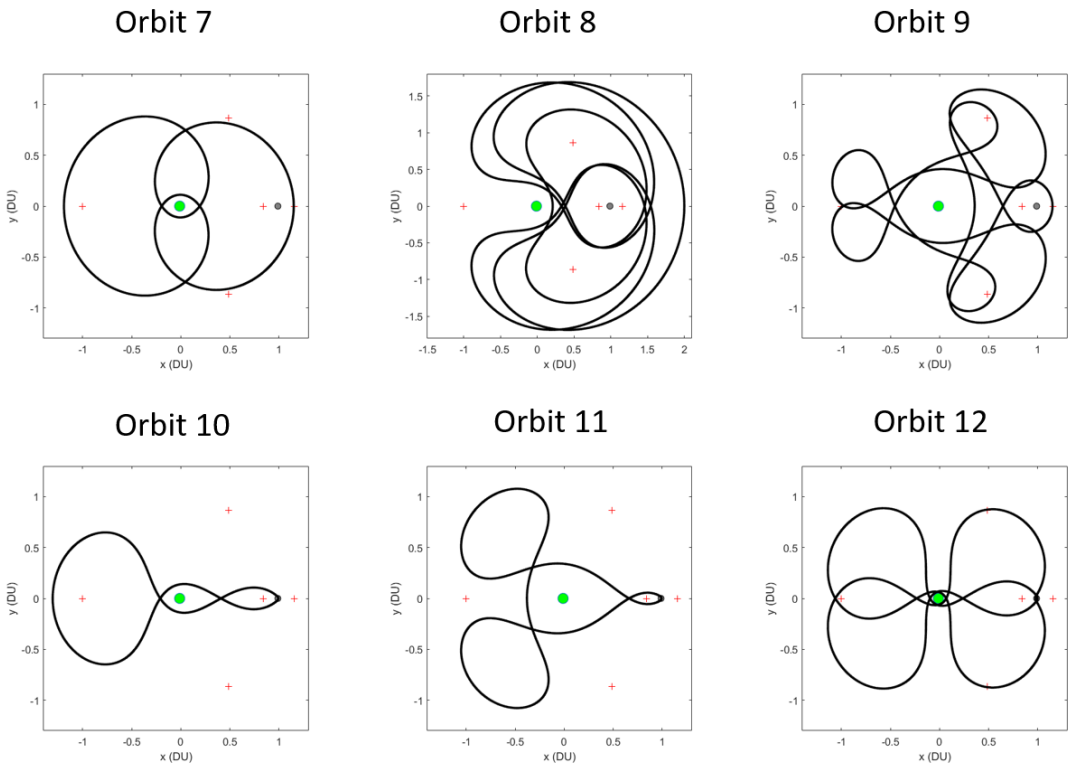

Figure 19: Cislunar Periodic Orbits 7-12

Orbits 1-9 were generated or "discovered" using methods presented in Section 3.7 while Orbits 10-12 were obtained through the works of Arenstorf [25, 26].

4.2.1 Discovered Cislunar Periodic Orbits Initial Conditions

Throughout this research, various cislunar periodic orbits were discovered using the methods presented in Section 3.7. From the discovered cislunar periodic orbits, 9 were chosen (Orbits 1-9 in Figs. 18 and 19) and analyzed for their effectiveness of Lyapunov and halo orbit monitoring. Their initial conditions and approximate periods are presented in Table 13 below:

Table 13: Generated Cislunar Periodic Orbit Initial Conditions in Analysis

Orbit	x_0	$\dot{y}_0$	T_0
1	1.2	-1.05	6.193
2	1.2	-0.768486	12.206
3	1.0	-1.497625	17.785
4	1.105	-0.570184254	29.99
5	1.15	-2.1116	3.42
6	0.82	0.6558356	11.45
7	1.15	-1.585	6.335
8	2.0	-1.624	30.936
9	1.15	-0.5724	30.819

These initial conditions correspond to a non-dimensional mass parameter of $\mu = 0.012150584673414$. It is important to note that the initial conditions for these orbits take the state $\mathbf{X} = \begin{bmatrix} x_0 & 0 & 0 & 0 & \dot{y}_0 & 0 \end{bmatrix}$.

4.2.2 Corrected Cislunar Periodic Orbits Initial Conditions

Cislunar periodic orbits which have been presented in previous literature were also analyzed in this work. Specifically, Orbits 10-12 were found in works from Arenstorf [25, 26]. It is important to note that in the original works in which these orbits were presented, a non-dimensional mass parameter of $\mu = 0.012277471$, which was commonly used in the 1960s by Arenstorf and his contemporaries such as Davidson [66]. The original initial conditions (corresponding to the original μ value used) are given in Table 14:

Table 14: Cislunar Periodic Orbits (From Previous Literature) Initial Conditions Used in Analysis

Orbit	x_0	z_0	$\dot{y}_0$	T_0
10	0.994	0	-2.113898796694	5.4368
11	0.994	0	-2.031732629557	11.1243
12	0.9765	0	-1.690574108489	12.3287

The values in Table 14 were corrected for a modern μ value ($\mu = 0.012150584673414$) using differential correction with 21 patchpoints combined with trial and error of changing the initial y-velocity to ensure periodicity for at least two periods on each orbit of the periodic orbits. The corrected initial conditions for each cislunar periodic orbit in the CR3BP are shown in Table 15:

Table 15: Corrected Cislunar Periodic Orbit Initial Conditions in CR3BP

Parameter	Orbit 10	Orbit 11	Orbit 12
x_0	0.993999897750721	0.994000000062232	0.976500014687630
y_0	-3.7306354$\times 10^{-8}$	-2.123829160152473 $\times 10^{-9}$	0
z_0	0	-1.936516349916483 $\times 10^{-9}$	-1.6769213 $\times 10^{-8}$
$\dot{x}_0$	0.003741232665221	0.001967678410973	0.008008641313757
$\dot{y}_0$	-2.122884103965	-2.0413426475	-1.6768357651
$\dot{z}_0$	0	-1.169055050872915 $\times 10^{-6}$	0
T_0	5.4368	11.1243	12.3287

The periodic orbit initial conditions shown in Table 15 are corrected to allow at least two full repeating periods where no propellant would be required in the CR3BP.

4.3 Target Lyapunov and Halo Orbits Initial Conditions

For this analysis the orbits which were having surveillance conducted on them included Lyapunov and halo orbits about the L_1 and L_2 Lagrange points. The lyapunov

orbits used were orbit 1 from Tables 8 (L_1 orbiting) and 9 (L_2 orbiting) while the halo orbits used were halo orbit 6 from Tables 8 (L_1 orbiting) and 9 (L_2 orbiting). The initial conditions for these orbits are shown in Tables 16 and 17 with more significant figures presented:

Table 16: Target Lyapunov Orbits Initial Conditions Used in Analysis

Parameter	Lyapunov Orbit	
	L_1	L_2
x_0	0.8234	1.180898552288355
y_0	0	0
z_0	0	0
$\dot{x}_0$	0	0
$\dot{y}_0$	0.126231741541912	-0.155856223405548
$\dot{z}_0$	0	0
T_0	2.742912136313352	3.415530868817168

Table 17: Target Halo Orbits Initial Conditions Used in Analysis

Parameter	Halo Orbit	
	L_1	L_2
x_0	0.830969944755594	1.178242316313596
y_0	0	0
z_0	0.12	0.05
$\dot{x}_0$	0	0
$\dot{y}_0$	0.234855901450957	-0.168829207277012
$\dot{z}_0$	0	0
T_0	2.785808231211621	3.394850343537553

Note that the orbits presented in Tables 16 and 17 were created in the CR3BP with a non-dimensional mass parameter of $\mu = 0.012150584673414$.

4.4 Simulations

In this analysis STK's Astrogator system was used to perform all simulations. While all orbits were propagated in a Earth-Moon CR3BP model within STK, Sun exclusion angles were also considered with the Sun located by a realistic ephemeris model which is built into STK. All four scenarios were simulated for two different scenario start conditions as to obtain data for different Sun angles. The two starting dates were 28 Mar 2021 and 29 Oct 2021. The vector range data during the simulations was obtained in 15 minute intervals.

An efficient way of comparing the effectiveness of each cislunar periodic orbit is to reduce as many differences between the scenarios as possible. In reducing free variables between scenarios, the same number of sensor satellites and Targets were chosen for each periodic orbit scenario. For each scenario, 2 Targets were chosen to be traversing the halo orbit trajectory with twelve sensor bearing satellites orbiting the periodic orbit. Each scenario was propagated for approximately 30 days (6.7375 TU). The Lyapunov and halo orbits begin to noticeably diverge from their periodic trajectory after this time, therefore 30 days was chosen to allow for periodicity throughout the scenario. Both the sensor satellites and Targets were spaced out evenly in time in their respective orbit such that at the beginning of the scenario there was always one satellite in the orbits initial conditions. A Target is assumed to be viewable if at least one of the twelve sensor bearing satellites is able to view it based on visual magnitude.

4.4.1 Single Cislunar Periodic Orbit Simulations

The first stage of this analysis is to analyze all twelve cislunar periodic orbits separately for their effectiveness at monitoring the Targets in all four example scenarios. Each scenario was given it's own table such that monitoring Targets in L_1

Lyapunov, L_2 Lyapunov, L_1 halo, and L_2 halo orbits correspond to Tables 18, 19, 20, and 21 respectively. The results include the percentage of time the Targets in the Lyapunov/halo orbit were visible based on visual magnitude. In all resulting tables the top three orbits which had the highest performance (most time on average observing the Targets) are highlighted green. To assist with visualizing the scenarios, simulations in STK for cislunar periodic orbits 1, 6, and 9 (descending order) for both the L_1 and L_2 Lyapunov orbit scenarios are shown below in Fig. 20:

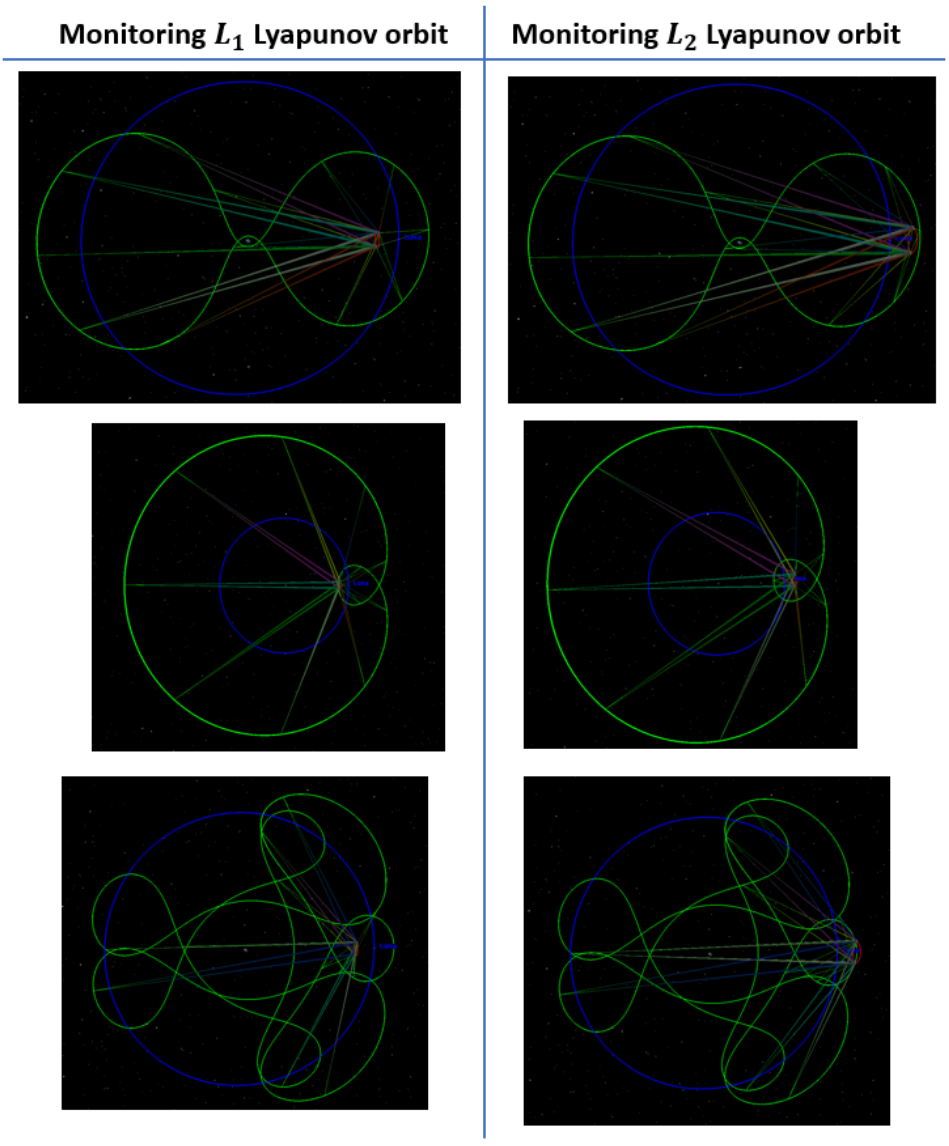

Figure 20: SDA Single Orbit Simulation Visuals for Select Orbits

As shown in Fig. 20 the blue orbit depicts the Moon's orbit about the Earth, the green orbit depicts the cislunar periodic orbit, and the red orbit depicts the Target's orbit. The sensors on each friendly satellite are also shown pointing at the Targets. These depict 6 of the total 48 scenarios (4 scenarios for each cislunar periodic orbit) played out. The results of the single cislunar periodic orbit SDA scenarios are presented in Tables 18-21:

Table 18: L_1 Lyapunov Orbit Targets Surveillance Results (% Time Visible)

Start Date:	28 Mar 2021		29 Oct 2021		
Orbit	Target 1	Target 2	Target 1	Target 2	**Average**
1	96.39%	97.12%	97.43%	99.76%	**97.68%**
2	96.81%	95.80%	93.34%	96.56%	**95.63%**
3	93.06%	91.46%	95.32%	96.63%	**94.12%**
4	93.34%	90.56%	100.00%	90.80%	**93.68%**
5	93.58%	92.99%	94.10%	95.21%	**93.97%**
6	95.70%	100.00%	100.00%	96.36%	**98.02%**
7	94.38%	92.40%	92.26%	97.85%	**94.22%**
8	94.10%	94.69%	94.31%	93.37%	**94.12%**
9	94.90%	100.00%	99.86%	97.71%	**98.12%**
10	81.99%	86.85%	91.12%	91.64%	**87.90%**
11	75.05%	62.63%	72.24%	70.40%	**70.08%**
12	97.05%	98.30%	99.41%	99.41%	**98.54%**

Table 19: L_2 Lyapunov Orbit Targets Surveillance Results (% Time Visible)

Start Date:	28 Mar 2021		29 Oct 2021		
Orbit	Target 1	Target 2	Target 1	Target 2	**Average**
1	100.00%	100.00%	100.00%	97.02%	**99.26%**
2	98.23%	92.05%	89.38%	93.72%	**93.35%**
3	90.84%	97.85%	85.22%	94.52%	**92.11%**
4	96.15%	93.48%	93.58%	94.86%	**94.52%**
5	93.89%	90.42%	98.13%	90.63%	**93.27%**
6	99.20%	100.00%	96.53%	100.00%	**98.93%**
7	96.60%	94.52%	97.22%	91.85%	**95.05%**
8	90.98%	92.47%	83.87%	91.98%	**89.83%**
9	100.00%	98.06%	100.00%	97.71%	**98.94%**
10	81.30%	77.76%	79.74%	70.82%	**77.41%**
11	64.19%	53.78%	62.77%	64.82%	**61.39%**
12	100.00%	97.19%	100.00%	98.44%	**98.91%**

Table 20: L_1 Halo Orbit Targets Surveillance Results (% Time Visible)

Start Date:	28 Mar 2021		29 Oct 2021		
Orbit	Target 1	Target 2	Target 1	Target 2	**Average**
1	99.83%	99.79%	99.72%	98.99%	**99.58%**
2	96.84%	97.22%	100.00%	97.54%	**97.90%**
3	100.00%	100.00%	98.13%	99.17%	**99.33%**
4	99.20%	98.82%	100.00%	100.00%	**99.51%**
5	96.25%	96.43%	96.22%	96.39%	**96.32%**
6	100.00%	100.00%	96.77%	100.00%	**99.19%**
7	97.88%	98.23%	99.34%	99.24%	**98.67%**
8	100.00%	96.70%	93.93%	97.81%	**97.11%**
9	94.24%	100.00%	100.00%	100.00%	**98.56%**
10	100.00%	100.00%	100.00%	100.00%	**100.00%**
11	97.50%	92.26%	93.20%	97.26%	**95.06%**
12	100.00%	100.00%	100.00%	100.00%	**100.00%**

Table 21: L_2 Halo Orbit Targets Surveillance Results (% Time Visible)

Start Date:	28 Mar 2021		29 Oct 2021		
Orbit	Target 1	Target 2	Target 1	Target 2	**Average**
1	100.00%	100.00%	100.00%	97.54%	**99.39%**
2	97.54%	92.82%	93.51%	94.38%	**94.56%**
3	91.22%	99.90%	84.91%	94.41%	**92.61%**
4	96.70%	94.03%	93.23%	95.35%	**94.83%**
5	95.04%	92.16%	98.82%	91.29%	**94.33%**
6	99.27%	100.00%	97.54%	100.00%	**99.20%**
7	96.56%	95.04%	99.55%	93.41%	**96.14%**
8	91.88%	95.35%	83.07%	93.44%	**90.94%**
9	100.00%	98.47%	100.00%	98.79%	**99.32%**
10	82.93%	79.70%	85.77%	70.99%	**79.85%**
11	75.36%	64.78%	75.92%	61.21%	**69.32%**
12	100.00%	97.95%	100.00%	98.58%	**99.13%**

The cislunar periodic orbits analyzed overall performed exceptionally well in monitoring L_1/L_2 Lyapunov and halo orbits. Nearly every scenario saw all twelve orbits have an average Target visibility of 90% or more. In terms of performance across the orbits, with respect to L_1 Lyapunov monitoring, Orbit 12 had the highest average percentage of Target visibility with 98.54%. Orbits 6 and 9 were nearly identical in performance to Orbit 12, hosting a 98.12% and 98.02% Target visibility respectively.

With regards to monitoring the L_1 halo orbit, Orbit 10 and 12 were shown to be the most effective with both displaying a 100% average visibility of the Target over the 30 day simulation. This is attributed to both orbits featuring close proximity L_1 passes which place the satellites in these orbits extremely close to the Targets. It is reasonable that these orbits performed similar: while Orbit 10 may only have 2 passes of L_1 for one period, its period is one of the shortest analyzed. On the other

hand, Orbit 12 has a little over twice the period as Orbit 10, however, it features more instances with close proximity L_1 passes.

Orbit 1 was shown to be the most effective at monitoring both L_2 Lyapunov and halo orbits. A key feature of Orbit 1 is it's long dwell time on the backside of the Moon. For a twelve satellite constellation and Orbit 1's relatively short period, when compared to other orbits analyzed, there are always 2-3 sensor bearing satellites on the backside of the Moon providing excellent viewing angles of L_2. Orbits 6 and 9 were close seconds in L_2 orbit surveillance, with there being less than a percentage difference in results. This is to be expected since Orbits 6 and 9 both feature a long dwell time about the Moon.

4.4.2 Cislunar Periodic Orbit Constellation Simulations

The four best performing cislunar periodic orbits from the previous section were chosen to create constellations with one another to analyze the effectiveness of monitoring Lyapunov and halo orbits about the L_1 and L_2 Lagrange points. Orbits 1, 6, 9, and 12 were chosen because they did consistently well in 2 or more of the simulations presented in Tables 18-21. As with the single cislunar periodic orbits simulations, in the constellation simulations there are a total of twelve sensor bearing satellites distributed amongst the respective cislunar periodic orbits in each scenario. For instance, if the constellation consists of 2 cislunar periodic orbits (such as 1+6) then each will consist of six sensor bearing satellites. Conversely, if the constellation consists of three cislunar periodic orbits (such as 1+6+9) then each will consist of four sensor bearing satellites. For all orbits, the satellites (whether it be a sensor satellite or Target) were spaced out evenly in time in their respective orbit such that at the beginning of the scenario there was always one spacecraft in the orbits initial conditions. To assist with visualizing the scenarios, simulations in STK for cislunar

periodic orbits 1+6 and 1+6+9 for both the L_1 and L_2 Lyapunov orbit scenarios are shown below in Fig. 21:

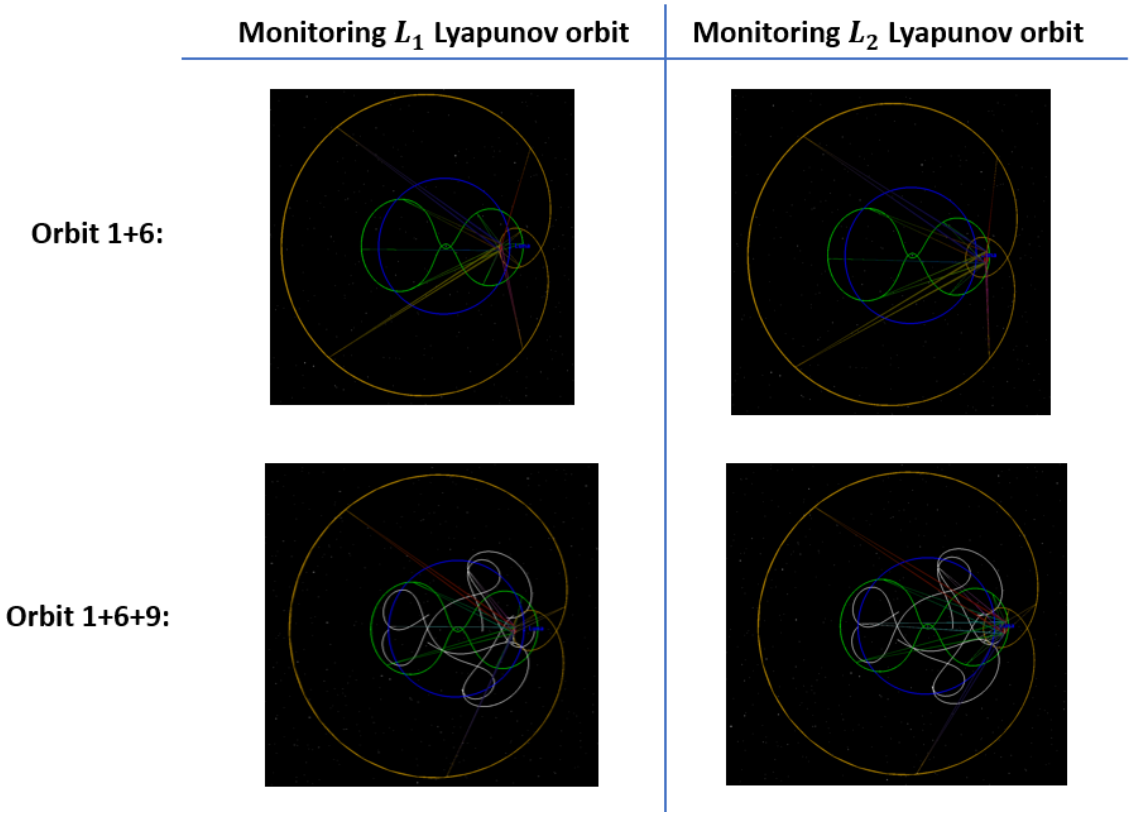

Figure 21: SDA Constellation Orbit Simulation Visuals for Select Orbits

As shown in Fig. 21, when the four satellites are spread out across Orbit 9, there is not enough time in the simulation for the sensor satellites to collectively traverse the entire trajectory. This is due to the long period which Orbit 9 features. The results of the constellation simulations are presented in Tables 22-25 below:

Table 22: L_1 Lyapunov Orbit Targets Surveillance Results (% Time Visible) for Cislunar Periodic Orbit Constellations

Start Date:	28 Mar 2021		29 Oct 2021		
Orbit	Target 1	Target 2	Target 1	Target 2	**Average**
1 + 6	93.48%	94.14%	95.45%	97.02%	**95.02%**
1 + 9	97.74%	96.25%	93.13%	97.54%	**96.17%**
1 + 12	93.82%	92.68%	95.28%	94.24%	**94.01%**
6 + 9	99.79%	99.44%	97.61%	99.44%	**99.07%**
6 + 12	90.22%	91.92%	98.96%	93.48%	**93.65%**
9 + 12	95.49%	100.00%	100.00%	100.00%	**98.87%**
1 + 6 + 9	91.85%	86.22%	91.36%	90.60%	**90.01%**
1 + 6 + 12	75.50%	68.60%	84.04%	77.65%	**76.45%**
1 + 9 + 12	84.14%	84.52%	90.49%	90.70%	**87.46%**
6 + 9 + 12	90.32%	94.07%	90.32%	94.07%	**92.20%**

Table 23: L_2 Lyapunov Orbit Targets Surveillance Results (% Time Visible) for Cislunar Periodic Orbit Constellations

Start Date:	28 Mar 2021		29 Oct 2021		
Orbit	Target 1	Target 2	Target 1	Target 2	**Average**
1 + 6	98.37%	98.30%	99.51%	96.60%	**98.20%**
1 + 9	99.13%	99.83%	90.28%	96.98%	**96.56%**
1 + 12	87.51%	91.74%	90.15%	96.11%	**91.38%**
6 + 9	97.88%	100.00%	93.55%	91.29%	**95.68%**
6 + 12	92.92%	93.72%	91.29%	93.37%	**92.83%**
9 + 12	100.00%	100.00%	100.00%	100.00%	**100.00%**
1 + 6 + 9	95.98%	96.81%	94.80%	97.71%	**96.33%**
1 + 6 + 12	91.26%	96.46%	94.27%	96.81%	**94.7%**
1 + 9 + 12	90.60%	96.77%	92.26%	95.80%	**93.86%**
6 + 9 + 12	95.45%	93.03%	86.05%	95.91%	**92.61%**

Table 24: L_1 Halo Orbit Targets Surveillance Results (% Time Visible) for Cislunar Periodic Orbit Constellations

Start Date:	28 Mar 2021		29 Oct 2021		
Orbit	Target 1	Target 2	Target 1	Target 2	**Average**
1 + 6	96.77%	100.00%	96.29%	100.00%	**98.27%**
1 + 9	96.60%	99.62%	96.32%	99.83%	**98.09%**
1 + 12	99.83%	96.46%	98.23%	99.10%	**98.41%**
6 + 9	100.00%	100.00%	99.79%	100.00%	**99.95%**
6 + 12	92.82%	99.55%	98.68%	100.00%	**97.76%**
9 + 12	99.51%	100.00%	100.00%	100.00%	**99.88%**
1 + 6 + 9	98.72%	95.21%	97.22%	99.41%	**97.64%**
1 + 6 + 12	95.00%	89.90%	95.59%	98.02%	**94.63%**
1 + 9 + 12	88.69%	95.21%	94.62%	98.72%	**94.31%**
6 + 9 + 12	79.98%	100.00%	79.98%	100.00%	**89.99%**

Table 25: L_2 Halo Orbit Targets Surveillance Results (% Time Visible) for Cislunar Periodic Orbit Constellations

Start Date:	28 Mar 2021		29 Oct 2021		
Orbit	Target 1	Target 2	Target 1	Target 2	**Average**
1 + 6	99.48%	98.82%	99.48%	97.09%	**98.72%**
1 + 9	100.00%	99.55%	93.44%	97.19%	**97.55%**
1 + 12	89.04%	91.98%	91.98%	96.22%	**92.31%**
6 + 9	98.54%	100.00%	95.94%	93.16%	**96.91%**
6 + 12	93.58%	94.52%	91.33%	94.48%	**93.48%**
9 + 12	100.00%	100.00%	100.00%	100.00%	**100.00%**
1 + 6 + 9	96.88%	97.71%	97.68%	98.65%	**97.73%**
1 + 6 + 12	93.30%	97.71%	95.87%	98.09%	**96.24%**
1 + 9 + 12	90.84%	97.71%	95.94%	96.70%	**95.30%**
6 + 9 + 12	94.80%	90.87%	85.11%	95.25%	**91.51%**

When put in two-orbit constellations with one another, there appears to be slight improvement in Target visibility time for all scenarios except the L_1 halo orbit case. However, when put in three-orbit constellations with one another, there is a slight decrease in performance. These results, particularly the improvements in target observation from two-orbit constellations, differ from those presented in previous research [65]. This is likely due to the larger body of cislunar periodic orbits analyzed in this research.

For monitoring both the L_1 Lyapunov and halo orbits, cislunar periodic orbit combination 6+9 proved to have the best performance, showcasing a 99.07% average visibility of the L_1 Lyapunov Targets and a 99.95% average visibility of the L_1 halo Targets. Orbit geometry is the key factor in these results. Orbit 6 features a loop about the Moon which nearly intersects L_1. With six sensor satellites spread out across the orbit, there will always be one or two that are near this critical node. Similarly, there is a significant portion of Orbit 9 which is between the Earth and Moon and fully encapsulate L_1. These factors provide many opportunities for varying viewing angles between Orbits 6 and 9 while also providing minimal interference due to exclusion angles.

For monitoring both the L_2 Lyapunov and halo orbits, cislunar periodic orbit combination 9+12 proved to have the best performance, showcasing a 100% average visibility of the Targets. These results are attributed to orbit geometry for both Orbits 9 and 12. The large loops which are located on the L_2 side of the Moon provide for a high probability of viewing the Targets with no risk of issues caused by Earth exclusion angles and minimal risk of issues from lunar exclusion angles.

4.5 Variations in Trajectory in Higher Fidelity Models

A particularly interesting study is the dynamical evolution from the CR3BP to higher fidelity models, such as the ER3BP and BCR4BP. While Orbits 1-12 are periodic in the CR3BP, they rapidly become unstable with the introduction of more perturbations, such as the Moon's eccentricity or the Sun's gravitational force. In this section, cislunar periodic orbits are propagated using the ER3BP and BCR4BP. The dynamical variations in these periodic orbits when transitioning between dynamical models are analyzed and discussed with plots presented.

All cislunar periodic orbits were propagated in the ER3BP with an eccentricity value of $e = 0.0549$ used for the Moon's orbit. In terms of BCR4BP propagation, the Sun was assumed to be initially aligned with the Earth and Moon at an angle of zero degrees. The constants used in the BCR4BP propagation are shown in Table 4.

Propagating each periodic orbit for one period resulted in Figs. 22-33 corresponding to cislunar periodic orbits 1-12. For all figures, the left image is the original CR3BP propagation, the middle image is the ER3BP propagation, and the right image is the BCR4BP propagation.

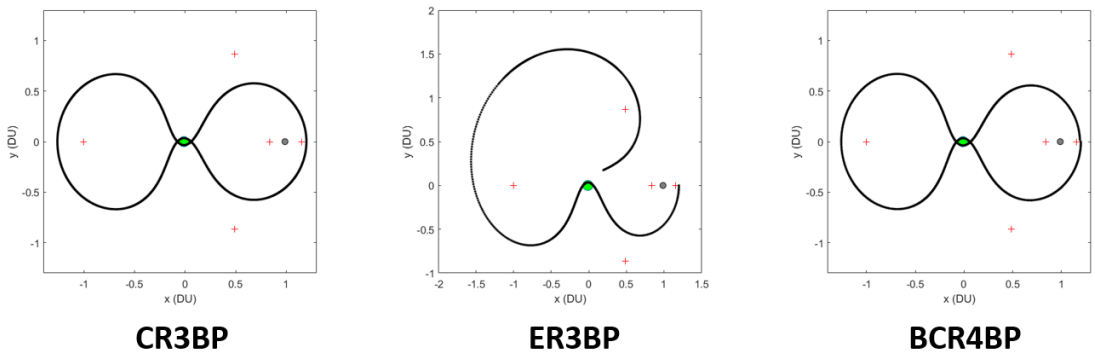

Figure 22: Propagation of Cislunar Periodic Orbit 1 via all Dynamical Models

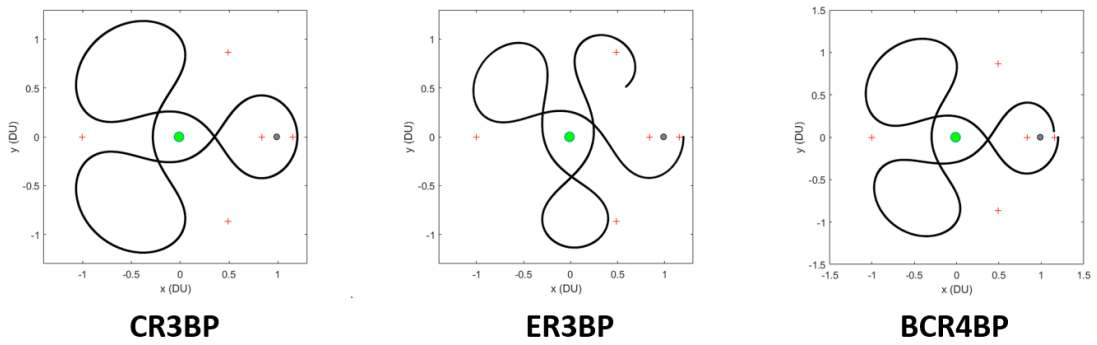

Figure 23: Propagation of Cislunar Periodic Orbit 2 via all Dynamical Models

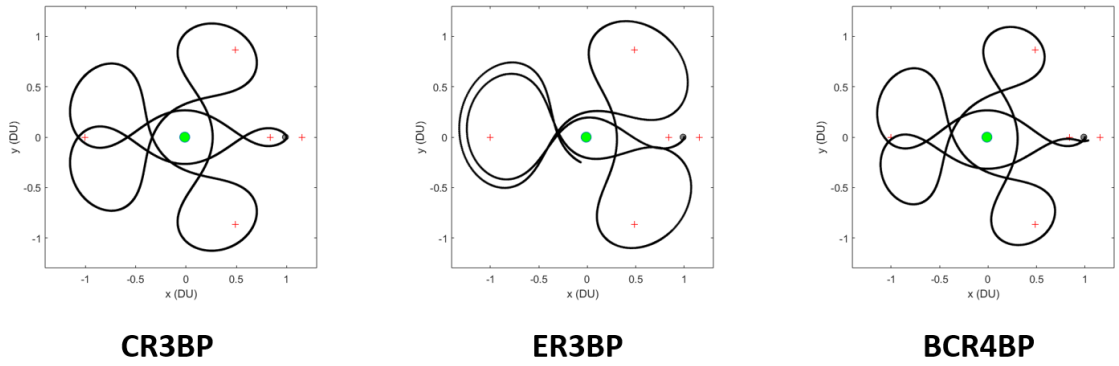

Figure 24: Propagation of Cislunar Periodic Orbit 3 via all Dynamical Models

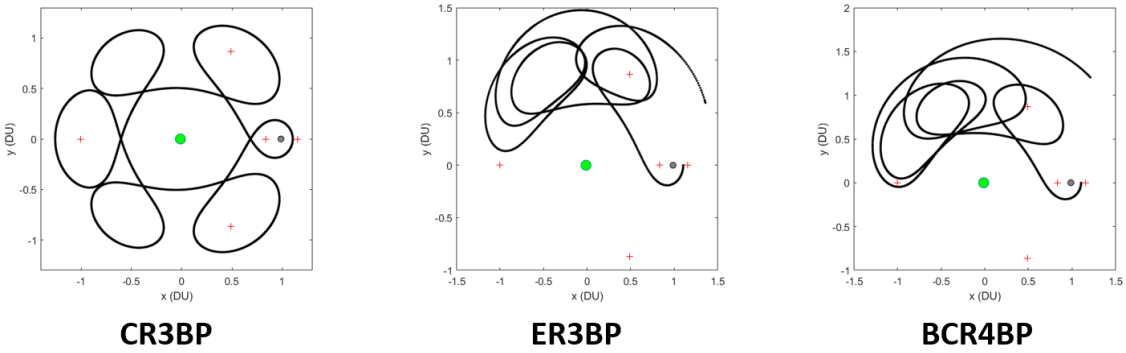

Figure 25: Propagation of Cislunar Periodic Orbit 4 via all Dynamical Models

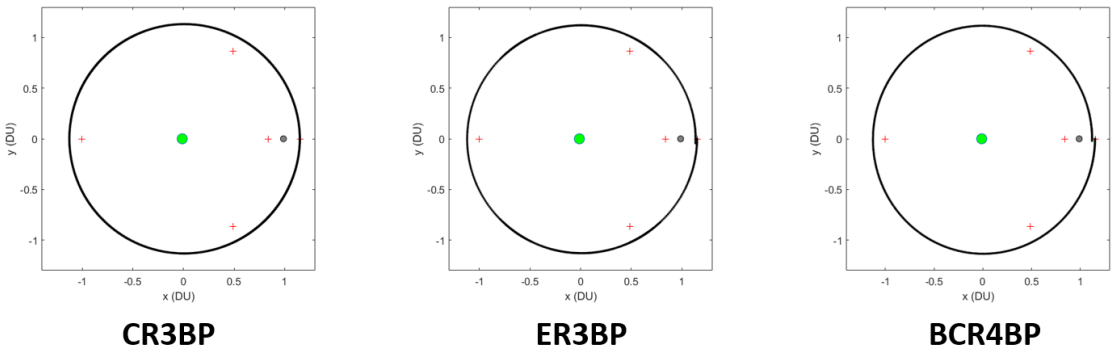

Figure 26: Propagation of Cislunar Periodic Orbit 5 via all Dynamical Models

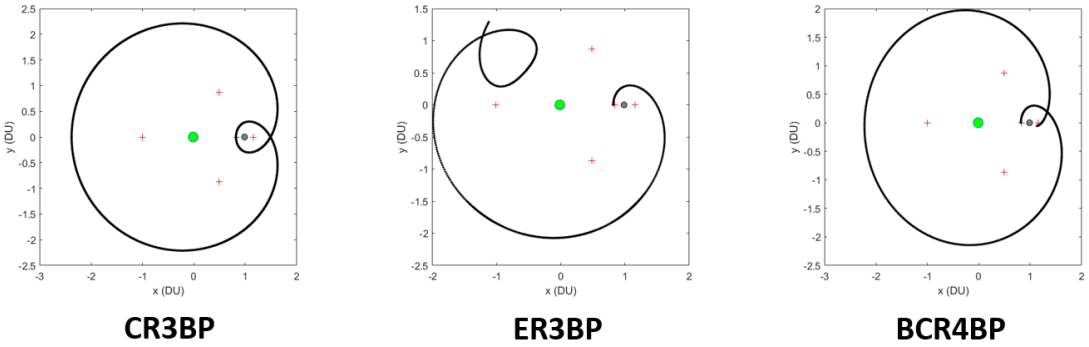

Figure 27: Propagation of Cislunar Periodic Orbit 6 via all Dynamical Models

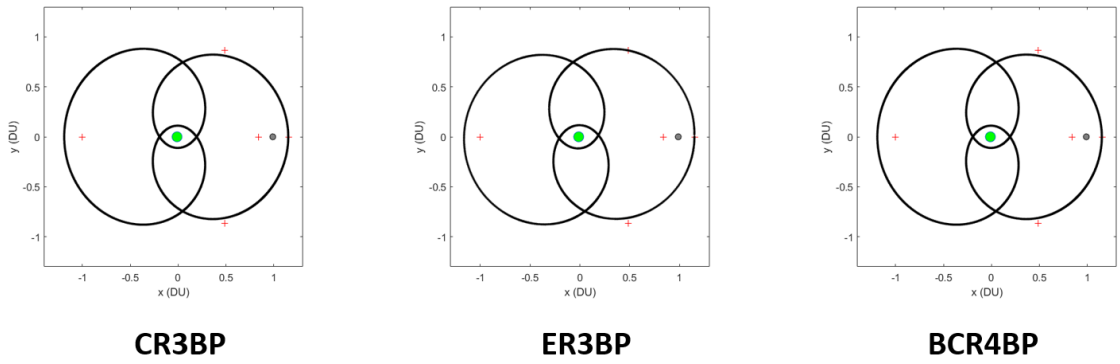

Figure 28: Propagation of Cislunar Periodic Orbit 7 via all Dynamical Models

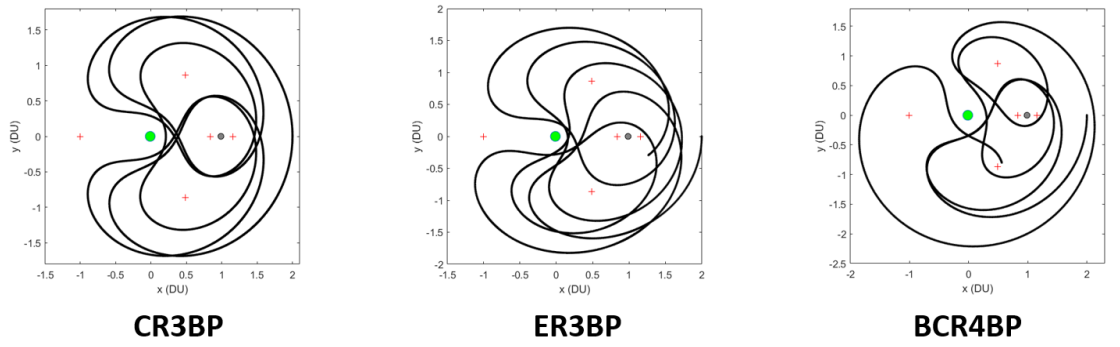

Figure 29: Propagation of Cislunar Periodic Orbit 8 via all Dynamical Models

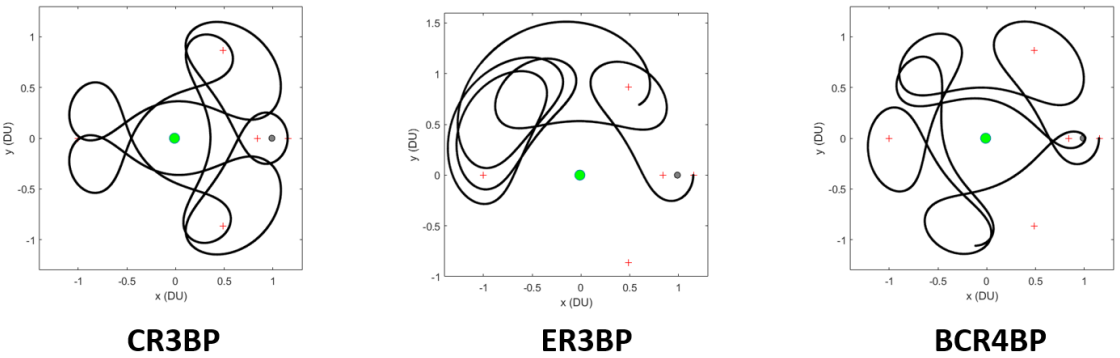

Figure 30: Propagation of Cislunar Periodic Orbit 9 via all Dynamical Models

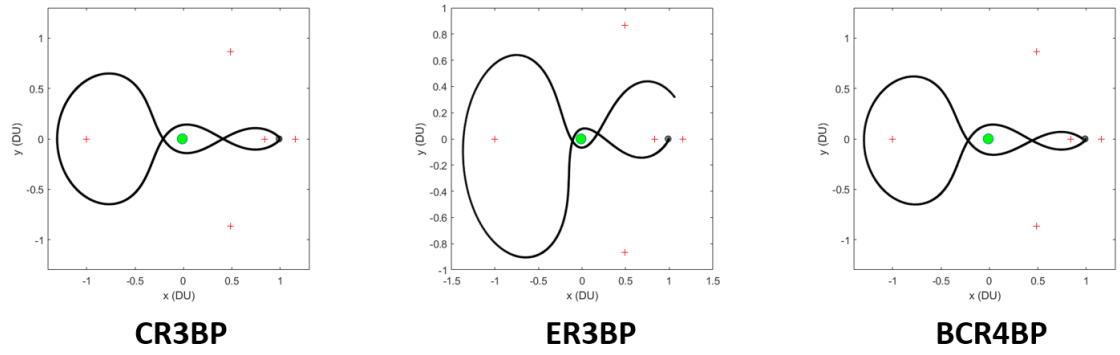

Figure 31: Propagation of Cislunar Periodic Orbit 10 via all Dynamical Models

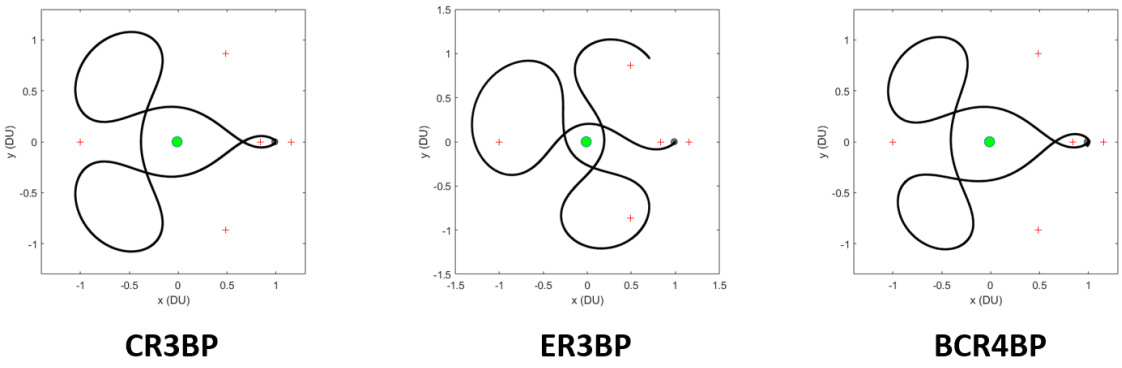

Figure 32: Propagation of Cislunar Periodic Orbit 11 via all Dynamical Models

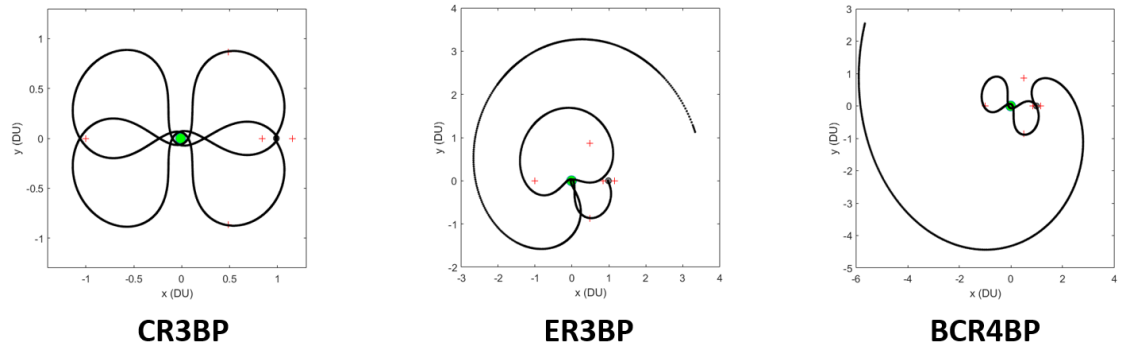

Figure 33: Propagation of Cislunar Periodic Orbit 12 via all Dynamical Models

It was observed that for the majority of these orbits, propagations in the ER3BP had significantly higher perturbative effects than the BCR4BP. This is expected due to the proximity of the Moon compared to the Sun. Since the Sun is approximately 389 times further away from the synodic reference frame origin than the Moon, the addition of solar gravitational influences is dwarfed when compared to any changes in the motion of the Moon while the satellite is in the Earth-Moon sphere of influence. If the periodic trajectory would traverse translunar[1] space, the effects of solar influences would begin to become more significant and surpass the effects of the Moon's eccentricity.

[1]The term "translunar" refers to the volume of space beyond the Moon and its orbit.

Initial conditions which produce stable one-period periodic orbits in the CR3BP produce noticeably unstable trajectories in the higher fidelity models if left uncorrected. To combat perturbations which force cislunar periodic orbits in the CR3BP to become non-periodic in higher fidelity models, stabilizing controllers are used. The most obvious form of a stabilizing controller is propellant expenditure, commonly refereed to as ΔV. ΔV expenditure paired with altered initial conditions found through differential correction via the single/multiple shooting method may provide the lowest cost solution to stability in higher fidelity models. Nonetheless, it is expected that differential correction will only lower the ΔV required for maintenance as opposed to eliminate the need altogether. Differential correction may be used for another purpose than changing the initial conditions: ΔV required to maintain periodicity in higher fidelity models may be found through differential correction in the single shooting method.

4.6 BCR4BP Correction Analysis

As discussed previously in Section 3.3, a commonly used stabilizing controller to mitigate chaos is the use of propellant to adjust trajectory, more specifically referred to as change in velocity, ΔV. ΔV expenditure is generally the limiting variable and dominant cost in space flight duration and longevity. However, the ΔV required for trajectory adjustments can be significantly reduced if scheduled early enough in the trajectory. While the orbits analyzed in this work are periodic in the CR3BP, potentially requiring no ΔV, these orbits become more chaotic when subject to higher fidelity models such as the BCR4BP. One solution would be to implement a controller to correct back to the CR3BP reference orbit by expending ΔV. However, one could also perform the same corrective methods in the BCR4BP dynamics to again generate periodic, or nearly periodic, solutions. It is shown here how much error the BCR4BP

dynamics introduce on the CR3BP solutions found previously and how correcting in the new dynamics minimizes those errors.

The methodology begins by using the initial conditions found in Tables 13 and 15 to create 21 patchpoints based on the CR3BP solution, then using the single shooting method to update the velocities in the BCR4BP. The amount of velocity correction is calculated as the sum of the individual ΔV's generated by the shooting method at the first patch point and each of the 19 middle patchpoints (a 20 patchpoint sum). The last point is excluded in the addition as it is in the same location as the first patchpoint. The analysis was performed on four different starting angles for the Sun with respect to the synodic reference frame x-axis for each orbit to show that the correction is time dependent. To assist in visualisation, the trajectories between patchpoints for 3 of the 12 orbits (orbits 1, 2, and 3) are shown in Fig. 34. The results of this analysis are presented in Table 26 with the amount of correction or error in ΔV shown as Δe_V in units of meters/second calculated for one period of each orbit.

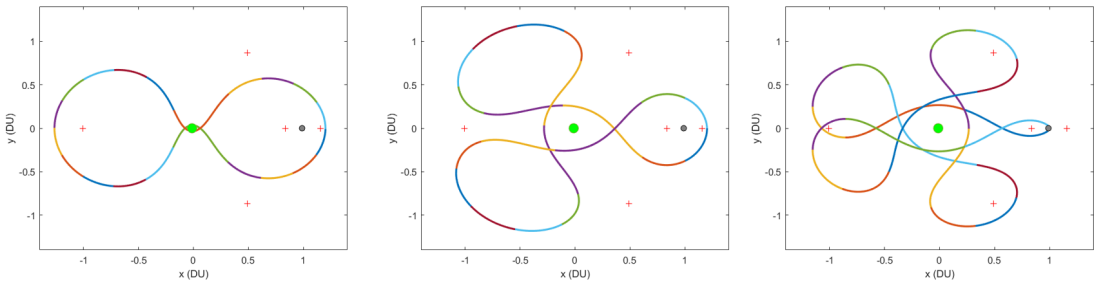

Figure 34: Cislunar Periodic Orbits 1-3 Subject to the Single Shooting Method in BCR4BP

Table 26: Approximate Δe_V Per Period Required to Maintain Orbit with 21 patchpoints in BCR4BP (in m/s)

Initial Sun Position:	0°	90°	180°	270°	**Average**
Orbit 1 Δe_V	2.169	1.090	2.189	1.090	**1.635**
Orbit 2 Δe_V	4.023	2.036	4.060	2.036	**3.039**
Orbit 3 Δe_V	6.439	3.706	6.481	3.707	**5.083**
Orbit 4 Δe_V	6.670	3.541	6.716	3.548	**5.119**
Orbit 5 Δe_V	1.166	0.589	1.176	0.589	**0.880**
Orbit 6 Δe_V	2.491	1.534	2.506	1.534	**2.016**
Orbit 7 Δe_V	2.125	1.076	2.144	1.077	**1.606**
Orbit 8 Δe_V	17.143	8.762	17.408	8.757	**12.993**
Orbit 9 Δe_V	6.755	3.902	6.807	3.899	**5.341**
Orbit 10 Δe_V	2.387	1.204	2.404	1.204	**1.800**
Orbit 11 Δe_V	5.060	2.801	5.095	2.797	**3.938**
Orbit 12 Δe_V	5.243	2.646	5.287	2.643	**3.955**

It is important to note that these Δe_V values change depending on the number of patchpoints chosen. At first glance of Table 26 it appears that Orbit 5 provides the least amount of error when transitioning from the CR3BP to the BCR4BP. However, this is to be expected because it hosts the shortest period. To more accurately compare the difference in error between orbits, it is beneficial to calculate the unit Δe_V, that is, the average Δe_V required per one time unit (4.4527 days). To accomplish this, the averages of Table 26 were divided by their respective orbit's non-dimensional period. The unit Δe_V (in meters/second) for each cislunar periodic orbit in the BCR4BP is shown in Table 27:

Table 27: Approximate Unit Δe_V Required to Maintain Orbit with 21 patchpoints in BCR4BP (in m/s)

	Average
Orbit 1 Unit Δe_V	**0.264**
Orbit 2 Unit Δe_V	**0.249**
Orbit 3 Unit Δe_V	**0.286**
Orbit 4 Unit Δe_V	**0.171**
Orbit 5 Unit Δe_V	**0.257**
Orbit 6 Unit Δe_V	**0.176**
Orbit 7 Unit Δe_V	**0.254**
Orbit 8 Unit Δe_V	**0.420**
Orbit 9 Unit Δe_V	**0.173**
Orbit 10 Unit Δe_V	**0.331**
Orbit 11 Unit Δe_V	**0.354**
Orbit 12 Unit Δe_V	**0.321**

Therefore, based on Table 27, Orbit 4 provides the least amount of error per time unit when transitioning to a higher fidelity model such as the BCR4BP. This is a hint that Orbit 4 will likely also be the most efficient in terms of propellant expenditure required to maintain trajectory in real life. This is to be expected since the majority of Orbit 4's trajectory is far from the Earth in terms of flyby distance which causes a low perturbation effect due to the Earth. Orbit 8 proved to have the most errors when transitioning from the CR3BP to the BCR4BP. This is to be expected since Orbit 8 has a trajectory which frequently passes between the Earth and Moon and features close proximity Earth passes. These results show promise for cislunar periodic orbits requiring low propellant expenditure in practice.

4.7 Summary and Recommendations

The cislunar periodic orbits analyzed in this work are ideal candidates for cislunar SDA mission architectures due to their periodicity and ability to traverse a wide expansion of cislunar space capturing various viewing angles on the Targets. This chapter sought to present and compare of the effectiveness of twelve different cislunar periodic orbits, both individually and when combined with one another, when subject to the SDA mission architecture of monitoring Targets in L_1/L_2 Lyapunov and halo orbits. All periodic orbit initial conditions were generated with a non-dimensional mass parameter of $\mu = 0.012150584673414$. The halo orbit initial conditions were found by taking advantage of the symmetry about the x-z plane, and using a continuation method to form families of potential orbits. These periodic orbits and combination of periodic orbits were then subject to simulations in which the visual magnitude was recorded with Sun, Earth, and Moon exclusion angles also considered.

When comparing the individual cislunar periodic orbits analyzed, Orbit 12 has the highest average L_1 Lyapunov orbit visibility, Orbits 10 and 12 share the highest average L_1 halo orbit visibility, and Orbit 1 has the highest average visibility for both the L_2 Lyapunov and halo orbits. However, when combining these orbits in constellations with one another, the results were slightly different. Orbit constellation 6+9 has the highest average L_1 Lyapunov orbit visibility, orbit constellation 9+12 has the highest average L_2 Lyapunov orbit visibility, Orbits 10 and 12 remain to have the highest average visibility for the L_1 halo orbit, and orbit constellation 9+12 has the highest average L_2 halo orbit visibility. While combining these orbits in constellations, specifically in two orbit constellations, did provide better results, the improvements were generally less than a percentage point. Therefore, for simplicity, it is recommended using single cislunar periodic orbits to conduct SDA for particular Lagrange points with the optimal cislunar periodic orbit depending on the mission.

When applied to reality, there are many more perturbations which the satellites will experience. These added perturbations induce further chaos and disturb the satellites from their periodic trajectories. BCR4BP Δe_V analysis was performed to calculate the approximate ΔV error (Δe_V) when transitioning from the CR3BP to the BCR4BP. Solving for the Δe_V required per time unit in the BCR4BP showed that Orbit 4 had the lowest required propellant expenditure on average. However, Orbits 6 and 9 have only a 0.005 and 0.002 m/s higher unit Δe_V, making them nearly identical in expenditure. Thus, due to the effectiveness in detection ability coupled with low Δe_V when transitioning to the BCR4BP, Orbits 6 and 9 show a high potential of success in being applied to cislunar SDA.

V. Proposed Space Domain Awareness Taxonomy

5.1 Chapter Overview

With the space beyond geosynchronous orbit likely to become competitive and congested in the coming decades, a new way of classifying Space Domain Awareness (SDA) missions which encompass the entire Earth-Moon system is advocated, to include the spatial expanses in the outside vicinity of the Earth's gravitational sphere of influence. Attaining space situational and wider space domain awareness in the future will require a field of view not limited to the traditional bounds of geosynchronous orbit. In this work, a new taxonomy for the classification of SDA regions is presented. This new taxonomy will enable a spatial division of the national SDA mission portfolio, with specific regions corresponding to compounding distances from the Earth and varying SDA mission subsets, to include space traffic management, space control, lunar/Lagrange point surveillance, space weather observation, and planetary defense. This research is in the process of being published in Air and Space Power Journal (ASPJ).

5.2 Current Space Domain Awareness: Structure and Missions

Currently, the USSF uses an SDA taxonomy comprising 5 altitude delimited regions: very low Earth orbit (VLEO), low Earth orbit (LEO), medium Earth orbit (MEO), geosynchronous Earth orbit (GEO), and XGEO. While LEO, MEO, and GEO are all universally standard orbital regions, AFRL defines VLEO as a high-drag environment with altitudes only previously considered as part of the de-orbit phase of space operations. First employed by AFRL in 2020, the term "XGEO" is used to describe distances beyond the GEO belt, with "XGEO" denoting some multiple "X" of the GEO radial [67]. Although the inclusion of XGEO into the current SDA

taxonomy serves to highlight the necessary pivot to cislunar space awareness, the existing region-based model is limited and fails to adequately capture the scope of the Earth-Moon system.

Based on requirements of securing full domain awareness in near-Earth space and beyond, five distinct missions can be identified as comprising the broader endeavor to attain SDA:

- **Space Traffic Management**: Similar to Air Traffic Management and – from a localized perspective – Sea Traffic Management, the mission of Space Traffic Management seeks to promote safe access to and operations in the space domain. Baseline operations include the SSA function of space catalog maintenance and orbit prediction in order to ensure collision avoidance between resident space objects, such as active and retired satellites, rocket bodies, and space debris. Of note, the space debris population is continuously growing due to the lowering of launch costs; the expansion of space mission architectures; the increasing reliance on space communication, commerce and defense; and the emergence of new space-faring nations. The pursuance of Space Traffic Management is increasingly important in low Earth orbit (LEO) due to the increasingly congested nature of this orbital regime due to its ease of access and proximity to terrestrial space users. In coming years, the LEO Space Traffic Management problem will dramatically increase with the expansion of mega-constellations and introduction of new private/commercial and state-affiliated players into the space operations arena [68].

- **Space Control**: The U.S. has a vested interest in securing space superiority in order to ensure unrestricted access to and use of space to fulfill national security objectives, support terrestrial military campaigns, and, ultimately, preserve national sovereignty. Space control represents a military-centric mission intended

to counter the growing competitive and contested nature of space, and is "a mixture of defensive and offensive measures... and is particularly important during periods of increased international tensions or hostilities" [69]. One subset of the Space Control mission will mirror actions performed in the maritime domain: the protection of U.S. economic interests amidst the growing competitive nature of the space domain. This subset mission was discussed in July 2020, when the Commander of the Space Vehicles Directorate at the Air Force Research Laboratory (AFRL), Colonel Eric Felt stated that "our mission in the Space Force will become to protect... commerce, and I... talk about it in terms of protecting the 'celestial lines of commerce,' or the space lines of commerce" [37].

- **Lunar/Lagrange Point Surveillance**: A subset both Space Traffic Management and Space Control, this mission focuses on the surveillance of lunar orbit, the Earth-Moon corridor comprising of the Moon and both the L_1 and L_2 Lagrange points, and the vicinity of the unstable L_3 and stable L_4/L_5 Lagrange points. These regions are of particular interest due in part to the growing international and commercial interest in cislunar and lunar exploration. In particular, the Lagrange points proffer lucrative positions within the Earth-Moon system for a variety of missions, to include scientific monitoring of space weather and celestial bodies, as well as intra-system SSA. Consequently, surveillance of satellites operating at the Lagrange points bolsters orbit de-confliction and collision avoidance within the purview of Space Traffic Management, and the general tracking of potentially hostile space vehicles for the Space Control mission.

- **Space Weather**: Space represents a challenging operating domain for both manned and unmanned space vehicles due in large part to the natural environmental conditions. The dynamic space weather in the Solar System is primarily a function of solar activity via the generation of thermal radiation, ionizing

particles, and plasma. With events such as solar flares and coronal mass ejections, the Sun imperils satellites and their constituent electronic equipment and sensitive payloads with radiation and high-energy particles which may cause temporary or even permanent damage based on the intensity of the event [70]. Tracking Space Weather contributes to the general SDA mission and enables both the forecasting and warning of natural environmental events in order to protect space vehicles operating within the Earth-Moon system.

- **Planetary Defense**: Apart from tracking manmade objects, debris, and space weather, another mission of SDA is the tracking of objects outside of the Earth-Moon system for the purposes of Planetary Defense. Asteroids, meteors, and comets orbiting the Sun are classified as Near-Earth Objects (NEOs) when their orbits bring them within 30 million miles of Earth's orbit. NEOs pose an impact risk to both the Earth and Moon, and the active searching for and tracking of these objects enables the overall Planetary Defense mission. Currently, NASA manages this mission by providing early detection, tracking, and characterization of NEOs; in addition, NASA develops strategies and technologies for mitigating potentially hazardous objects, and plays a lead role in coordinating U.S. Government planning in response to an actual impact threat [71].

5.3 Proposed SDA Taxonomy

The increasing spatial scope of space operations will necessitate an SDA taxonomy which considers the entire Earth-Moon system rather than the near-Earth space region confined by geosynchronous and geostationary Earth orbits (GSO/GEO). The proposed SDA taxonomy comprises five distinct regions radiating outward from the Earth as shown in Fig. 35. These regions relate to different dynamical zones of operation within the Earth-Moon system, with each containing different potential SDA

missions and space system requirements for access to and operation in these regions. Some regions present more challenges to maintain a specified trajectory due to the chaotic nature of the Earth-Moon system (such as near the Earth SOI), while other regions contain more perturbations which may lead to higher propellant expenditures required (such as those regions near Earth or beyond the Earth SOI). Each region is described below with a corresponding identification of the associated spatial distance as measured radially from the center of the Earth in terms of kilometers and the canonical unit XGEO, or some multiple "X" of the GEO radial distance (or, 42,164 km above the Earth's center). The radius of the Earth is assumed to be 6378 km. For convenience, Table 28 outlines the metric and XGEO distance of each SDA region. Other key locations within the Earth-Moon system, such as the Moon and Lagrange points, are also given for comparison purposes (values are based on the Earth-Moon non-dimensional mass parameter, μ=0.01215058655). Distances are also expressed using the "DU" non-dimensional distance unit in Table 28, which is a classical and commonly used canonical unit defined as 1 DU equaling 384,400 km, or the mean distance between the Earth and Moon.

- The first three SDA regions all contain a similar naming convention exploiting the notion that space is the "ultimate high ground." The first region, or **Low Ground SDA (LG-SDA)**, encompasses "near Earth space," which includes the common orbital regimes of LEO, MEO, and GSO/GEO. Specifically, LG-SDA extends from the Von Karman Line ($\sim$100 km from the surface of the Earth), a nominal delimitation for the start of space, out to super-synchronous orbit beyond GEO (42,464 km from the center of the Earth), an orbital regime approximately 300 km above GEO typically used for spacecraft disposal at mission end-of-life. The LG-SDA region contains most current space operations, to include both Earth and space surveillance missions, and represents the highest

density of resident space objects and debris to search, detect, track, characterize, and catalog for the general ground- and space-based SDA mission. In terms of the XGEO canonical unit, the LG-SDA region extends from the planetary surface to about 1XGEO.

- Next, **Mid-Ground SDA (MG-SDA)** denotes SDA operations occurring in the region of space commonly referred to as "cislunar," or the spherical volume of space extending from super-synchronous orbit to the Moon's orbit. The MG-SDA region also contains all five Lagrange points and extends 15,000 km beyond the collinear L_2 Lagrange point (∼465,000 km). Therefore, MG-SDA encompasses space operations occurring from ∼42,500 km to 480,000 km as measured from the Earth's center, or between 1-11.4XGEO. Plans and developments of space-based infrastructure, both nationally and internationally, in cislunar space are rapidly growing, thus making MG-SDA an attractive region for performing SDA in the near future.

- **High-Ground SDA (HG-SDA)** is the next region in the proposed SDA taxonomy, and is associated with the translunar[1] orbital regime of the Earth-Moon system. The HG-SDA spherical region begins at the outer boundary of the MG-SDA region (480,000 km) and extends to 25,000 km below the Earth gravitational SOI, a demarcation occurring at approximately 925,000 km from the Earth (or, 21.9XGEO). The Earth's graviational SOI is calculated from Eq. (71):

$$r_{SOI} = r_{S/e}\left(\frac{m_e}{m_S}\right)^{\frac{2}{5}} \tag{71}$$

where r_{SOI} is the radius of the Earth's sphere of influence with respect to the

[1]The term "translunar" refers to the volume of space beyond the Moon and its orbit.

Sun, $r_{S/e}$ is the distance to the Sun with respect to the Earth, m_e is the mass of the Earth, and m_S is the mass of the Sun. At the Earth SOI, the effects of solar gravity begin to supersede that of Earth's gravity. Therefore, HG-SDA will be defined as SDA operations occurring between 480,000-900,000 km, or 11.4-21.3XGEO.

- Beyond the HG-SDA layer is the **Parapet SDA (P-SDA)** region, a spherical volume containing the demarcation of the Earth-Moon gravitational sphere of influence, and extending 25,000 km both above and below said boundary. The gravitational SOI is loosely analogous to the dynamical "wall" or "fence" of the Earth-Moon system and, as a result, the P-SDA region derives its name from the parapet of a castle wall, or the protected walkway and/or battlement located on top of a castle wall [72]. In terms of spatial distance, P-SDA defines operations occurring between 900,000-950,000 km, or 21.3-22.5XGEO. Orbital trajectories residing exclusively within the P-SDA region are challenging to define and maintain due to the chaotic instabilities of the Earth-Moon gravitational system at this distance. As a result, space systems seeking to perform a P-SDA mission will likely require orbits that traverse other regions within the Earth-Moon system so as to deliver the necessary transit times in and around the sphere of influence.

- The final region within the proposed taxonomy is referred to as **Fence Line SDA (FL-SDA)**. Continuing the analogy of the gravitational SOI resembling a pseudo-barrier, FL-SDA embodies the concept of performing surveillance and security operations outside of a given fence or wall that may surround a forward operating base in theater, or a secure installation. Space system orbits within the FL-SDA region are still influenced by the gravity of the Earth-Moon system; however, the gravitational influences of the Sun have a greater effect on the

trajectory. Tertiary bodies external to the Earth-Moon system also become increasingly relevant at this distance. A given SDA mission could extend well beyond the Earth SOI based on the needs of the mission and the corresponding design of the orbital trajectory, therefore, an outer boundary for the FL-SDA is only estimated herein. For the purposes of this paper, the FL-SDA region starts at 950,000 km from the Earth and extends to approximately 2.3M km, or 22.5-55XGEO.

Table 28: Distance Measurements of SDA Regions and Locations of Interest within the Earth-Moon System (measured with respect to the Earth Center)

Location of Interest	**Average Radial Distance from Earth Center**		
	Kilometers	**XGEO**	**DU**
GEO	42,164	1	0.1097
L_1	326,394	7.7	0.8491
L_2	448,940	10.6	1.1679
L_3	381,632	9.0	0.9928
L_4	384,400	9.1	1.0
L_5	384,400	9.1	1.0
Moon	384,400	9.1	1.0
LG-SDA Region	6478 - 42,500	0.2 - 1.0	0.0169 - 0.1105
MG-SDA Region	42,500 - 480,000	1.0 - 11.4	0.1106 - 1.2487
HG-SDA Region	480,000 - 900,000	11.4 - 21.3	1.2487 - 2.3413
Sphere of Influence	925,000	21.9	2.4063
P-SDA Region	900,000 - 950,000	21.3 - 22.5	2.3413 - 2.4714
FL-SDA Region	950,000 - 2.3M	22.5 - 55	2.4714 - 5.9834

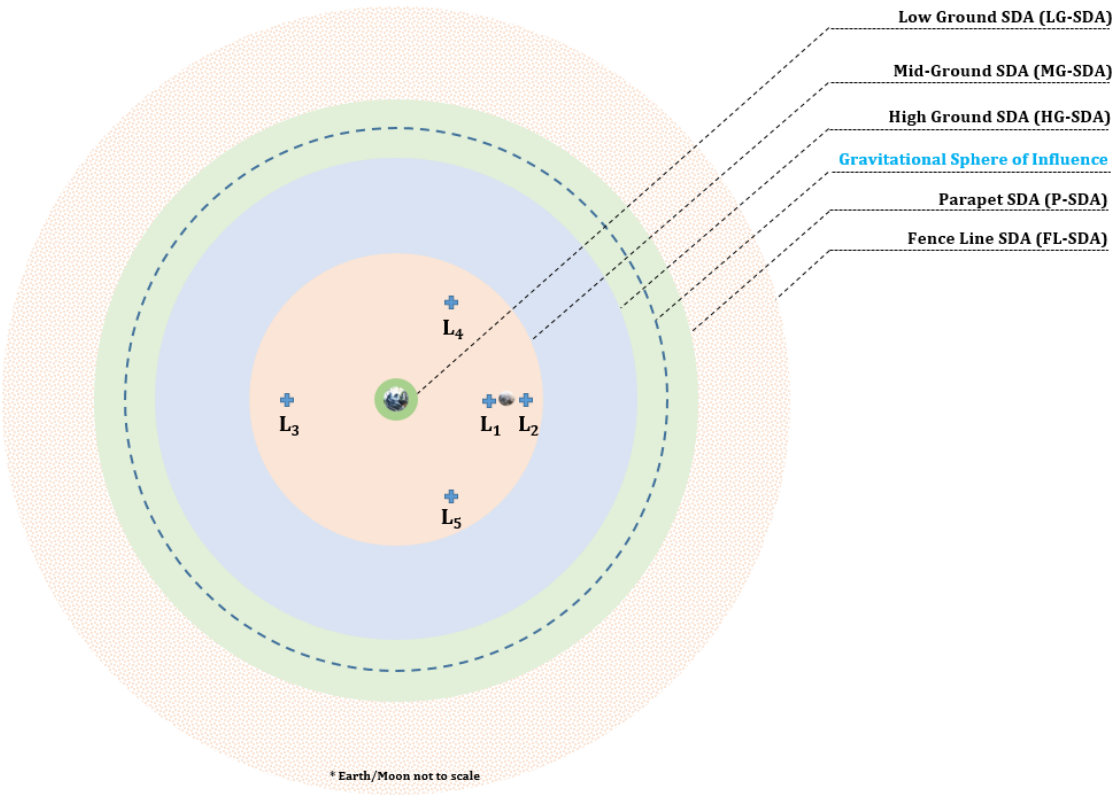

Figure 35: Proposed Earth-Moon System SDA Taxonomy (not to scale)

5.4 Mission Mapping and Orbits within Proposed Taxonomy

Although an SDA taxonomy can be proposed, its usability and attractiveness for implementation ultimately arises with a discussion of mission allocation per region comprising the taxonomy, as well as the types of trajectories which can be generated to perform these missions. A cursory mapping of SDA missions to each region is given in Table 29 with corresponding spatial bounds expressed in XGEO units as a reference (and reiteration) of the size of each region. Nominally, the Space Traffic Management mission will reside in the regions closest to the Earth and Moon, specifically LG-SDA and MG-SDA, due to issues related to orbital congestion and collision avoidance between spacecraft and resident space objects (e.g., debris). The Space Control mission will similarly reside in regions where Space Traffic Management is a

priority. However, the inclusion of HG-SDA as a potential region for Space Control is provided in Table 29 due to the vantage point that translunar space proffers for 'inward' surveillance of the Earth, Moon, and orbital regimes of interest in the LG- and MG-SDA regions. Overall, the Space Weather mission can be performed in any orbital regime within the Earth-Moon system based on specific program needs, such as scientific observation or warning. In Table 29, the outer regions of HG-SDA, P-SDA, and FL-SDA are identified as potential areas for Space Weather missions due to their distance from both the Earth and Moon, thereby proffering an 'outward' surveillance perspective for pseudo-early warning of Space Weather events. While true early warning of events such as solar flares and coronal mass ejections occur at the Sun-Earth Lagrange Points, the placement of monitoring spacecraft in trajectories traversing HG-SDA or outer regions enable a second-tier for warning and event intensity. As previously stated, surveillance of the Moon and Earth-Moon Lagrange points is of interest due to the planned infrastructure development at or near these locations in the coming years. Specifically, the collinear L_1 and L_2 Lagrange points around the Moon have become a focus for mission planners due to their proximity to the Moon. For instance, the Lunar Gateway, a critical component of NASA's Artemis program which will provide "vital support for a long-term human return to the lunar surface [and] a staging point for deep space exploration," is planned to orbit near L_2 [73]. Therefore, the lunar and Lagrange point surveillance mission will occur in either the MG-SDA or HG-SDA region.

The final mission set, Planetary Defense, is identified herein as appropriate for the P- and FL-SDA regions. These regions give the ultimate vantage point for the 'outward' surveillance of NEOs and other transient asteroids/meteoroids which may pass near or traverse the Earth SOI. Early warning is critical to averting and/or preparing for catastrophe arising from an NEO or similar piece of cosmic debris,

and the stand-off distance of approximately 21-55 XGEO established by the P- and FL-SDA regions contribute to an early warning posture for Planetary Defense. In addition to surveillance, the vast spatial volumes of the P- and FL-SDA regions also enable the fielding of defensive systems to deflect and/or destroy potential threats arising from outside the Earth-Moon system.

Table 29: Mapping of SDA Missions to Proposed Spatial Regions

Region	XGEO Distance	Mission Examples
LG-SDA	0.2 - 1.0	Space Traffic Management Space Control
MG-SDA	1.0 - 11.4	Space Traffic Management Space Control Lunar/Lagrange Point Surveillance
HG-SDA	11.4 - 21.3	Space Control Space Weather Lunar/Lagrange Point Surveillance
P-SDA	21.3 - 22.5	Planetary Defense Space Weather
FL-SDA	22.5 - 55.0	Planetary Defense Space Weather

Multi-body gravitational systems are inherently chaotic, therefore, small changes to the initial position and velocity of a spacecraft can generate large changes in overall trajectory. Despite the chaotic challenges posed by gravitational fields such as the Earth-Moon system, periodic orbits are indeed possible which permit repeating trajectories which are beneficial for a variety of missions sets, especially SDA. Different dynamical models can be employed to explore and generate periodic orbits, with all models seeking to simplify the gravitational field by examining the complex dynamical interactions of a limited number of bodies. Using the dynamics assumed by the circular restricted three-body problem (CR3BP), a trajectory model which

considers only the gravitational influences of the Earth and Moon on the spacecraft, example periodic orbits were generated which correspond to each region comprising the proposed SDA taxonomy, and are shown in Fig. 36. In Fig. 36(a), the dotted/-dashed line identifies geosynchronous orbit in relation to the example LG-SDA orbit; for Figs. 36(b)-36(f), the dotted/dashed line identifies the Earth SOI. The unique design of each example periodic orbit is the result of trajectory generation performed with respect to the synodic reference frame, a rotating refence frame with the Earth and Moon held on the x-axis. While the exact shape of a given orbit will change based on the perspective of the viewer (e.g., from the Earth or Sun), the spatial volume within which a given orbit traverses remains the same. As a result, periodic orbits can be built which provide surveillance coverage to key locations within the Earth-Moon system, to include the Moon, Lagrange Points, Earth SOI, and outside the Earth SOI.

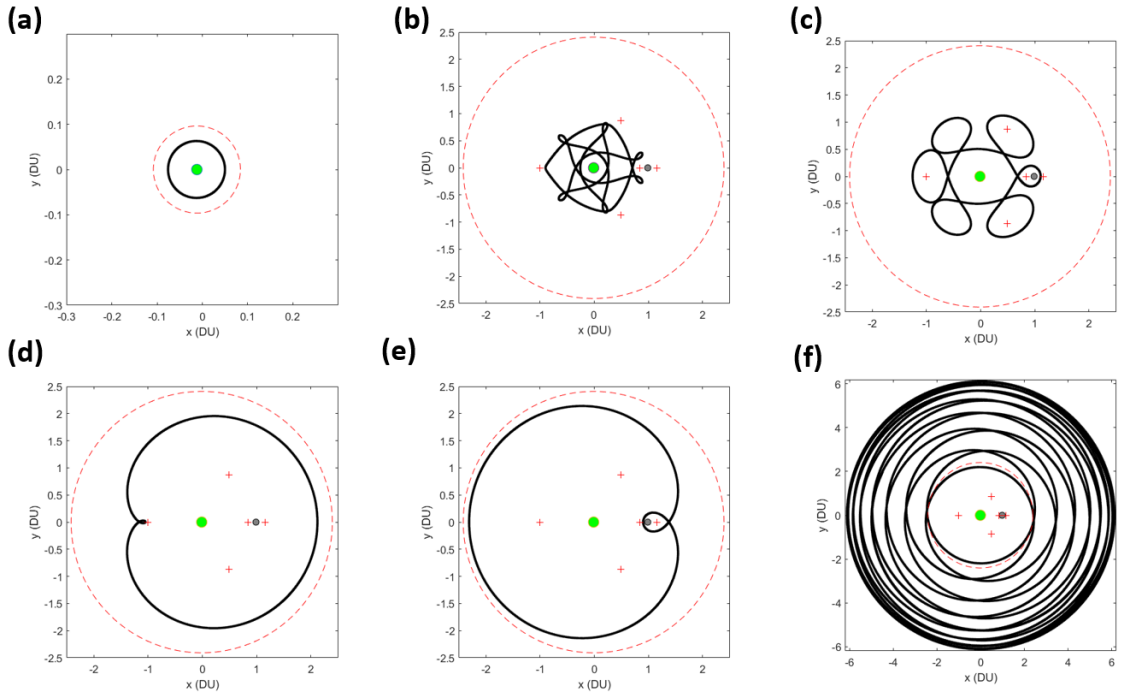

Figure 36: Example SDA Orbits: (a) Low Ground SDA; (b) Mid-Ground SDA; (c) Mid-Ground SDA; (d) High Ground SDA; (e) Parapet SDA; and (f) Fence Line SDA

The initial conditions for the orbits in Fig. 36 are shown in Table 30:

Table 30: Initial Conditions for Fig. 36 ($\mu = 0.012150584673414$)

Parameter	(a)	(b)	(c)	(d)	(e)	(f)
x_0	0.05	-0.9	1.105	-1.05	0.9026	-2.5
y_0	0	0	0	0	0	-0.5
z_0	0	0	0	0	0	0
$\dot{x}_0$	0	0	0	-0.04	0	-0.15
$\dot{y}_0$	3.95	-0.099452	-0.57019	-0.08101	0.6566173	1.85
$\dot{z}_0$	0	0	0	0	0	0
T_0	0.3	35.0	31.0	12.5	11.0	150

For any space mission, two (of many) critical decisions center around mode of orbit access and mission lifetime. While the former decision focuses on the type of launch vehicle required to reach a particular orbital regime and whether a given spacecraft will be the primary or secondary/rideshare payload, the latter decision addresses lifetime, in part, as a function of total propellant availability and the ability to perform orbital maneuvers (e.g., orbit maintenance). Within the Earth-Moon system, spacecraft can be injected into periodic orbits such as those portrayed in Fig. 36 via direct launch from either the Earth or Moon. Only launch from the Earth is currently feasible, but the construction of lunar infrastructure in coming decades will enable the launching of spacecraft into periodic orbits which pass near the Moon (e.g., Figs. 36(c), 36(e)) at relatively low propellant cost. By comparison, lunar launch will require less propellant than conventional Earth-based launch due to a weaker gravitational field and the absence of virtually any atmosphere. Regarding orbit maintenance, periodic orbits in the Earth-Moon system may remain stable for weeks depending on the selected geometry, particularly how closely a trajectory passes by the Earth, Moon, or the various Lagrange Points. We assess that orbit maintenance,

or the expenditure of propellant to maintain a desired orbital geometry, will take on the order of 10-100's of meters per second of ΔV per period depending on the distance of the orbit from the Earth. This low-order amount of required propellant for orbit maintenance will enhance any SDA mission in terms of lifetime and desirability for implementation. A second consideration for mission lifetime is the actual time-based lifetime of a spacecraft measured in weeks, months, or years depending on the type of spacecraft, intended mission, and the orbital period (T). For spacecraft operating with the LG-SDA region, the period will be in the range $1.5 \leq \mathrm{T} \leq 24.2$ hours, depending on the orbital regime. Moving higher into the remaining regions, the period will be highly variable based on the selected geometry of a periodic orbit. For example, the period for the orbits in Figs. 36(b) and 36(c) are approximately 152 and 135 days, respectively. The variation in period between these orbits is due to the difference in geometric complexity, with the orbit in Fig. 36(b) featuring more looped segments and a longer orbital path than that in Fig. 36(c). Due to the simplistic geometries selected for Figs. 36(d) and 36(e), coupled with the distance of these orbits from the Earth, the periods are comparatively lower at approximately 56 and 48 days, respectively. Finally, Fig. 36(e) features the longest period of the example orbits at about 651 days. This duration, approximately 1.75 years, is a function of the complex switch-back design of the orbit and the spatial volume traversed outside the SOI, where orbital velocity is the lowest of the examples presented herein. When designing SDA missions in any of these proposed regions, the duration of a single period will influence the number of spacecraft to perform the mission. In order to provide a desired level of sensor coverage and re-visit time in a particular region, multiple spacecraft will likely be needed – either with phased operation in the same periodic orbit, or with the spacecraft spread over different, yet similar periodic orbits. For example, the need for a constellation of SDA spacecraft will likely be important

for the planetary defense mission in the FL-SDA region. Due to a single period being on the order of approximately 1-1.5 years, numerous spacecraft - potentially on the mega-constellation scale - may be needed to provide a timely and persistent monitoring and defense posture for threats external to the Earth-Moon system.

5.5 Summary

With the development and growth of the USSF, new policy and doctrine will develop with the aim of securing U.S. space dominance. As such, new terminology will be vital to viewing space as a warfighting domain, as well as better describing missions - such as SDA - which ensure the continuous protection of U.S. space assets. This work serves to propose a new SDA taxonomy for future missions contained in or around the Earth-Moon system that will assist in the development of new procedures when discussing SDA missions in the Earth-Moon system. Five SDA regions were presented in this work: Low-Ground SDA (LG-SDA), Mid-Ground SDA (MG-SDA), High-Ground SDA (HG-SDA), Parapet SDA (P-SDA), and Fence Line SDA (FL-SDA). Particular points in the Earth-Moon system, such as Lagrange points, and regions in which trajectory dynamics become chaotic, such as near the Earth SOI, are markers for regional boundaries in this new taxonomy. All proposed regions correspond to varying distances away from the Earth and varying SDA mission subsets, to include space traffic management, space control, space weather observation, lunar/Lagrange point surveillance, and planetary defense. Each region is described with a corresponding identification of the associated spatial distance as measured radially from the center of the Earth in terms of kilometers and the canonical unit XGEO, a common unit used by AFRL when describing regions past GEO.

In the early years of spaceflight, space operations primarily consisted of near-Earth missions with few spacecraft ever venturing to the Moon. As time progressed,

more and more missions began extending beyond the confines of geosynchronous orbit. This pattern continues to today, with the contemporary space domain facing increasing concerted efforts around the world to reach and operate within the cislunar environment. The future will likely see a similar trend of extending outward to the new high-grounds with missions becoming more and more frequent near the Moon, in the High-Ground SDA region, and beyond. As such, it is important to develop policy and terminology which will address the evolving SDA mission, one which will come to embrace the entirety of the Earth-Moon system and its celestial environs.

VI. Artificial Debris Propagation in Cislunar Periodic Orbits

6.1 Chapter Overview

This chapter seeks to analyze the potential debris-related consequences of a catastrophic explosion on-board spacecraft traveling along select cislunar periodic orbits, identified herein as Debris Orbits. This case study features cislunar periodic orbits with host notional spacecraft that are subjected to catastrophic breakup events at various location along their trajectories, which are simulated using the dynamics of the bicircular restricted four-body problem (BCR4BP). Analysis of the survivability of another notional spacecraft traveling along the same periodic orbit, displaced one run[1] ahead of where the mishap occurs, is then conducted to quantify the risks from the debris event to another spacecraft operating in a theoretical cislunar periodic orbit constellation. Finally, the orbital states of debris fragments at the end of the simulation window will be used to evaluate the potential risk to orbital regimes near Earth and the Moon due to a cislunar periodic orbit debris event. Each case study showed debris that spread throughout cislunar space; however, the overall risk to any one spacecraft was very low in each case.

Credit is given to Nathan Boone who assisted with this portion of the research. Specifically, Cislunar periodic orbit initial conditions and mishap locations were given to Boone to perform debris simulations; Boone wrote his thesis [3] on cislunar debris propagation following a catastrophic spacecraft mishap. Results of these simulations are presented in this Chapter. Part of this research was presented at the 2021 AAS/AIAA Astrodynamics Specialist Conference [74] and is currently under review for the Journal of Space Safety Engineering.

[1]Each simulations consists of 8 "runs" which are locations which the catastrophic explosion takes place. The run locations were chosen to be at critical parts of the orbit, such as near Lagrange points, close approaches to the Earth and/or the Moon, or near trajectory crossings.

6.2 Rationale of Debris Analysis

Despite programmatic efforts to mitigate the onset of spacecraft failure, mishaps may occur and threaten not only the mission integrity of a given spacecraft, but also the safety of other spacecraft in a given orbital regime. A catastrophic spacecraft mishap, such as a breakup event in a cislunar periodic orbit, may generate a significant number of artificial debris fragments that could threaten other spacecraft in cislunar space, especially if those spacecraft are operating in a cislunar periodic constellation. In addition, the close approaches to the Earth and Moon present in some periodic orbits may cause the debris from a catastrophic mishap to threaten other spacecraft operating near these bodies. To date, the most famous spacecraft mishap that generated debris in cislunar space is the Apollo 13 oxygen tank explosion. This event created a debris cloud that trailed the Apollo 13 vehicle along its translunar trajectory and precluded the on-board sextant device from sighting stars for navigation [75]. A recent debris propagation study [45] demonstrated that the debris from a similar debris-generating event could potentially threaten spacecraft in both the low Earth orbit (LEO) and geostationary Earth orbit (GEO) environments as the debris fragments traverse those orbital regimes during their circulation of wider cislunar space. Future lunar missions could also be threatened by debris circulating cislunar space on short- and long time-scales alike, with debris potentially posing a risk for missions operating weeks or even years following a given breakup event. Overall, research into cislunar periodic orbit debris propagation enhances operational planning for future Earth-Moon space traffic management and develops an understanding of the debris-related consequences of spacecraft mishaps along cislunar periodic orbits.

6.3 Cislunar Periodic Orbits Used for Debris Propagation

The first cislunar periodic orbit example to be analyzed is the Interstellar Boundary Explorer (IBEX), whose initial conditions were obtained from Dichmann [76]. In 2011, the IBEX was set to perform an extended mission and, in doing so, transferred into an orbit which was near 3:1 resonance with the Moon [77]. In reality, this orbit contains oscillations making it quasi-periodic [76], meaning that it maintains the same general shape with slight variation of path on each period. While not an exact periodic orbit, this orbit is still included in this research due to its real-world application. A top-down view of this quasi-periodic orbit with annotated run locations is shown in Fig. 37.

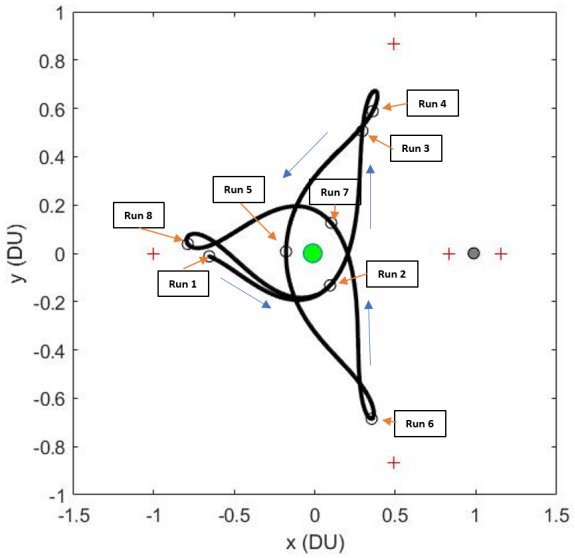

Figure 37: IBEX Quasi-Periodic Orbit w/ Mishap Annotation

The second, third, and fourth cislunar periodic orbit examples to be analyzed are trajectories formulated by Arenstorf [25, 26]. These cislunar periodic orbits use a non-dimensional mass parameter of $\mu = 0.012277471$, which was commonly used in the 1960s by Arenstorf and his contemporaries such as Davidson [66]. Top-down views of these periodic orbits with annotated run locations are given in Figs. 38,

39, and 40. These examples feature planar trajectories that reside in the x-y plane with $z = 0$. Of note, periodic orbit 3 in Fig. 39 is symmetric about the x-axis and encompasses both the L_1 and L_3 points; alternatively, periodic orbit 4 in Fig. 40 is symmetric about the x- and y-axis and features proximity passes of the Earth, the Moon, and L_3.

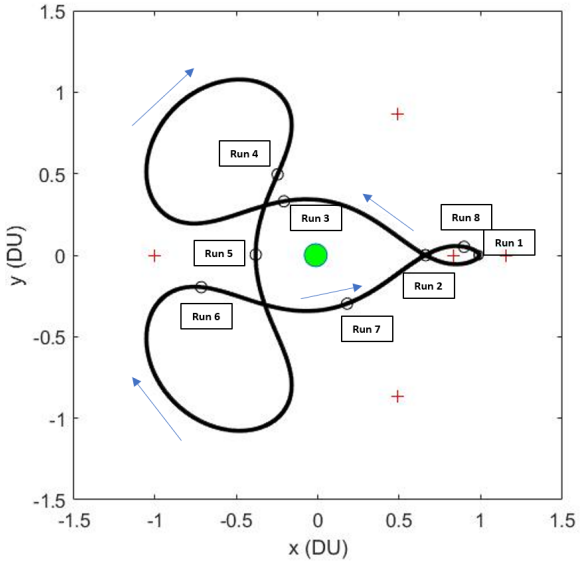

Figure 38: Debris Orbit 2 w/ Mishap Annotation

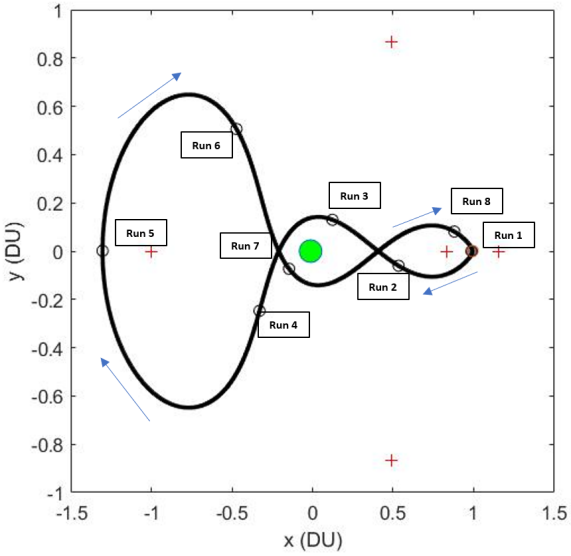

Figure 39: Debris Orbit 3 w/ Mishap Annotation

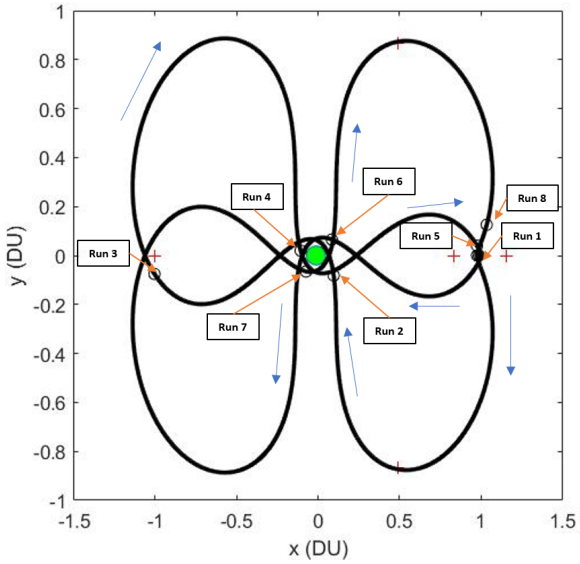

Figure 40: Debris Orbit 4 w/ Mishap Annotation

The fifth and final periodic orbit example to be analyzed is a three-dimensional trajectory formulated by Vaquero and Howell [78, 79]. a top-down view of this orbit with annotated run locations is shown in Fig. 41.

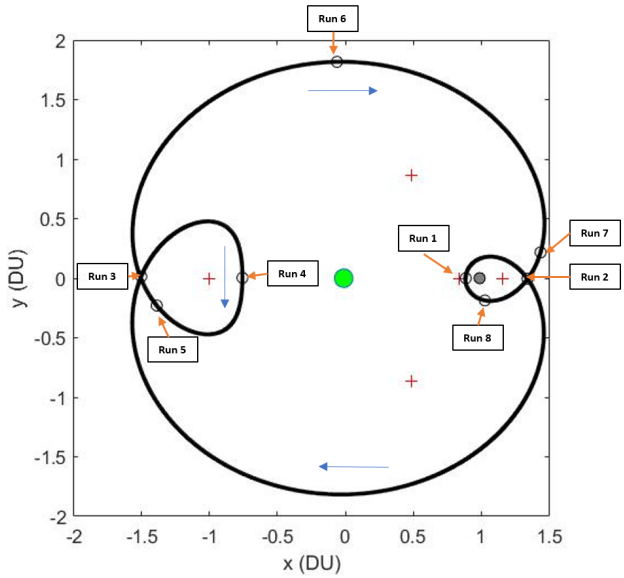

Figure 41: Debris Orbit 5 w/ Mishap Annotation

Since the orbits in Figs. 37-41 were initially created with varying μ values, the

initial conditions were corrected via differential correction in the CR3BP to fit a standard non-dimensional mass parameter, $\mu = 0.012150584673414$. The μ value provided by Dichmann [76] for the IBEX was nearly equivalent to the μ value used in this analysis, therefore no correction was performed on the IBEX initial conditions. The initial conditions for Debris Orbits 2, 3, and 4 were previously presented in Table 15. The initial conditions for the IBEX and corrected initial conditions for Debris Orbit 5 are shown in Table 31:

Table 31: IBEX and Debris Orbit 5 Initial Conditions Used in Debris Analysis

	IBEX	Debris Orbit 5
x_0	-0.6546	0.886004483448809
y_0	-0.0126	0.000000000069543
z_0	0.1162	-0.001000000180988
$\dot{x}_0$	0.5619	0.000026138540531
$\dot{y}_0$	-0.1561	0.6091208
$\dot{z}_0$	-0.1723	0.000000275457282
T_0	6.5	17.0

The sixth, seventh, eighth, and ninth cislunar periodic orbits analyzed are trajectories whose initial conditions were recently discovered during this research and analyzed in SDA scenarios previously in Chapter IV. These orbits feature planar trajectories that reside in the x-y plane with $z = \dot{z} = 0$. Top-down views of these periodic orbits with annotated run locations are given in Figs. 42, 43, 44, and 45.

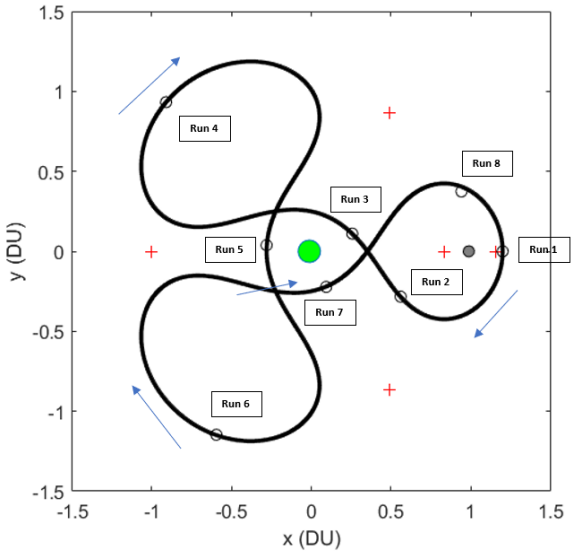

Figure 42: Debris Orbit 6 w/ Mishap Annotation

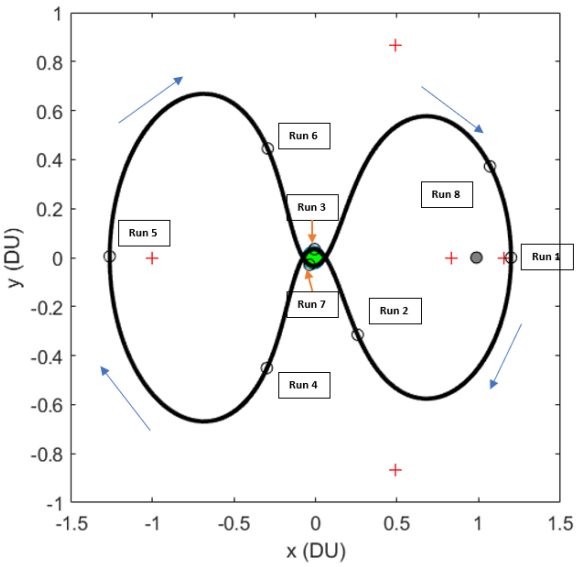

Figure 43: Debris Orbit 7 w/ Mishap Annotation

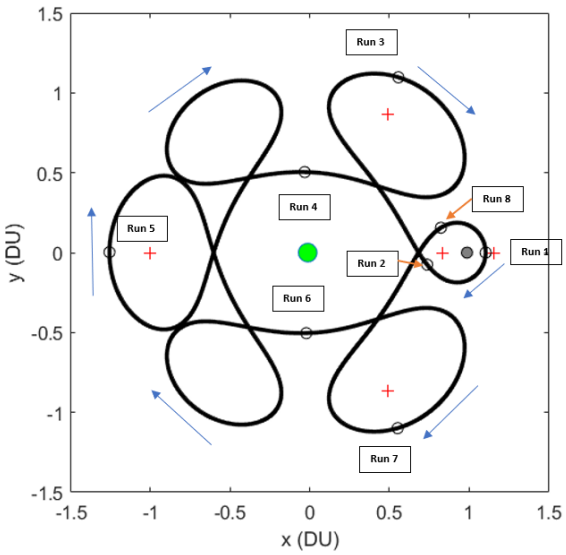

Figure 44: Debris Orbit 8 w/ Mishap Annotation

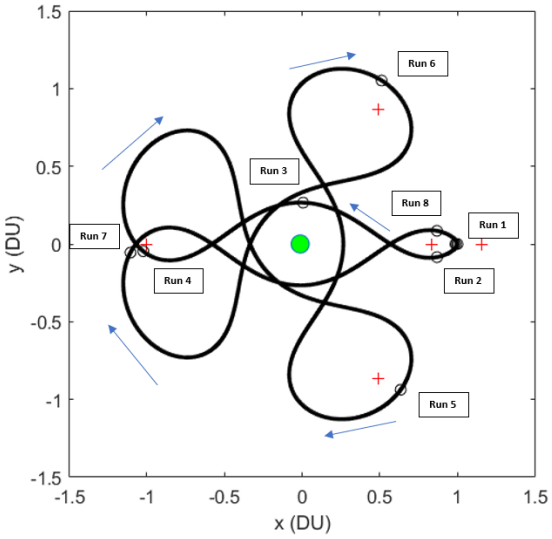

Figure 45: Debris Orbit 9 w/ Mishap Annotation

The initial conditions of Debris Orbits 6-9 were previously presented in Table 13. As shown above, periodic orbits 6 and 9 are symmetric about the x-axis; alternatively, periodic orbits 7 and 8 are symmetric about both the x- and y-axis. Debris Orbit 7 features a close proximity pass of the Earth, while Debris Orbit 9 features a close proximity pass of the Moon. Debris Orbits 8 and 9 encompass the L_1, L_3, L_4, and

L_5 Lagrange points; alternatively, Debris Orbits 6 and 7 encompass both the L_1 and L_2 Lagrange points, with Debris Orbit 7 also encompassing the L_3 Lagrange point.

6.4 Results and Discussion

In order to study debris propagation in cislunar periodic orbits, a notional spacecraft is assumed to be traveling along a cislunar periodic orbit trajectory prior to undergoing a catastrophic mishap. Mishaps are simulated at critical parts of the orbit, such as near Lagrange points, close approaches to the Earth and/or the Moon, or near trajectory crossings. This will maximize the probability of collateral damage occurring, thus providing an upper bound on the expected amount of damage such mishaps could cause. The cislunar periodic orbits analyzed consisted of four custom trajectories, three presented by Arenstorf [26], one presented by Vaquero and Howell [78, 79], and one used by the Interstellar Boundary Explorer (IBEX) spacecraft. Between these nine orbits, two different vulnerability models (one which was mass-dependent and another which was mass and velocity-dependent) were used to determine probability of kill for the spacecraft hit by the debris. Initial analysis provided results for the IBEX and Debris orbits 2-5 using the mass-dependent vulnerability model. Later in the research, a new vulnerability model was created and the IBEX as well as Debris Orbits 6-9 were analyzed using this new model.

6.4.1 Mass-Dependent Results

During initial analysis, the IBEX and Debris Orbits 2-5 were subject to the mass-dependent vulnerability model. This analysis was performed before the mass and velocity dependent vulnerability model was created. Prior to simulations, all Debris Orbit initial conditions were adjusted for a standardized μ value of 0.012150584673414. For each cislunar periodic orbit, catastrophic spacecraft mishaps were simulated for

8 different initial starting locations (or run), with debris particle trajectories propagated 50 days from the time of the mishap. A notional spacecraft is located at a phase offset (one run ahead) from each mishap location and the mass-dependent survivability model is applied to assess the total probability of hazard to this spacecraft due to collisions with space debris. In addition, the risks to spacecraft near Earth and elsewhere in cislunar space are evaluated based on the number of particles that feature a perigee that is within GEO altitude, or orbit within either the lunar or Earth sphere of influence (SOI) at the end of each simulation.

Figures 46-51 show debris propagation snapshots at 6 TU elapsed time for all 8 simulation runs across each of the five cislunar periodic orbits. Subplots (a) through (h) corresponding to Runs 1 through 8, respectively. The green circle marks the location of the Earth, the black circle marks the location of the Moon, and the red crosses mark the locations of the Lagrange points. The yellow line indicates the current direction to the Sun, the blue star (*) indicates the location of the non-mishap spacecraft, and the black dots represent debris particles. Due to the three-dimensional geometry of the IBEX orbit, there are additional debris propagation snapshots showing the z-direction in Fig. 47 for 1, 3, 6, and 9 TU elapsed time. For Orbits 1-5, the starting locations of each run, along with the mishap time (in Time Units), and the corresponding total probability of hazard to the nearby spacecraft are shown in Tables 32, 34, 36, 38, and 40 for Debris Orbits 1-5, respectively. The locations of all particles in the Earth-Moon system at the end of each run are given in Tables 33, 35, 37, 39, and 41 for Debris Orbits 1-5, respectively.

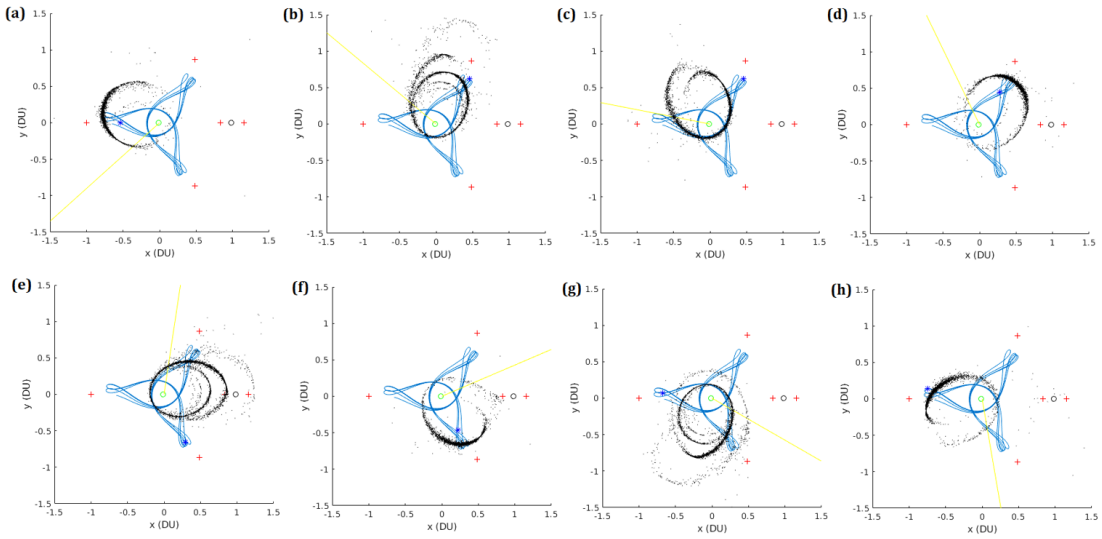

Figure 46: Debris Propagation Snapshot at $\Delta T = 6$ TU Elapsed Time for IBEX

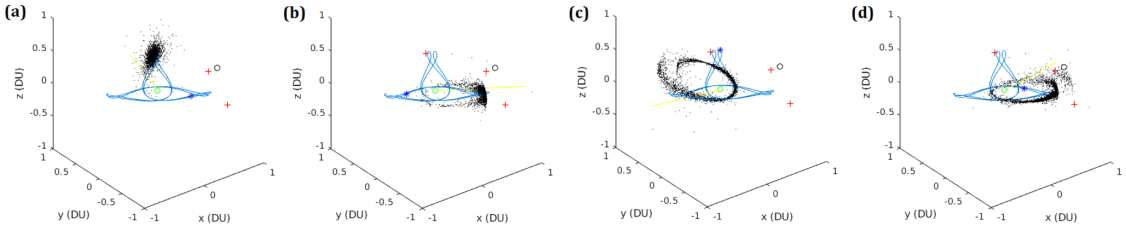

Figure 47: Three-Dimensional Debris Propagation Snapshot at $\Delta T = 1, 3, 6, 9$ TU Elapsed Time for IBEX (Run 3)

Table 32: Total Probability of Hazard for Catastrophic Mishaps in IBEX

Run Locations	Run	Mishap Time (Elapsed Time)	Total P_{HZ}
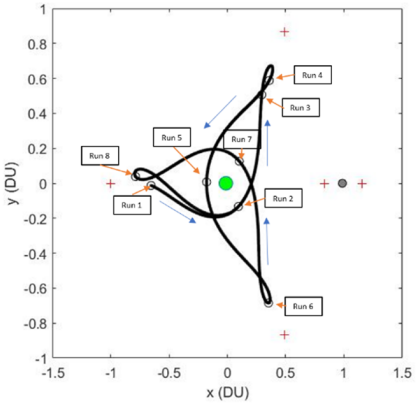	1	0 TU	4.63×10^{-10}
	2	0.55 TU	1.38×10^{-9}
	3	1 TU	8.87×10^{-10}
	4	2 TU	4.69×10^{-10}
	5	2.65 TU	9.18×10^{-10}
	6	3.75 TU	5.31×10^{-10}
	7	4.75 TU	5.15×10^{-10}
	8	5.7 TU	1.07×10^{-9}

Table 33: Number of Debris Particles at Simulation End for IBEX

Run Number	Escaped Earth-Moon System	Impacted Moon	Impacted Earth	End in Lunar SOI	End in Earth SOI	Perigee within GEO
1	**2**	**0**	**0**	**1**	**2597**	**18**
2	**23**	**0**	**0**	**0**	**2890**	**0**
3	**3**	**1**	**1**	**2**	**2926**	**38**
4	**1**	**2**	**1**	**0**	**2912**	**33**
5	**24**	**0**	**0**	**0**	**3055**	**0**
6	**1**	**0**	**2**	**2**	**2907**	**31**
7	**26**	**0**	**0**	**0**	**2941**	**0**
8	**8**	**1**	**1**	**1**	**2907**	**12**

For all mishap location runs of the IBEX, there is minimal risk of either an Earth or lunar impact. The vast majority of particles remained on the same IBEX-shaped trajectory after mishap occurred. This is likely due to the great distance between the trajectory and Moon, coupled with the absence of near-Earth passes. With the debris field remaining primarily along the orbit path (the most of all the orbits analyzed), the IBEX features the highest risk to collision with the notional spacecraft, even though the risk is relatively low. In terms of geometry, the debris after all runs for IBEX formed the appearance of a rotating elliptical orbit about the Earth. Across all 8 runs of the IBEX, the average relative speed of the debris particles (with respect to the notional spacecraft) contained in the danger zone was 902 m/s.

The next orbit analyzed was presented in the work of Arenstorf [25, 26] in the 1960s. Results of this orbit are shown below:

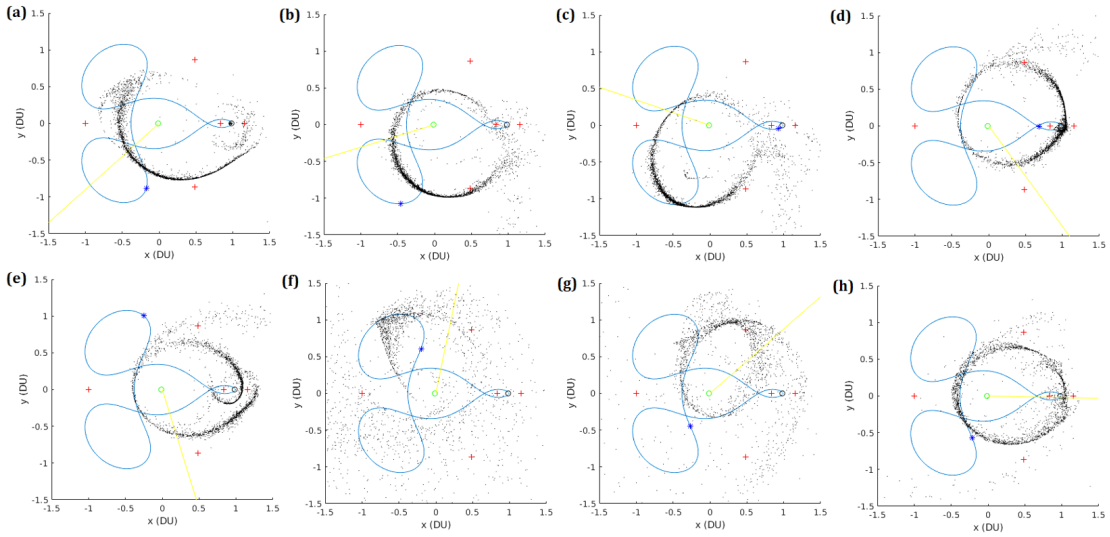

Figure 48: Debris Propagation Snapshot at $\Delta T = 6$ TU Elapsed Time for Debris Orbit 2

Table 34: Total Probability of Hazard for Catastrophic Mishaps in Debris Orbit 2

Run Locations	Run	Mishap Time (Elapsed Days)	Total P_{HZ}
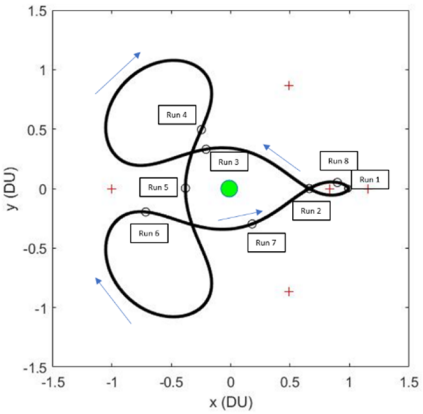	1	0 TU	3.04×10^{-10}
	2	0.47 TU	7.38×10^{-11}
	3	1.15 TU	5.88×10^{-11}
	4	5.2 TU	2.34×10^{-10}
	5	5.56 TU	3.2×10^{-11}
	6	9.5 TU	3.55×10^{-11}
	7	10.2 TU	2.68×10^{-11}
	8	11 TU	7.11×10^{-11}

Table 35: Number of Debris Particles at Simulation End for Debris Orbit 2

Run Number	Escaped Earth-Moon System	Impacted Moon	Impacted Earth	End in Lunar SOI	End in Earth SOI	Perigee within GEO
1	**30**	**142**	**38**	**288**	**2307**	**95**
2	**89**	**24**	**0**	**273**	**2648**	**10**
3	**145**	**37**	**0**	**6**	**2763**	**46**
4	**277**	**52**	**0**	**17**	**2548**	**39**
5	**323**	**79**	**0**	**60**	**2170**	**59**
6	**467**	**79**	**0**	**8**	**2197**	**22**
7	**622**	**457**	**1**	**0**	**1909**	**106**
8	**68**	**481**	**2**	**64**	**2239**	**157**

When compared to the IBEX, there are significantly more instances in Debris Orbit 2 in which the particles impacted the Moon. This is to be expected since there is a close proximity lunar pass along the Debris Orbit 2 trajectory. However, Run 1 was the only mishap location which resulted in a small but notable number of Earth impacts. The comparatively higher number of lunar impacts are likely due to the mishap occurring so close to the Moon that any change in initial condition causes a large change in particle trajectory. Both Runs 7 and 8 resulted in the largest amount of particles impacting the Moon, which is due to the velocity in both of these runs pointing in the direction of the Moon, thus causing the debris cloud to intersect the Moon.

In terms of the geometry of the particle cloud, the debris particles in Runs 2 and 8 appear to form a rotating elliptical orbit about the Earth. In Runs 6 and 7 the debris particles scatter all across the system, thus highlighting the chaotic nature of the gravitational dynamics within the Earth-Moon system. Across all 8 runs of Debris Orbit 2, the average relative speed of the debris particles (with respect to the notional spacecraft) contained in the danger zone was 633 m/s. This represents the second lowest relative speed of all of the orbits analyzed.

Similar to Orbit 2, Orbit 3 was also presented in the work of Arenstorf[25, 26] in the 1960's. Results of this orbit are shown below:

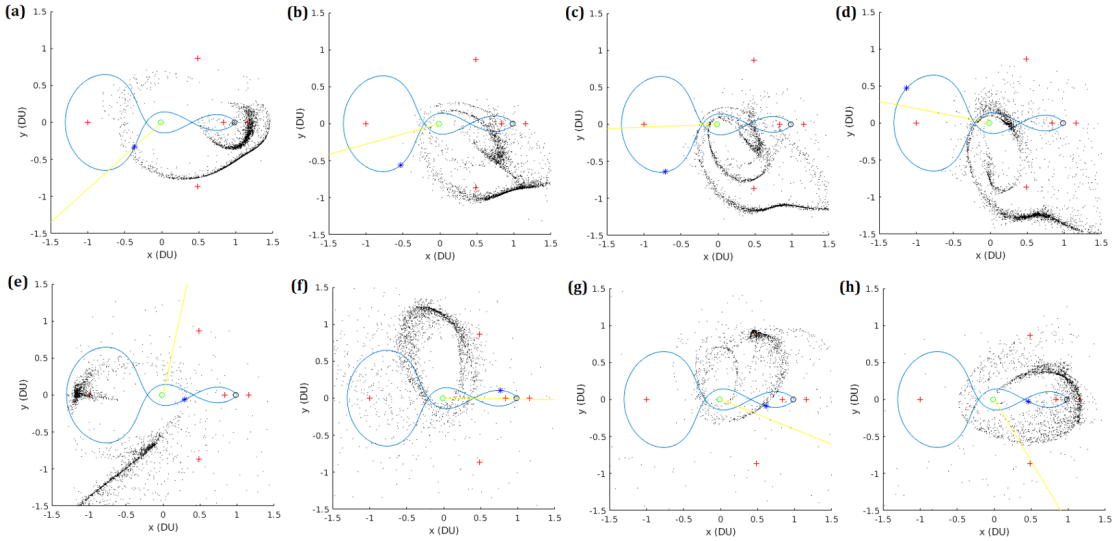

Figure 49: Debris Propagation Snapshot at $\Delta T = 6$ TU Elapsed Time for Debris Orbit 3

Table 36: Total Probability of Hazard for Catastrophic Mishaps in Debris Orbit 3

Run Locations	Run	Mishap Time (Elapsed Days)	Total P_{HZ}
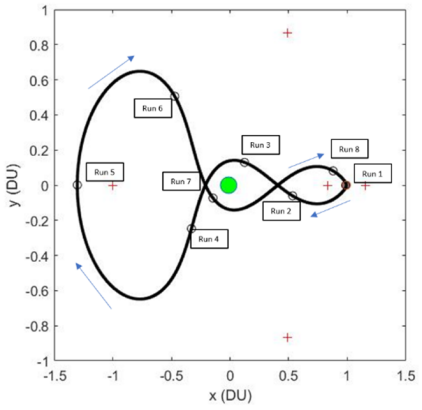	1	**0 TU**	3.22×10^{-10}
	2	**0.5 TU**	2.61×10^{-10}
	3	**0.75 TU**	4.35×10^{-10}
	4	**1 TU**	3×10^{-11}
	5	**2.72 TU**	2.94×10^{-12}
	6	**4.2 TU**	6.24×10^{-12}
	7	**4.6 TU**	4.27×10^{-12}
	8	**5.3 TU**	2.83×10^{-11}

Table 37: Number of Debris Particles at Simulation End for Debris Orbit 3

Run Number	Escaped Earth-Moon System	Impacted Moon	Impacted Earth	End in Lunar SOI	End in Earth SOI	Perigee within GEO
1	**251**	**65**	**87**	**261**	**2198**	**765**
2	**188**	**18**	**0**	**86**	**2564**	**256**
3	**350**	**61**	**1**	**164**	**2349**	**257**
4	**330**	**29**	**0**	**164**	**2572**	**225**
5	**457**	**59**	**10**	**2**	**2438**	**459**
6	**302**	**54**	**6**	**0**	**2402**	**347**
7	**808**	**777**	**65**	**1**	**1471**	**774**
8	**98**	**469**	**53**	**6**	**2198**	**649**

The risks to the notional spacecraft remain small with Debris Orbit 3, however, Debris Orbit 3 simulations did result in some risk to other regions of cislunar space. Orbit 3 resulted in a significant number of both Earth and Moon impacts from the debris particles. In particular, Run 7 resulted in 777 particles impacting the Moon, and 808 particles escaping the Earth-Moon system. This is likely due to the mishap occurring in close proximity to the Earth. At this location, the gravitational effects of the Earth are the strongest, thus leading to large changes in final state (i.e. leaving the Earth-Moon system). Similarly, since the trajectory has a relatively close Earth-pass feature, there is a substantial amount of particles in each run which end with a perigee within GEO. However, it appears the greatest risk of this periodic orbit is to the lunar environment, in particular with impacts to the Moon.

With regards to geometry, the debris particles in Runs 1, 2, 3, and 4 initially appear to have a highly elliptical rotating orbit about the Earth. However, the apogee of this pseudo-elliptical orbit is past the Moon, thus this shape quickly diminished once the rotation of the orbit "crashes" into the Moon causing debris particles to scatter. In Runs 5, 6, and 7 the debris particles stay fairly compact along the trajectory until the section of the orbit which has a close proximity pass of the Moon. Similar to Runs 1, 2, 3, and 4, at this location the debris particles scatter leaving a slight resemblance of a rotating elliptical orbit as the scenario continues. Run 8 is unique in that the

debris particles scatter almost instantly due to the close proximity of the Moon at the time of mishap. Once scattered, the particles appear to collect into a more scattered form of the rotating elliptical orbit which is seen in other cases. There is significant motion in the z-direction when particles pass the Moon, especially in Run 8, where the explosion occurs just prior to the Moon.

Across all 8 runs of Debris Orbit 3, the average relative speed of the debris particles (with respect to the notional spacecraft) contained in the danger zone was 1643 m/s. This was the second highest of all of the orbits analyzed in this work. The large relative speed is attributed to the short period which contains frequent close encounters with both gravitational bodies, thus more instances in the trajectory where large speeds are reached.

As with Debris Orbits 2 and 3, Debris Orbit 4 was also presented in the work of Arenstorf [25, 26] in the 1960's. Results of this orbit are shown below:

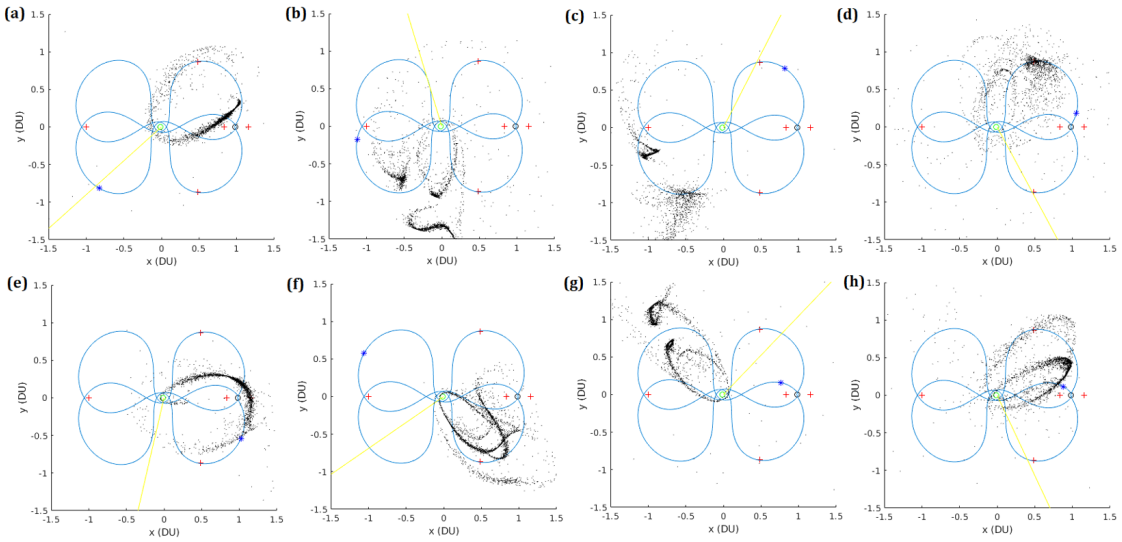

Figure 50: Debris Propagation Snapshot at $\Delta T = 6$ TU Elapsed Time for Debris Orbit 4

Table 38: Total Probability of Hazard for Catastrophic Mishaps in Debris Orbit 4

Run Locations	Run	Mishap Time (Elapsed Days)	Total P_{HZ}
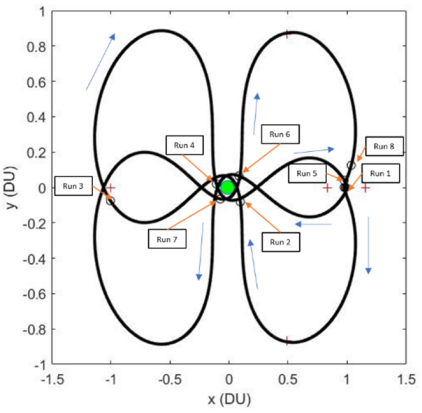	1	0 TU	2.75×10^{-11}
	2	2.17 TU	8.59×10^{-12}
	3	3 TU	1.0×10^{-11}
	4	5.35 TU	5.6×10^{-12}
	5	6.13 TU	6.35×10^{-12}
	6	6.93 TU	1.97×10^{-11}
	7	10.105 TU	4.61×10^{-12}
	8	12.2 TU	8.18×10^{-11}

Table 39: Number of Debris Particles at Simulation End for Debris Orbit 4

Run Number	Escaped Earth-Moon System	Impacted Moon	Impacted Earth	End in Lunar SOI	End in Earth SOI	Perigee within GEO
1	216	191	321	3	1931	1074
2	320	49	89	0	2219	1401
3	559	386	111	6	2122	1260
4	416	300	243	0	1704	1162
5	73	106	391	52	2304	1472
6	253	60	74	510	2037	1432
7	318	93	160	0	2351	1656
8	73	180	332	0	2318	1175

Although the risks to the notional spacecraft are again small, the Debris Orbit 4 simulations resulted in some risk to other regions of cislunar space. Debris Orbit 4 simulations resulted in a greater risks to spacecraft near Earth than any other periodic orbit simulated. In each run, over 1,000 particles ended the simulation with perigees within GEO altitude. In addition, many of the simulation runs saw hundreds of particles pass close enough to the Earth to enter the atmosphere. These particles would pose small risks to spacecraft at all orbital altitudes around Earth.

Another potential concern could be the close approaches to the Moon. The debris cloud passes the Moon about once per month, and it undergoes dramatic changes to

its orbit with each pass. Run 6, which ends near the time when the debris cloud is passing the Moon, resulted in over 500 particles within the lunar SOI at the end of the simulation, which could lead to a small risk to lunar spacecraft. The significant number of particles that impact the Moon could also threaten to contaminate the lunar environment.

In terms of geometry, the debris cloud in Runs 1 and 3 appears to follow the original trajectory, while in Runs 2, 4, 6, 7, and 8 the particles appear to follow their own rotating elliptical orbit about the Earth. Run 5 appears to be a hybrid, having instances throughout the scenario when it appears to be following the trajectory and other instances when it appears in its own rotating elliptical orbit. In all runs, each time the debris particle cloud passes the Moon, many particles are given significant velocity in the z-direction and enter orbits that are out of the Earth-Moon plane.

Debris Orbit 4 had the highest average relative speed of the debris particles (with respect to the notional spacecraft) contained in the danger zone, with an average speed of 2,864 m/s across all 8 runs. This is due to Orbit 5 having the closest and most frequent near-planetary body passes. Many of the runs also had the mishap occur near a gravitational body, causing the debris to scatter at critical nodes in the orbit, thus disrupting its state and changing its condition in a significant manner.

The last orbit analyzed in this work was presented more recently in work conducted by Vaquero and Howell [78, 79]. Results for Debris Orbit 5 are shown below:

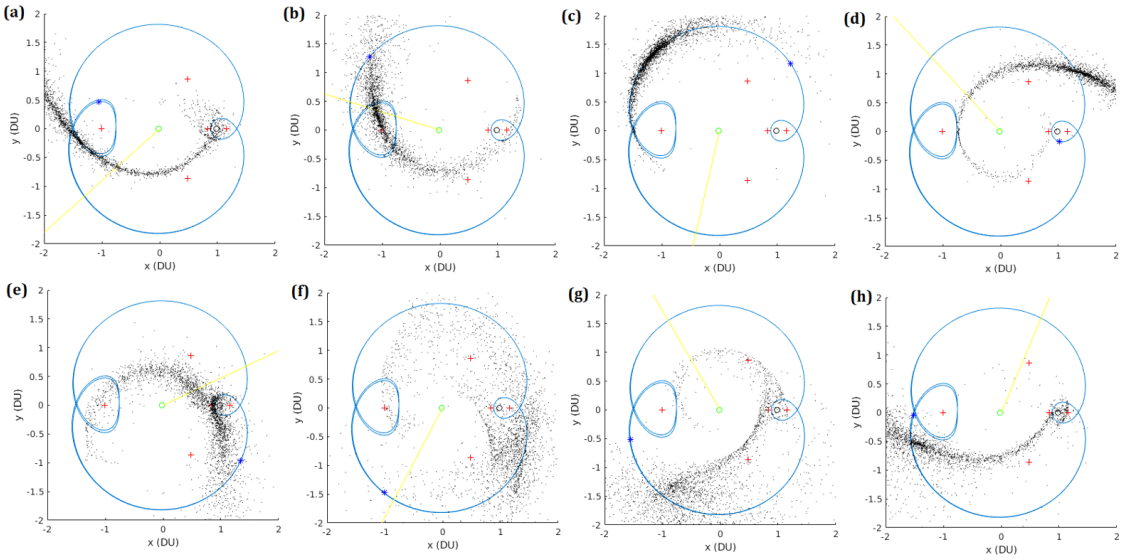

Figure 51: Debris Propagation Snapshot at $\Delta T = 6$ TU Elapsed Time for Debris Orbit 5

Table 40: Total Probability of Hazard for Catastrophic Mishaps in Debris Orbit 5

Run Locations	Run	Mishap Time (Elapsed Days)	Total P_{HZ}
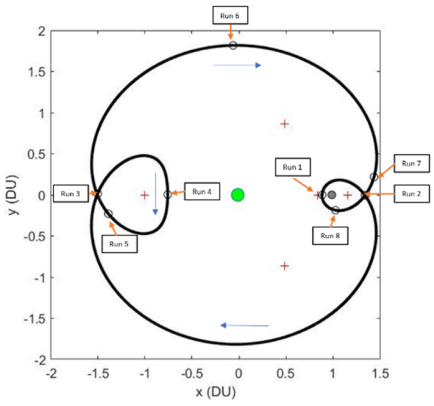	1	0 TU	2.752×10^{-11}
	2	1.12 TU	8.586×10^{-12}
	3	6.13 TU	1.004×10^{-11}
	4	8.47 TU	5.604×10^{-12}
	5	10.5 TU	6.353×10^{-12}
	6	13.2 TU	1.966×10^{-11}
	7	15.5 TU	4.609×10^{-12}
	8	16.5 TU	8.175×10^{-11}

Table 41: Number of Debris Particles at Simulation End for Debris Orbit 5

Run Number	Escaped Earth-Moon System	Impacted Moon	Impacted Earth	End in Lunar SOI	End in Earth SOI	Perigee within GEO
1	**590**	**41**	**0**	**109**	**2223**	**97**
2	**131**	**4**	**0**	**9**	**2696**	**4**
3	**181**	**9**	**0**	**17**	**2577**	**8**
4	**536**	**22**	**0**	**29**	**2287**	**8**
5	**480**	**30**	**0**	**38**	**2589**	**7**
6	**607**	**78**	**0**	**20**	**2045**	**17**
7	**404**	**72**	**0**	**8**	**2399**	**5**
8	**513**	**22**	**0**	**44**	**2395**	**3**

The low speed and long period of Debris Orbit 5 means that the debris cloud does not have time to reach the notional spacecraft by the end of the 50-day simulation. The risk to the notional spacecraft is very low as a result. There is also minimal risk to spacecraft near Earth due to the high altitude of this periodic orbit trajectory, with few particles passing within GEO altitude. Perhaps the greatest risk from this periodic orbit is to the lunar environment. The orbit appears to have an energy level close enough to the energy level of lunar orbits that some particles can enter unstable lunar orbits. This is especially apparent in Run 1, and it is also apparent to a lesser extent in Run 8. After the explosion near the Moon, a ring of particles forms around the Moon. The orbits of these particles are unstable, and many particles are ejected from lunar orbit as the simulation progresses, but many have not left lunar orbit by the time the 50-day simulation concludes. This may create some long-term concern to spacecraft in lunar orbit.

The geometry of the debris cloud for Debris Orbit 5 in all runs stayed compact for the longest amount of time when compared to all orbits analyzed in this work. In most instances the cloud is simply stretched, resembling a snake as the approximate centroid of the cloud follows the original trajectory. This is due to a combination of no near-Earth passes and the long period throughout most of which the particle cloud is far away from any gravitational body. Once the cloud of debris passes the

Moon, the particles scatter all across cislunar space, still rotating about the Earth in the same clockwise direction.

Debris Orbit 5 had the lowest average relative speed of debris with respect to the notional satellite across all 8 runs, with an average relative speed of 504 m/s. The long period of this orbit and its large distance from other gravitational bodies means that the particles move relatively slowly with respect to the notional spacecraft.

6.4.2 Mass and Velocity-Dependent Results

Later in this research, a new model was created by Boone which takes into account both the debris mass and velocity in determining probability of kill. Four discovered cislunar periodic orbits were subject to this new model while the IBEX trajectory was carried over and analyzed to compare the results between models. For each cislunar periodic orbit, catastrophic spacecraft mishaps are simulated for 8 runs. Each run simulated the mishap at different initial starting locations, with debris particle trajectories propagated 4π TU (54.57 days) from the time of the mishap. A notional spacecraft is located at a phase offset (one run ahead) from each mishap location and the survivability model is applied to assess the total probability of hazard to this spacecraft due to collisions with space debris. In addition, the risks to spacecraft near Earth and elsewhere in cislunar space are evaluated based on the number of particles that feature a perigee that is within GEO altitude or orbit within either the lunar or Earth sphere of influence (SOI) at the end of each simulation.

Figures 52-57 show debris propagation snapshots at 6 TU elapsed time for all 8 simulation runs across each of the five cislunar periodic orbits. Subplots (a) through (h) corresponding to Runs 1 through 8, respectively. The green circle marks the location of the Earth, the black circle marks the location of the Moon, and the red crosses mark the locations of the Lagrange points. The yellow line indicates the

current direction to the Sun, the blue star (*) indicates the location of the non-mishap spacecraft, and the black dots represent debris particles. Due to the three-dimensional geometry of the IBEX orbit, there are additional debris propagation snapshots showing the z-direction in Fig. 53 for 1, 3, 6, and 9 TU elapsed time. For the IBEX and Debris Orbits 6-9, the starting locations of each run, along with the mishap time (in Time Units), and the corresponding total probability of hazard to the nearby spacecraft are shown in Tables 42, 44, 46, 48, and 50 respectively. The locations of all particles in the Earth-Moon system at the end of each run are given in Tables 43, 45, 47, 49, and 51 for the IBEX and Debris Orbits 6-9, respectively.

The IBEX was again analyzed using this new model. The results are shown below:

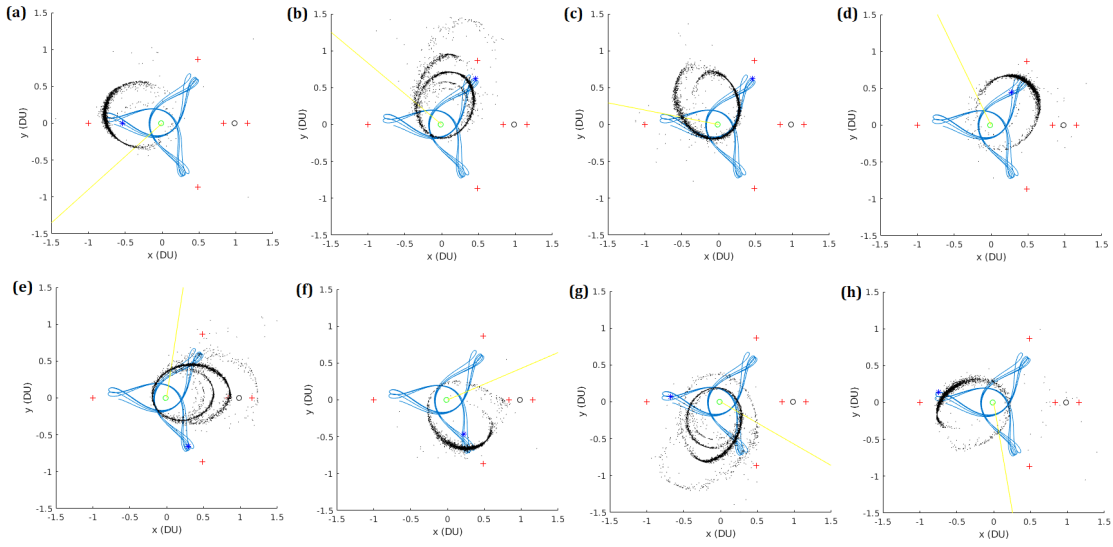

Figure 52: Debris Propagation Snapshot at $\Delta T = 6$ TU Elapsed Time for IBEX

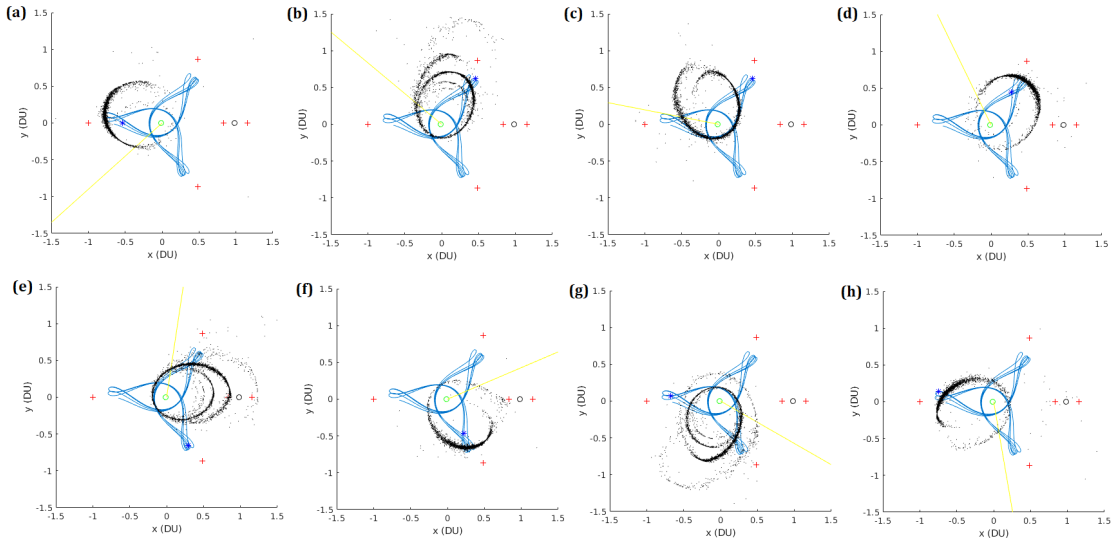

Figure 53: Three-Dimensional Debris Propagation Snapshot at $\Delta T = 1, 3, 6, 9$ TU Elapsed Time for IBEX (Run 3)

Table 42: Total Probability of Hazard to Notional Spacecraft for Catastrophic Mishaps in IBEX

Run Locations	Run	Mishap Time (Elapsed Days)	Total P_{HZ}
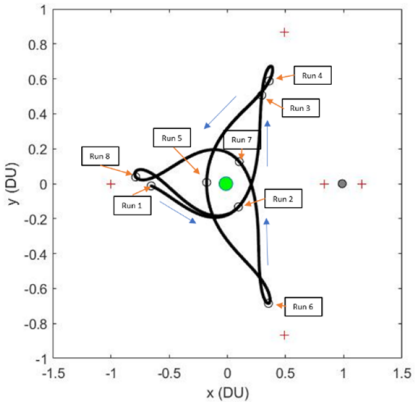	1	0	3.25×10^{-10} %
	2	2.39	8.70×10^{-10} %
	3	4.34	5.55×10^{-10} %
	4	8.68	3.41×10^{-10} %
	5	11.51	5.46×10^{-10} %
	6	16.28	3.77×10^{-10} %
	7	20.63	3.90×10^{-10} %
	8	24.75	1.03×10^{-9} %

Table 43: Number of Debris Particles at Simulation End for IBEX

Run Number	Escaped Earth-Moon System	Impacted Moon	Impacted Earth	End in Lunar SOI	End in Earth SOI	Perigee within GEO
1	**3**	**0**	**0**	**0**	**2859**	**16**
2	**25**	**0**	**0**	**0**	**2831**	**0**
3	**1**	**2**	**0**	**3**	**2919**	**22**
4	**2**	**0**	**1**	**0**	**3092**	**37**
5	**22**	**0**	**0**	**17**	**2927**	**94**
6	**0**	**0**	**3**	**1**	**2760**	**19**
7	**28**	**0**	**0**	**0**	**3094**	**36**
8	**2**	**0**	**0**	**0**	**2822**	**38**

For all mishap location runs of the IBEX, there is minimal risk of either an Earth or lunar impact, with the vast majority of particles remained on the same IBEX-shaped trajectory after mishap occurred. This is likely due to the great distance between the trajectory and Moon, coupled with the absence of near-Earth passes. With the debris field remaining primarily along the orbital path, the most observed of all the orbits analyzed herein, the IBEX features the highest risk to the notional spacecraft with an average P_{HZ} of $5.54 \times 10^{-10}\%$. In terms of geometry, the debris after all runs for the IBEX formed the appearance of a rotating elliptical orbit about the Earth. Across all 8 runs of the IBEX, the average relative speed of the debris particles (with respect to the notional spacecraft) contained in the danger zone was 876 m/s.

The next orbit, Debris Orbit 6, studied features a close transit of the L_2 point, and the effectiveness of this orbit for monitoring spacecraft in L_1/L_2 Lyapunove and halo orbits was presented previously in Chapter IV. Results for this orbit are shown below:

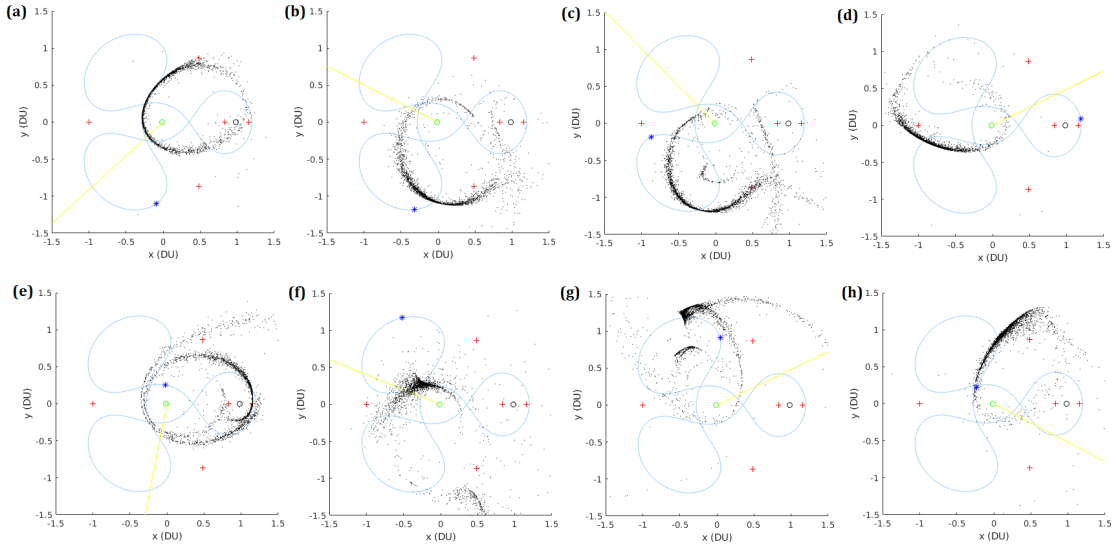

Figure 54: Debris Propagation Snapshot at $\Delta T = 6$ TU Elapsed Time for Debris Orbit 6

Table 44: Total Probability of Hazard to Notional Spacecraft for Catastrophic Mishaps in Debris Orbit 6

Run Locations	Run	Mishap Time (Elapsed Days)	Total P_{HZ}
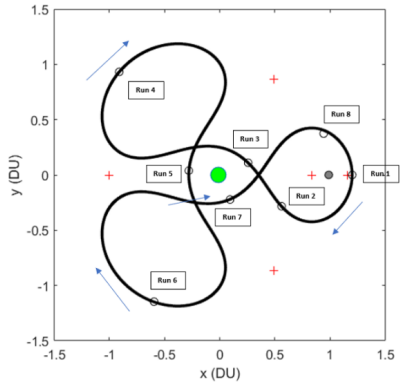	1	0	1.18×10^{-12} %
	2	5.65	1.07×10^{-10} %
	3	7.17	1.26×10^{-11} %
	4	16.07	3.70×10^{-12} %
	5	26.49	1.64×10^{-11} %
	6	34.74	1.49×10^{-12} %
	7	45.60	1.60×10^{-11} %
	8	49.94	5.63×10^{-11} %

Table 45: Number of Debris Particles at Simulation End for Debris Orbit 6

Run Number	Escaped Earth-Moon System	Impacted Moon	Impacted Earth	End in Lunar SOI	End in Earth SOI	Perigee within GEO
1	**6**	**6**	**1**	**515**	**2134**	**33**
2	**74**	**24**	**0**	**3**	**2576**	**84**
3	**258**	**61**	**0**	**7**	**2858**	**99**
4	**101**	**31**	**3**	**0**	**2528**	**96**
5	**295**	**73**	**0**	**44**	**2514**	**113**
6	**107**	**20**	**2**	**0**	**2805**	**29**
7	**178**	**59**	**1**	**0**	**2684**	**112**
8	**19**	**37**	**0**	**406**	**2441**	**71**

The risks to the notional spacecraft remain extremely small in Orbit 6. When compared to the IBEX, there are significantly more lunar impacts with number of particles that impacted the Moon is fairly comparable across all runs in Orbit 6. This is to be expected since the trajectory encapsulates the Moon, with a close proximity pass of the L_2 Lagrange point. Overall, the risk of an Earth impact is low, and there were a maximum of three particles on a trajectory that intersected the Earth the Earth in Run 4. It is expected that these particles would be so small that they would burn up upon reentry. The vast majority of debris particles had an end state which was orbiting the Earth above GEO.

In terms of the geometry of the particle cloud, the debris particles in Runs 2, 3, and 8 begin to form a rotating elliptical orbit about the Earth. However, the apogee of this pseudo-elliptical orbit is past the Moon, and intersecting the Moon causes the debris particles to scatter. While somewhat dispersed, the overall elliptical shape remains intact. In Runs 4 and 5, the particles scatter in all directions, thus highlighting the chaotic nature of the system. The debris particles in Runs 6 and 7 scatter immediately due to their close initial proximity to the Moon. Across Runs 2-8 (since Run 1 posed no risk to the notional spacecraft), the average relative speed of debris in the danger zone with respect to the notional spacecraft was 1171 m/s. This represents the second highest relative speed of all of the orbits analyzed, which may

be due to the relatively short period combined with close- to mid- range Earth/Moon passes.

Like Debris Orbit 6, Debris Orbit 7 was previously analyzed for it's effectiveness in variouus SDA mission architectures in Chapter IV. Results for Debris Orbit 7 are shown below:

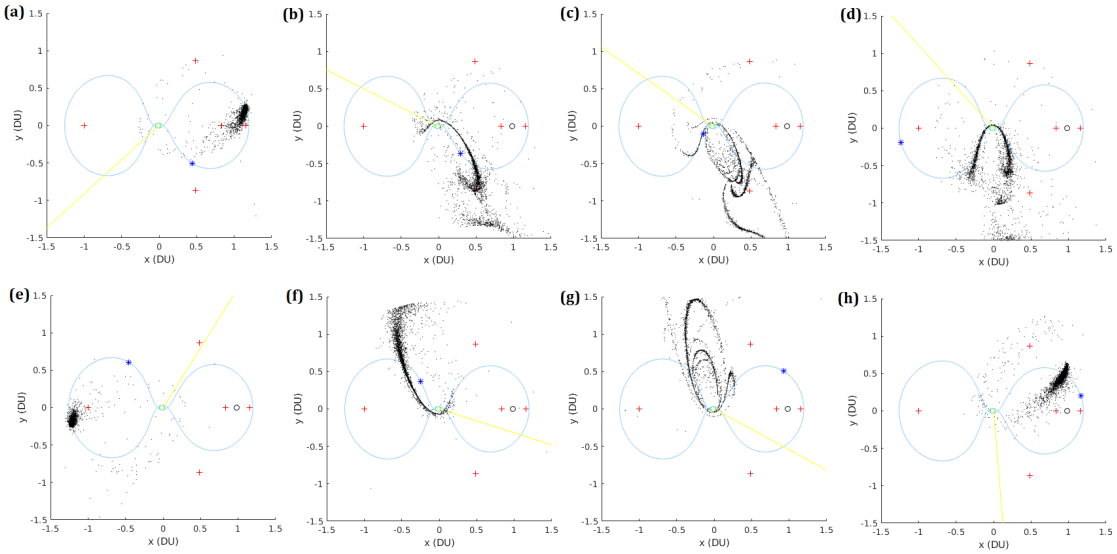

Figure 55: Debris Propagation Snapshot at $\Delta T = 6$ TU Elapsed Time for Debris Orbit 7

Table 46: Total Probability of Hazard to Notional Spacecraft for Catastrophic Mishaps in Debris Orbit 7

Run Locations	Run	Mishap Time (Elapsed Days)	Total P_{HZ}
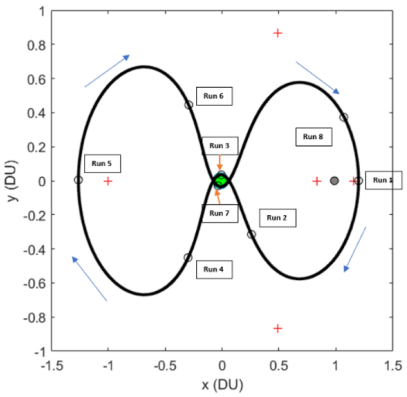	1	0	0 %
	2	5.65	4.08×10^{-10} %
	3	6.34	3.54×10^{-10} %
	4	7.38	3.30×10^{-12} %
	5	13.46	7.86×10^{-14} %
	6	19.54	2.24×10^{-10} %
	7	20.54	3.04×10^{-11} %
	8	25.19	4.34×10^{-10} %

Table 47: Number of Debris Particles at Simulation End for Debris Orbit 7

Run Number	Escaped Earth-Moon System	Impacted Moon	Impacted Earth	End in Lunar SOI	End in Earth SOI	Perigee within GEO
1	6	2	223	75	2864	2550
2	81	26	164	1	2328	2069
3	494	190	174	0	2055	2309
4	78	21	173	0	2661	2360
5	4	1	148	0	2763	2615
6	46	14	108	0	2911	2062
7	492	64	219	0	2137	2256
8	32	11	174	122	2628	2594

The risks to the notional spacecraft remain small for Debris Orbit 7, with Run 1 featuring zero risk. This means that there were no particles that entered the notional spacecraft's danger zone. However, the Debris Orbit 7 simulations did result in some risk to other regions of cislunar space. There were a significant number of both Earth and Moon impacts, and many of the simulation runs saw hundreds of particles pass close enough to the Earth to enter the atmosphere. The number of Earth impacts was fairly consistent in all runs, ranging from approximately 100 to 230 particles. This is likely due to the close-proximity Earth passes featured in this orbit. Once again, it is expected that these particles would burn up during reentry into Earth's atmosphere due to their physical size and mass, thus causing no appreciable risk to ground-based equipment and/or personnel. However, due to the orbit's close approaches to the Earth, all runs result in approximately 2,000-2,5000 particles maintaining a perigee within GEO. This debris population could pose risks to spacecraft in near-Earth space.

The geometry of the debris particle cloud in Runs 1, 5, and 8 stays densely compact, and most particles remain along the original trajectory for the entire simulation. The debris particles in Runs 2, 3, 6, and 7 initially appear to have a rotating pseudo-elliptical orbit about the Earth. However, as with some Runs in Orbit 6, the apogee of this rotating pseudo-elliptical orbit is past the Moon, thus this shape quickly di-

minishes as the debris particles scatter upon a close approach with the Moon. In Run 4, the debris particles loosely follow along the original trajectory's path for the entire simulation. Across all 8 runs of Debris Orbit 7, the average relative speed of debris in the danger zone with respect to the notional spacecraft was 1384 m/s. This was the highest of all of the orbits analyzed in this study. The large relative speed is attributed to the short period which contains frequent close encounters with the Earth, thus leading to more instances in the trajectory where large speeds are reached.

The next orbit analyzed is Debris Orbit 8. The results of Debris Orbit 8 simulations are shown below:

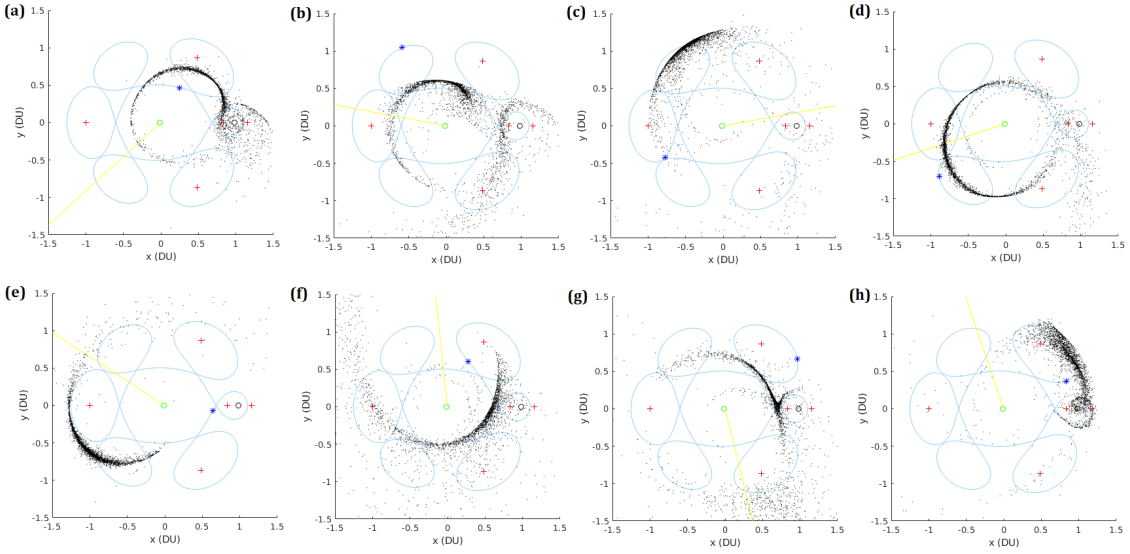

Figure 56: Debris Propagation Snapshot at $\Delta T = 6$ TU Elapsed Time for Debris Orbit 8

Table 48: Total Probability of Hazard to Notional Spacecraft for Catastrophic Mishaps in Debris Orbit 8

Run Locations	Run	Mishap Time (Elapsed Days)	Total P_{HZ}
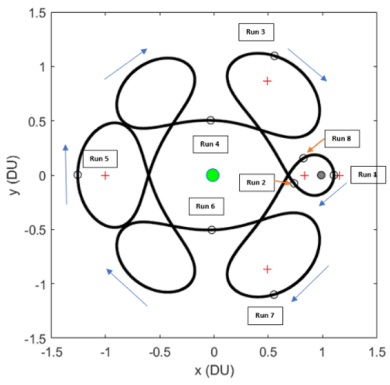	1	0	6.18×10^{-11} %
	2	4.34	6.05×10^{-12} %
	3	17.37	6.45×10^{-12} %
	4	31.48	1.02×10^{-10} %
	5	65.14	8.96×10^{-12} %
	6	98.79	1.61×10^{-11} %
	7	112.90	7.08×10^{-12} %
	8	126.80	4.11×10^{-11} %

Table 49: Number of Debris Particles at Simulation End for Debris Orbit 8

Run Number	Escaped Earth-Moon System	Impacted Moon	Impacted Earth	End in Lunar SOI	End in Earth SOI	Perigee within GEO
1	97	88	3	106	2619	216
2	127	33	0	2	2771	108
3	54	23	1	3	2835	64
4	95	48	0	0	2936	8
5	68	21	0	7	2816	43
6	438	92	0	45	2392	13
7	313	70	0	1	2534	46
8	157	56	0	45	2547	14

As with the previous orbits, the risk to the notional spacecraft remains small with Debris Orbit 8. There is also minimal risk to spacecraft near Earth due to the high altitude of this periodic orbit trajectory, with few particles passing within GEO altitude. Runs 1 and 3 were the only ones to have debris particles impact the Earth. However, it was only a small amount in both cases. Perhaps the greatest risk from this periodic orbit is to the lunar environment. All runs saw a consistent number of debris particles impacting the Moon, ranging from approximately 20 to 90. The majority of particles across all runs ended in an Earth orbit outside of GEO. However,

the trajectory path does have close passes and/or encapsulates many Lagrange points, which could create concern for satellites orbiting these points.

In terms of debris particle geometry, Runs 1, 2, 3, 5, 6, 7, and 8 featured the debris loosely scattering across the whole system with there being a slightly more dense collection centered on the trajectory path. Run 4 formed a rotating circular orbit about the Earth. However, as with certain runs in Debris Orbits 6 and 7, the apogee of this pseudo-elliptical orbit is past the Moon, thus this shape quickly dissipates once the rotation of the orbit intersects the Moon and the debris particles scatter.

Across all 8 runs of Debris Orbit 8, the average relative speed of debris in the danger zone with respect to the notional spacecraft was 561 m/s. This was the lowest of all of the orbits analyzed in this work and is attributed to the long period and large distance from the Earth (compared to the other orbits analyzed).

Similar to Debris Orbits 6 and 7, Debris Orbit 9 was also recently discovered and presented for SDA analysis in Chapter IV. The results of Debris Orbit 9 simulations are shown below:

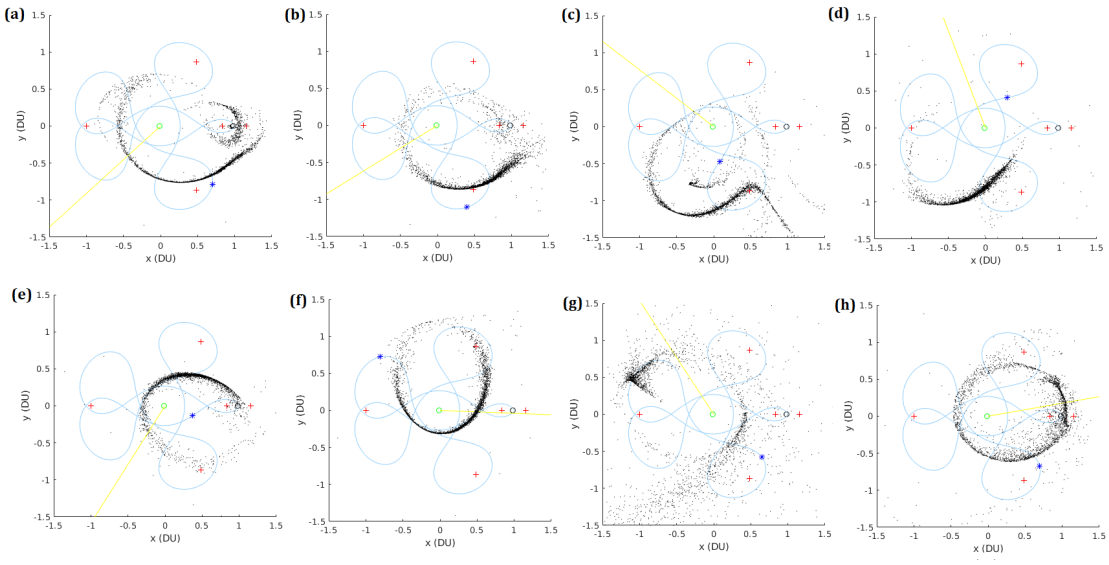

Figure 57: Debris Propagation Snapshot at $\Delta T = 6$ TU Elapsed Time for Debris Orbit 9

Table 50: Total Probability of Hazard to Notional Spacecraft for Catastrophic Mishaps in Debris Orbit 9

Run Locations	Run	Mishap Time (Elapsed Days)	Total P_{HZ}
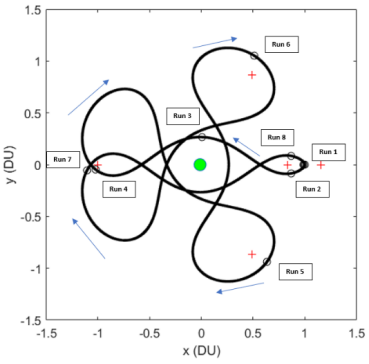	1	0	1.07×10^{-9} %
	2	0.87	2.16×10^{-11} %
	3	4.34	5.50×10^{-11} %
	4	9.12	7.71×10^{-12} %
	5	28.23	4.56×10^{-11} %
	6	47.77	6.68×10^{-11} %
	7	67.09	9.44×10^{-13} %
	8	76.36	5.96×10^{-11} %

Table 51: Number of Debris Particles at Simulation End for Debris Orbit 9

Run Number	Escaped Earth-Moon System	Impacted Moon	Impacted Earth	End in Lunar SOI	End in Earth SOI	Perigee within GEO
1	111	113	42	67	2701	130
2	63	32	0	49	2807	63
3	236	132	0	25	2501	73
4	53	16	2	1	2560	28
5	17	71	0	0	2663	81
6	295	31	1	110	2552	160
7	348	56	11	3	2436	43
8	91	198	4	245	2371	191

As with all other orbits analyzed, the risk to the notional spacecraft remain small in Debris Orbit 9. Risk to the Earth and Earth-orbiting satellites is low, with many runs featuring no Earth impacts.The number of debris particles which end with a perigee within GEO remains below 200 across all runs. Similar to Orbit 8, the greatest risk from a mishap in Debris Orbit 9 appears to be to the lunar environment. Debris Orbit 9 has the most lunar impacts than any other orbit analyzed. This is expected due to the close proximity lunar pass with which this orbit features. Dramatic changes occur in the debris particles motion with every close proximity pass of the Moon, leading to concerns as the scenario propagates for longer periods of time. Close proximity Lagrange point passes is another aspect of this orbit, thus increasing risk to satellites orbiting about the L_1, L_3, L_4, and L_5 Lagrange points.

The debris cloud in Runs 1, 2, 3, and 8 forms a rotating psuedo-elliptical orbit about the Earth. However, as with certain runs in Debris Orbits 6, 7 and 8, the apogee of this pseudo-elliptical orbit is past the Moon, so the debris particles scatter when they encounter the Moon. Run 4 had a dense cluster of debris particles which followed the trajectory path. The debris clouds in Runs 5, 6, and 7 appear to follow the original trajectory with the particles forming a dense cluster until they reached the Moon, which led to the cluster being dispersed. Across all 8 runs of Orbit 9, the average relative speed of debris in the danger zone with respect to the notional

spacecraft was 687 m/s, the second lowest of the periodic orbits analyzed.

6.5 Summary

This chapter sought to analyze the debris-related consequences of a catastrophic spacecraft mishap occurring along cislunar periodic orbits. Specifically, two vulnerability models (one which was dependent on mass and the other which was dependent on mass and velocity) were applied to five cislunar periodic orbits each. Each model consisted of simulating eight mishap scenarios at various critical nodes of each orbit. The IBEX orbit was used across both vulnerability models to compare any differences in results and show the impact of debris velocity on the probability of kill to the notional spacecraft. For both models, the results were extremely similar, leading to the conclusion that adding velocity to the vulnerability model minimally impacts the probability of kill. The mishap scenarios seen in this study could occur during SDA missions comprising two or more notional spacecraft, with one spacecraft suffering the mishap, and the other imperiled by the resulting debris cloud during the duration of each simulation. Particular points of interest in this investigation included the Earth, Moon, and notional spacecraft. While there were anticipated risks to other useful regions of cislunar space, such as the Lagrange points, the true magnitude of these risks remains unknown. In this study, the IBEX (Debris Orbit 1) featured the highest risk to other spacecraft, granted this risk was extremely low. It did, however, have the lowest risk of collision with spacecraft in Earth or lunar orbit, the lowest risk of impacting either the Earth or Moon, and the lowest number of debris particles escape the Earth-Moon system. Conversely, Debris Orbits 4 and 7 featured the high risk of collision with the Earth. However, it is expected this debris would burn up in the Earth's atmosphere upon entry. Debris along Orbits 2, 3, 4, 7, 8, and 9 all featured moderate to high risk of a Moon collision. Debris Orbits 2, 3, 4, 5, 6, 7, 8,

and 9 all had a moderate to large amount of debris which escaped the Earth-Moon system.

Each case study threatens unique regions of cislunar space; however, the overall risk to the notional spacecraft was very low in each case. Thus, SDA missions are likely to be minimally affected if a nearby satellite in a cislunar periodic orbit undergoes a breakup event. This is largely due to the wide expanse of cislunar space. When compared to LEO, which is heavily congested with space objects, cislunar space is larger and has fewer space objects. However, impacts with the Moon, or intersections with congested orbits near Earth, would remain a concern. The location of the mishap along the periodic orbit has a significant impact on the severity, especially with respect to collisions with gravitational bodies. Periodic orbits with initial trajectories that featured close approaches to the Earth or Moon had the greatest probability of collision with one of these bodies.

Future studies of cislunar debris propagation and survivability assessment could analyze other case study scenarios, such as catastrophic mishaps within larger SDA constellations (i.e., more spacecraft in a given periodic orbit), or catastrophic mishaps within SDA constellations featuring two or more cislunar periodic orbit types. In addition, while the dynamical model in the present research incorporated four-body assumptions for trajectory propagation, future research could incorporate an ephemeris-based gravitational model to propagate debris orbits within the lunar SOI and estimate the hazard to spacecraft in lunar orbit to such debris. Finally, extending the simulation time could yield insight into long-term debris propagation behavior and spacecraft risk within the Earth-Moon system. For longer simulations, debris would likely only travel along the periodic orbit for a maximum of one or two periods after the mishap due to the chaotic nature of the BCR4BP.

VII. Conclusions and Recommendations

7.1 Conclusions of Research

In the early years of spaceflight, space operations primarily consisted of near-Earth missions with few spacecraft ever venturing to the Moon. As time progressed, more and more missions began extending beyond the confines of geosynchronous orbit. This pattern continues to today, with the contemporary space domain facing increasing concerted efforts around the world to reach and operate within the cislunar environment. The future will likely see a similar trend of extending outward to the new high-grounds with missions becoming more and more frequent near the Moon and beyond. With various countries now looking to expand their infrastructure in space, safe cislunar space traffic management techniques coupled with the development of new policy and terminology which embrace the entirety of the Earth-Moon system and its celestial environs are vital for the continued protection of space assets.

This research included an in-depth analysis of cislunar periodic orbits. In particular, the dynamics, construction, effectiveness in space domain awareness (SDA) missions, and debris risks from an onboard explosion were recorded. Over 30 cislunar periodic orbits were discovered in this work and presented in Figs. 12, 13, 18, 19 (Orbits 7-9), and 36. These orbits may be used for a wide swath of missions, not limited to SDA. Such missions include re-supply, personnel transport, and space-based infrastructure development. Orbits which feature close proximity passes of both the Earth and Moon, identified herein as cycler orbits, may be extremely useful for such mission sets.

The cislunar periodic orbits analyzed in this work are ideal candidates for cislunar SDA mission architectures, such as monitoring L_1/L_2 Lyapunov and halo orbits. This is due to their ability to traverse a wide expanse of cislunar space while capturing

various viewing angles on targets. Chapter IV sought to present and compare the effectiveness of twelve different cislunar periodic orbits, both individually and in combination with one another, when subject to the monitoring of targets in four SDA mission architectures: L_1 Lyapunov orbit surveillance, L_2 Lyapunov orbit surveillance, L_1 halo orbit surveillance, and L_2 halo orbit surveillance. Nine of the twelve orbits analyzed in Chapter IV were generated in the circular restricted three-body problem (CR3BP) with a non-dimensional mass parameter of $\mu = 0.012150584673414$. The other three were obtained from previous literature and corrected to use the same standardized μ value. These orbits were then subject to a simulation in which the visual magnitude was recorded with Sun, Earth, and Moon exclusion angles considered. A cutoff visual magnitude of 18.5 was instituted to determine if a target was observable. While the cislunar periodic orbits analyzed in this work are periodic in the CR3BP, they rapidly become more chaotic with the introduction of additional perturbations, such as the Moon's eccentricity or the Sun's gravitational force. Bicircular restricted four-body problem (BCR4BP) Δe_V analysis was performed to calculate the approximate error in ΔV when transitioning cislunar periodic orbits from the CR3BP to the BCR4BP. The results of this work show cislunar periodic orbits to be highly effective in monitoring Lyapunov and halo orbits about the Earth-Moon L_1 and L_2 Lagrange points.

A new taxonomy for the classification of SDA regions in the Earth-Moon system was introduced which will enable a spatial division of the national SDA mission portfolio. Five SDA regions were presented in this taxonomy: Low-Ground SDA (LG-SDA), Mid-Ground SDA (MG-SDA), High-Ground SDA (HG-SDA), Parapet SDA (P-SDA), and Fence Line SDA (FL-SDA). Particular points in the Earth-Moon system, such as Lagrange points, and regions in which trajectory dynamics become chaotic, such as near the Earth SOI, are markers for regional boundaries. All pro-

posed regions correspond to varying distances away from the Earth and varying SDA mission subsets, to include space traffic management, space control, space weather observation, lunar/Lagrange point surveillance, and planetary defense. Each region is described with a corresponding identification of the associated spatial distance as measured radially from the center of the Earth in terms of kilometers and the canonical unit XGEO, a common unit used by AFRL when describing regions past GEO.

Mishaps in the form of catastrophic spacecraft explosions were simulated along selected cislunar periodic orbits to analyze potential risk to the Earth, Moon, and a notional satellite in the same orbit. Two vulnerability models were used in assessing probability of kill of the notional spacecraft: one which was mass-dependent and one which was mass and velocity dependent with respect to the artificial debris. The Interstellar Boundary Explorer (IBEX) orbit was used in both models to compare them. The vulnerability models showed consistent results, leading to the conclusion that adding velocity to the model minimally impacts the probability of kill. In all debris simulations, risk to the notional satellite in the orbit was low, leading to the conclusion that SDA missions are likely to be minimally affected if a nearby satellite in a cislunar periodic orbit undergoes a breakup event. This is largely due to the wide expanse of cislunar space. However, impacts with the Moon, or intersections with congested orbits near Earth, would remain a concern. The location of the mishap along the cislunar periodic orbit has a significant impact on the severity, especially with respect to collisions with gravitational bodies. Cislunar periodic orbits with trajectories that featured close approaches to the Earth or Moon had the greatest probability of collision with one of these bodies.

In conclusion, the SDA simulations showed cislunar periodic orbits to be extremely effective in monitoring Lyapunov and halo orbits about the L_1 and L_2 Lagrange points. Further analysis into the propellant expenditure (ΔV) is required to ade-

quately determine the feasibility of cislunar periodic orbits in a real world, highly perturbative, environment. However, if the required ΔV is indeed low, cislunar periodic orbits are ideal candidates for SDA and surveillance of various points in cislunar space, to include the Moon and Lagrange points.

7.2 Significance of Research

This research provided one of the first in-depth analysis of cislunar periodic orbits for SDA mission architectures. This understanding will be valuable in creating avenues for advanced space traffic management and monitoring techniques for cislunar objects. It is vital to have a complete understanding and awareness of all space objects in any region of cislunar space. This knowledge optimizes mission readiness while avoiding catastrophic collisions. During this research, over 30 cislunar periodic orbits were also discovered. These new orbits create a wide range of viewing angles for various regions of cislunar space while also featuring close proximity passes to critical points such as the Moon and Lagrange points. Due to this, these orbits may be applied to a wide swath of missions in the Earth-Moon system.

With nations and private companies looking to expand infrastructure into cislunar space and beyond, the techniques which have been used and focused on near-Earth space in the past must be modified. New policy and terminology will undoubtedly be required in the coming decades. The SDA taxonomy presented in this research aims to assist with this effort. This new taxonomy embraces the entirety of the Earth-Moon system and enables a spacial division of the national SDA mission portfolio, with specific regions corresponding to compounding distances from the Earth and varying SDA mission subsets.

This research also provided the first study into debris related consequences should a mishap occur along a cislunar periodic orbit. As orbits in cislunar space become

more crowded, the importance of keeping this region free from hazardous artificial debris will begin to grow. Although the risk to another satellite in the a cislunar periodic orbit which had a mishap occur in is assessed to be low, spacecraft in other orbital regions such as LEO may be at a greater threat.

7.3 Publications and Scholarly Efforts

The following list of publications and scholarly efforts illustrates the impactful nature of this research on the wider community at the time of this thesis submission.

7.3.1 Journal Manuscripts under Review

1. Wilmer, A. P., Bettinger, R. A., "Beyond the High Ground: A Proposed Space Domain Awareness Taxonomy for Earth-Moon System Operations," *Air & Space Power Journal.*

2. Wilmer, A. P., Boone, N. R., Bettinger, R. A., "Debris Propagation and Spacecraft Survivability Assessment for Catastrophic Mishaps Occurring in Cislunar Periodic Orbits," *Journal of Space Safety Engineering.*

7.3.2 Conference Papers

1. Wilmer, A. P., Bettinger R. A., Little B. D., "Cislunar Periodic Orbit Constellation Assessment for Space Domain Awareness of L_1 and L_2 Halo Orbits," *2021 ASCEND Conference*, Las Vegas, NV, November 2021.

2. Wilmer, A. P., Bettinger R. A., Little B. D., "Preliminary Viability Assessment of Cislunar Periodic Orbits for Space Domain Awareness," *2021 Advanced Maui Optical and Space Surveillance Technologies Conference (AMOS)*, Maui, HI, September 2021.

3. Wilmer, A. P., Bettinger R. A., "Lagrangian Derivation and Stability Analysis of Multi-Body Gravitational Dynamical Models with Application to Cislunar Periodic Orbit Propagation," *2021 AAS/AIAA Astrodynamics Specialist Conference*, Big Sky, MT, August 2021.

4. Wilmer, A. P., Boone, N. R., Bettinger, R. A., "Artificial Debris Propagation in Cislunar Periodic Orbits," *2021 AAS/AIAA Astrodynamics Specialist Conference*, Big Sky, MT, August 2021.

7.3.3 Scholarly Presentations

1. Wilmer, A. P., Bettinger R. A., "Preliminary Space Domain Awareness Assessment of Cislunar Periodic Orbits for Lagrange Point Surveillance," *2nd Cislunar Security Conference*, John Hopkins Applied Physics Laboratory, MD, November 2021.

7.4 Recommendations for Future Work

The analysis conducted in the present research may be expanded with follow-on research. Various avenues for future development in this field include:

- Describe how detailed a Target is if it is under the visual magnitude cutoff for being viewable. Questions which should be answered include: Are capabilities of this spacecraft able to be identified? Which country does this spacecraft belong to?

- Research into the difficulty of SDA on cislunar periodic orbits. Essentially, how difficult is orbit determination on cislunar periodic orbits.

- Development of a study which looks into the effectiveness of cislunar periodic orbits in other mission sets such as re-supply, personnel transport, and space-based infrastructure development.
- Increase the number of cislunar periodic orbits analyzed in the SDA model.
- Increase the number of notional satellite in cislunar periodic orbits for the mishap scenarios.
- Discover more cislunar periodic orbits which may aid in future missions.
- Increase the number of notional satellites in cislunar periodic orbits for the mishap scenarios.
- Longer simulations to characterize longevity of debris.

Bibliography

1. Wang Sang Koon, Martin W. Lo, Jerrold E. Marsden, and Shane D. Ross. *Dynamical Systems, The Three-Body Problem, and Space Mission Design*, chapter 2. 3 edition, 2011.

2. Daniel J. Grebow. Generating Periodic Orbits in the Circular Restricted Three-Body Problem With Applications to Lunar South Pole Coverage. Master's thesis, Purdue University, 2006.

3. Nathan R. Boone. Cislunar debris propagation following a catastrophic spacecraft mishap. Master's thesis, Air Force Institute of Technology, 2021.

4. Joseph J. Roth and Eric J. Felt. Overcoming technical challenges from low earth orbit to cislunar. Presented at 2020 AMOS Conference, 2020.

5. Leondard David. Us military eyes strategic value of earth-moon space. `https://www.space.com/us-military-strategic-value-earth-moon-space.html`, 2019.

6. USSF. Spacepower. *Space Capstone Publication*, page 38, 2020.

7. Leonard Meirovitch. *Methods of Analytical Dynamics*. 1 edition, 2003.

8. Mauri Valtonen and Hannu Karttunen. *The Three-Body Problem*. Cambridge University Press, 2006.

9. William E. Wiesel. *Modern Astrodynamics*. CreateSpace, 2 edition, 2010.

10. H. Poincaré. *Les Méthodes Nouvelles de la Mécanique Céleste*. Gauthier-Villars, Paris, 1892-1899.

11. Victor Szebehely. *Theory of Orbits*. Academic Press, 1967.

12. Jeffery S. Parker and Rodney L. Anderson. *Low-Energy Lunar Trajectory Design*. John Wiley Sons Inc., 2014.

13. Andrew Jones. Chang'e-5 successfully lands on moon to collect youngest lunar samples. `https://spacenews.com/change-5-successfully-lands-on-moon-collect-youngest-lunar-samples/`, 2020.

14. Morgan McFall-Johnsen. India's and israel's moon-landing attempts both failed during descent — here's why the '15 minutes of terror' are so difficult. `https://www.businessinsider.com/why-india-israel-failed-moon-landings-failed-final-descent-2019-9`, 2019.

15. Maria Temming. Israel's first moon mission lost moments before landing. `https://www.sciencenews.org/article/israel-moon-mission-spacecraft-crash`, 2019.

16. Su-Shu Huang. *Very Restricted Four-Body Problem*. National Aeronautics and Space Administration, 1960.

17. STK. Orbit propagators for satellites, 2016.

18. G. H. Darwin. Periodic orbits. *Acta Mathematica*, pages 99–242, 1897.

19. G. W. Hill. Researches in the lunar theory. *American Journal of Mathematics*, pages 5–26, 1878.

20. S. S. Hough. On certain discontinuities connected with periodic orbits. *Acta Mathematica*, 21, 1901.

21. George Darwin. On certain families of periodic orbits. *Royal Astronomical Society*, pages 108–143, 1909.

22. Ellis Strömgren. Symmetrische und unsymmetrische librationsähnliche bahnen im probléme restreint mit asymptotisch-peridischen bahnen als grenzbahnen. 1934.

23. V. A. Egorov. Certain problems of moon flight dynamics. *The Russian Literature of Satellites*, pages 107–174, 1958.

24. Robert R. Newton. Periodic orbits of a planetoid passing close to two gravitating masses. *Smithsonian Contributions to Astrophysics*, 3(7), 1959.

25. Richard F. Arenstorf. Existence of periodic solutions passing near both masses of the restricted three-body problem. *AIAA Journal*, 1:238–240, 1963.

26. Richard F. Arenstorf. Periodic trajectories passing near both masses of the restricted three-body problem. *Proceedings of the XIV International Astronautical Congress*, pages 85–97, 1963.

27. Anthony L. Genova and Buzz Aldrin. A free-return earth-moon cycler orbit for an interplanetary cruise ship. *Astrodynamics Speacialist Conference*, 2015.

28. K. E. Papadakis. Families of asymmetric periodic orbits in the restricted three-body problem. *Earth, Moon, and Planets*, pages 25–42, 2008.

29. Robert Farquhar. The control and used of libration-point satellites. Master's thesis, Stanford University, 1968.

30. USDOD. National security space strategy. *Space Capstone Publication*, page 1, 2011.

31. Benjamin S. Lambeth. Mastering the ultimate high ground: Next steps in the military uses of space. *Rand*, page 23, 2003.

32. Paul Cefola Brian Weeden and Jaganath Sankaran. Global space situational awareness sensors. *Presented at the Advanced Maui Optical and Space Surveillance Technologies Conference*, 2010.

33. Mark A. Baird. Maintaining space situational awareness and taking it to the next level. *Air and Space Power Journal*, 27, 2013.

34. Sandra Erwin. Air force: Ssa is no more; it's 'space domain awareness'. *Spacenews*, 2019.

35. Eva Dou. China and russia to open moon base, expanding space cooperation. *The Washington Post*, page 10, 2021.

36. Adam Mann. China's chang'e-5 lunar mission: Sampling the lunar surface. *Space.com*, 2020.

37. Theresa Hitchens. Dod needs plans to protect commercial space industry, says new study. *breakingdefense.com*, 2020.

38. Joseph J. Roth and Eric J. Felt. Overcoming technical challenges from low earth orbit to cislunar. *Presented at the Advanced Maui Optical and Space Surveillance Technologies Conference*, 2020.

39. IAA. Cosmic study on space traffic management. *International Academy of Astronautics (IAA) Report*, page 11, 2006.

40. John R. Davidson and Paul E. Sandorff. Environmental problems of space flight structures: Ii. meteoroid hazard. 1963.

41. Paige B. Burbank, Burton G. Cour-Palais, and William E. McAllum. A meteoroid environment for near-earth, cislunar, and near-lunar operations. 1965.

42. Judit Slíz-Balogh, András Barta, and Gábor Horváth. Celestial mechanics and polarization optics of the kordylewski dust cloud in the earth-moon lagrange point l5, part i: 3d celestial mechanical modelling of dust cloud formation. *Monthly Notices of the Royal Astronautical Society*, 480(4):5550–5559, 2018.

43. Nathan R. Boone and Robert A. Bettinger. Spacecraft survivability in the natural debris environment near the stable earth-moon lagrange points. *Advances in Space Research*, 67(8):2319–2332, 2021.

44. Donald J. Kessler and Burton G. Cour-Palais. Collision frequency of artificial satellites: the creation of a debris belt. *Journal of Geophysical Research*, 83 (A6):2637–2646, 1978.

45. Nathan R. Boone and Robert A. Bettinger. Cislunar debris propagation following a catastrophic spacecraft mishap. *2021 AIAA SciTech Forum.*

46. Nathan R. Boone and Robert A. Bettinger. Debris propagation following a catastrophic spacecraft mishap at the collinear earth-moon lagrange points. 2021.

47. Priyankar Bandyopadhyay, Ram Krishan Sharma, and Ashish Tewari. Space debris hazards from fragmentations in collinear earth-moon points. 2009.

48. Adam P. Wilmer and Robert A. Bettinger. Lagrangian derivation and stability analysis of multi-body gravitational dynamical models with application to cislunar periodic orbit propagation. *Astrodynamics Specialist Conference*, 2021.

49. Donald T. Greenwood. *Classical Dynamics.* 1 edition, 1997.

50. Howard D. Curtis. *Orbital Mechanics for Engineering Students.* 4 edition, 2013.

51. Bryan Little. Introduction to the three-body problem (3bp). University Lecture, 2020.

52. Chang Liu and Lu Dong. Stabilization of lagrange points in circular restricted three-body problem: A port-hamiltonian approach. *Physics Letters, Section A: General, Atomic and Solid State Physics*, 383:1907–1914, 2019.

53. Iwo Bialynicki-Birula, Maciej Kaliński, and J. H. Eberly. Lagrange equilibrium points in celestial mechanics and nonspreading wave packets for strongly driven rydberg electron. *Physical Review Letters*, 73:1777–1780, 1994.

54. C. Uphoff and M.A. Crouch. Lunar cycler orbits with altering semi-monthly transfer windows. *Journal of the Astronautical Sciences*, 1993.

55. Anthony L. Genova and Buzz Aldrin. Circumlunar free-return cycler orbits for a manned earth-moon space station. *Astrodynamics Speacialist Conference*, 2015.

56. Victor Szebehely. On the elliptical restricted problem of three bodies. *The Astronomical Journal*, 69(3).

57. Richard F. Arenstorf. Regularization theory for the elliptic restricted three body problem. *Journal of Differential Equations*, 6:420–451, 1969.

58. R Brouke. Stability of periodic orbits in the elliptic, restricted three-body problem. *AIAA Journal*, 7:1003–1009, 1969.

59. Michael A. Seeds and Dana E. Backman. *The Solar System*, volume 7. CENGAGE Learning, 1997.

60. Robert E. Ball. *The Fundamentals of Aircraft Combat Survivability Analysis and Design*. American Institute of Aeronautics Astronautics, 2003.

61. E. L. Christiansen. Design and performance equations for calculating spacecraft vulnerability to low Earth orbit debris. *International Journal of Impact Engineering*, 14(1–4):145–156, 1993.

62. E. L. Christiansen. Meteoroid/debris shielding. National Aeronautics and Space Administration, 2003.

63. STK. Astrogator: Circular restricted three-body problem (cr3bp) configuration, 2021.

64. Adam P. Wilmer, Robert A. Bettinger, and Bryan D. Little. Preliminary viability assessment of cislunar periodic orbits for space domain awareness. *2021 Advanced Maui Optical and Space Surveillance Technologies Conference (AMOS)*, 2021.

65. Adam P. Wilmer, Robert A. Bettinger, and Bryan D. Little. Cislunar periodic orbit constellation assessment for space domain awareness of l_1 and l_2 halo orbits. *2021 ASCEND Conference*, 2021.

66. M.C. Davidson. Numerical examples of transition orbits in the restricted three body problem. 1964.

67. David Buehler, Eric Felt, Charles Finley, Peter Garretson, Jaime Stearns, and Andy Williams. Posturing space forces for operations beyond geo. *Space Force Journal*, 2021.

68. J. C. McDowell. The low earth orbit satellite population and impacts of the spacex starlink constellation. *The Astrophysical Journal Letters 892*, pages 1–18, 2020.

69. Terrence Smith. Challenges to future u.s. space control. *Army Space Journal*, page 1, 2002.

70. R.D. Leach and M.B. Alexander. Failures and anomalies attributed to spacecraft charging. *NASA Reference Publication 1375*, 1995.

71. NASA. Planetary defense coordination office. *Nasa.gov*.

72. E. Viollet-Le-Duc. Military architecture. *Oxford and London: James Parker and CO.*, pages 66,85, 1907.

73. D.E. Lee. Gateway destination orbit model: A continuous 15 year nrho reference trajectory. *National Aeronautics and Space Administration (NASA) Report*, 2019.

74. Adam P. Wilmer, Nathan R. Boone, and Robert A. Bettinger. Artificial debris propagation in cislunar periodic orbits. *Astrodynamics Specialist Conference*, 2021.

75. Brian Dunbar. Apollo 13. `https://www.nasa.gov/mission_pages/apollo/missions/apollo13.html`, 2009.

76. Donald J. Dichmann, Ryan Lebois, and John P. Carrico. Dynamics of orbits near 3:1 resonance in the earth-moon system. *The Journal of the Astronautical Sciences*, 60:51–86, 2013.

77. John Carrico JR, Donald Dichmann, Lisa Policastri, John Carrico III, Timothy Craychee, John Ferreira, Marissa Intelisano, Ryan Lebois, Mike Loucks, Travis Schrift, and Ryan Sherman. Lunar-resonant trajectory design for the interstellar boundary explorer (ibex) extended mission. 2011.

78. Mar Vaquero and Kathleen C. Howell. Design of transfers trajectories between resonant orbits in the restricted problem with application to the earth-moon system. 2012.

79. Mar Vaquero and Kathleen C. Howell. Leveraging resonant-orbit manifolds to design transfers between libration-point orbits. *Journal of Guidance, Control, and Dynamics*, 37:1143–1157, 2014.

Author Vita

Lieutenant Adam P. Wilmer graduated from Matoaca High School in Chesterfield, VA in June, 2015. While there, he was the captain of his wrestling team and placed third in the Virginia state tournament. He attained a congressional appointment to attend and entered into the United States Air Force Academy in Colorado Springs, CO, where he studied Mechanical Engineering. During his first year at the Academy, Lt Wilmer received a concussion while wrestling which inevitably caused him to leave the Academy for a year to recover. While away, he attended Virginia Commonwealth University where he obtained a 4.0 GPA in Mechanical Engineering. During his free time Lt Wilmer would assist his grandfather in teaching chess at local underprivileged elementary schools.

Lt Wilmer returned to the Academy in the summer of 2017. While there, he taught survival and evasion, was cadre for Basic Cadet Training, participated in a foreign academy visit to El Salvador's Air Force Academy, and completed basic parachutist training. Over the course of the 2019 summer, Lt Wilmer spent time researching U.S. border patrol Counter Unmanned Aerial System (C-UAS) operations across the northern and southern borders which included travel to Washington D.C., Texas, New York, New Mexico, Pennsylvania, Michigan, and Vermont where he interviewed border patrol agents and C-UAS Subject Matter Experts (SMEs). This research was critical to his undergraduate capstone project (for which he was team lead) and culminated in a publication and filed U.S. patent. Lt Wilmer received the Department of Mechanical Engineering's Graduate School Program (GSP) scholarship, securing a graduate student position and future assignment as an instructor at the Academy.

During his final year, the world experienced a pandemic causing schools and businesses to shut down. As Director of Operations, he assisted with the exodus of over

70 cadets in his squadron to avoid transmission risks. After a fallout of events, it was decided by Academy and Air Force leadership to have an accelerated graduation. Upon graduating in April 2020, he received a Regular Commission in the United States Air Force and relocated to his first assignment as a graduate student at the Air Force Institute of Technology (AFIT). Following completion of the Aeronautical Engineering Masters program he will be assigned to the Air Force Life Cycle Management Center's Propulsion Division located at Wright-Patterson Air Force Base, OH. Lt Wilmer has been approved to the Astronautical Engineering Doctoral program at AFIT and will continue this work until he is able to return to complete his PhD as an in-resident student.

REPORT DOCUMENTATION PAGE

Form Approved
OMB No. 0704–0188

1. REPORT DATE *(DD–MM–YYYY)*	2. REPORT TYPE	3. DATES COVERED *(From — To)*
23–12–2021	Master's Thesis	June 2020 — Dec 2021

4. TITLE AND SUBTITLE

Space Domain Awareness Assessment of Cislunar Periodic Orbits for Lagrange Point Surveillance

5a. CONTRACT NUMBER

5b. GRANT NUMBER

5c. PROGRAM ELEMENT NUMBER

6. AUTHOR(S)

Wilmer, Adam P., 2d Lt, USAF

5d. PROJECT NUMBER

5e. TASK NUMBER

5f. WORK UNIT NUMBER

7. PERFORMING ORGANIZATION NAME(S) AND ADDRESS(ES)

Air Force Institute of Technology
Graduate School of Engineering and Management (AFIT/ENY)
2950 Hobson Way
WPAFB OH 45433-7765

8. PERFORMING ORGANIZATION REPORT NUMBER

AFIT-ENY-MS-21-D-079

9. SPONSORING / MONITORING AGENCY NAME(S) AND ADDRESS(ES)

10. SPONSOR/MONITOR'S ACRONYM(S)

11. SPONSOR/MONITOR'S REPORT NUMBER(S)

12. DISTRIBUTION / AVAILABILITY STATEMENT

DISTRIBUTION STATEMENT A:
APPROVED FOR PUBLIC RELEASE; DISTRIBUTION UNLIMITED.

13. SUPPLEMENTARY NOTES

14. ABSTRACT

Cislunar periodic orbits provide an elegant means to fill the observational capability gaps which are present in ground-based and/or near-Earth spaced-base sensors. This research involves theoretical analysis on the effectiveness of cislunar periodic orbits for Space Domain Awareness (SDA) mission architectures. Specifically, cislunar periodic orbits are analyzed, both individually and in constellations with one another, for their effectiveness at monitoring target satellites in Lyapunov and halo orbits about the Earth - Moon L_1 and L_2 Lagrange points. All orbits are created and modeled in the Circular Restricted Three-Body Problem (CR3BP), then subject to perturbations in both the Elliptical Restricted Three-Body Problem (ER3BP) and the Bicircular Restricted Four-Body Problem (BCR4BP) to observe dynamical variations. A new taxonomy for the classification of SDA regions is also presented which will enable a spatial division of the national SDA mission portfolio. Finally, select cislunar periodic orbits are subject to a catastrophic spacecraft explosion to understand the debris-related consequences of mishaps within this orbital regime.

15. SUBJECT TERMS

Cislunar, Periodic Orbit, Space Domain Awareness, Space Situational Awareness, Lagrange Point, Artificial Debris, Lyapunov Orbit, Halo Orbit

16. SECURITY CLASSIFICATION OF:			17. LIMITATION OF ABSTRACT	18. NUMBER OF PAGES	19a. NAME OF RESPONSIBLE PERSON
a. REPORT	b. ABSTRACT	c. THIS PAGE			Robert A. Bettinger, Maj
U	U	U	UU	191	19b. TELEPHONE NUMBER *(include area code)* (937) 255-6565 x4578; Robert.Bettinger@afit.edu